

UNIVERSITÀ DELLA CALABRIA



**UNIVERSITÀ DELLA CALABRIA**

Dipartimento di Fisica

**Dottorato di Ricerca in**

**SCIENZE E TECNOLOGIE FISICHE, CHIMICHE E DEI MATERIALI**

**CICLO**

**XXIX**

**TITOLO TESI**

**TURBULENCE IN SPACE PLASMAS:**

**ANALYSIS OF OBSERVATIONS AND THEORETICAL MODELS**

**Settore Scientifico Disciplinare FIS/03**

**Coordinatore:** Ch.mo Prof. VINCENZO CARBONE

Firma Vincenzo Carbone

**Supervisore/Tutor:** Ch.mo Prof. FRANCESCO MALARA

Firma Francesco Malara

**Co-Supervisor:** Dott. LUCA SORRISO-VALVO

Firma Luca Sorriso-Valvo

Dott. ALESSANDRO RETINO'

Firma Alessandro Retino'

**Dottorando:** Dott./ssa FRANCESCA DI MARE

Firma Francesca Di Mare

## Abstract

Turbulence represents an universal phenomenon characterizing the dynamics of different kinds of fluids, like gases, liquids, plasmas, etc., both in nature and in laboratory devices. It is responsible for the efficient transfer of energy across scales, making the connection between the macroscopic flow and the microscopic dissipation of its energy. Moreover, turbulence plays a key role in determining various phenomena. For instance, the anomalous diffusion of tracers in a flow may be controlled by the properties of turbulence, and the transport of charged particles in astrophysical or laboratory plasmas is determined by the properties of the turbulent magnetic field. Synthetic turbulence models are a useful tool that provide realistic representations of turbulence, necessary to test theoretical results, to serve as background fields in some numerical simulations, and to test analysis tools. Models of 1D and 3D synthetic turbulence previously developed still required large computational resources. A new “wavelet-based” model of synthetic turbulence, able to produce a field with tunable spectral law, intermittency and anisotropy, is presented here. The rapid algorithm introduced, based on the classic p-model of intermittent turbulence, allows to reach a broad spectral range using a modest computational effort. The model has been tested against the standard diagnostics for intermittent turbulence, all showing an excellent response. The same analysis tools have been used to study a more specific subject, of interest in space physics, i.e., the turbulence at the interface between the solar wind and the Earth’s magnetosphere, mediated by the magnetopause. The dynamics occurring at this boundary depends on various aspects as, e.g., the solar wind dynamic pressure or the direction of the Interplanetary Magnetic Field (IMF). If the IMF is directed northward the formation of a wide boundary layer at the low latitude is observed. This boundary layer is thought to be the result of the observed plasma transfer, driven by the development of the Kelvin-Helmholtz instability, originating from the velocity shear between the solar wind and the almost static near-Earth plasma. Our interest is to describe these phenomena and build a collection of event related to rolled-up vortices, spatially located on the tail-flank magnetopause, previously studied by Hasegawa *et al.* (2006) and Lin *et al.* (2014). The scope is to study the properties of plasma turbulence and intermittency inside the magnetosheath, with the aim to understand the evolution of turbulence, as a result of the development of KH instability. The analysis we present, represents a complete and quantitative characterization of turbulence and associated intermittency

in this region. It appears that a fluctuating behaviour during the progressive departure along the Geocentric Solar Magnetosphere (GSM) coordinate system may exist, and it is visible as a quasi-periodic modulation of the exponent. The periodicity associated with such oscillation can be estimated to be approximately  $6 - 7 R_E$ , which is consistent with the typical periodicity of the magnetosheath KH. This suggest that a kind of signature related to the development of the KH unstable modes could be present in the statistical properties of the magnetic turbulence.

## Riassunto

La turbolenza rappresenta l'aspetto dinamico più comune del flusso di un fluido. Essa è responsabile del trasporto efficiente di energia dalle grandi scale, dove avviene l'iniezione, fino alle piccole scale in cui, dopo l'attivazione delle dinamiche non lineari, hanno luogo i processi dissipativi. Per tali ragioni, la turbolenza gioca un ruolo fondamentale in vari fenomeni quali ad esempio, il trasporto di particelle in plasmi astrofisici o di laboratorio, lo studio della diffusione anomala di traccianti nei fluidi e via di seguito. I modelli di turbolenza sintetica si inseriscono in tale contesto in quanto forniscono un valido strumento per ricreare quanto più realisticamente il fenomeno della turbolenza. Essi sono usati per testare risultati teorici, per fornire un sistema turbolento su cui lavorare con simulazioni numeriche al fine di ottenere le leggi fisiche cercate. I modelli di turbolenza sintetica precedentemente sviluppati, presentano dei limiti stringenti dal punto di vista della memoria di archiviazione enorme, di cui necessitano, e di tempi di calcolo considerevoli. Il lavoro di tesi vuole presentare un nuovo modello, appartenente alla classe dei cosiddetti modelli "wavelet-based", capace di riprodurre un campo caratterizzato da leggi di scala adattabili alle proprie esigenze di analisi. L'algoritmo realizza la cascata turbolenta come il modello  $p$  di Meneveau e Sreenivasan, prevedendo di raggiungere un ampio range spettrale con uno sforzo computazionale davvero modesto. Il modello è stato testato mediante la diagnostica standard di analisi per la turbolenza che prevede intermittenza, per cui è stata fatta un'analisi spettrale e statistica delle fluttuazioni delle grandezze in esame dipendenti dalle scale a cui si osserva il fenomeno. La risposta del sistema è stata eccellente ed in accordo con le leggi teoriche attese. Il lavoro è stato presentato e pubblicato in un recente articolo (Malara *et al.*, 2016). La stessa analisi è stata utilizzata per studiare la dinamica turbolenta che si verifica in un contesto ben specifico, ossia lungo i fianchi della magnetopausa. Essa rappresenta la regione di separazione tra il plasma ed il campo magnetico della magnetogaina, da quelli della magnetosfera più interna. I processi che hanno luogo in questa regione sono piuttosto complessi e diversi, in particolare, a seconda dell'orientazione del campo magnetico interplanetario. Oggetto del nostro studio è stata l'analisi statistica delle proprietà di strutture turbolente originate per mezzo dell'instabilità di Kelvin-Helmholtz e la caratterizzazione delle stesse, al fine di far emergere una dinamica evolutiva in funzione dell'allontanamento progressivo dal piano alba-tramonto fino ai fianchi più esterni della magnetopausa. È stato collezionato un set di eventi delle missioni spaziali THEMIS e Geotail, associati a vortici di Kelvin-Helmholtz studiati da Hasegawa *et al.*, 2006 e Lin *et al.*, 2014. L'analisi statistica ha evidenziato caratteristiche tipiche della

turbolenza, con lo studio delle stesse leggi di scala. Si è osservato un comportamento fluttuante degli indici delle suddette leggi di scala, in dipendenza delle coordinate spaziali del sistema e l'emergere di una modulazione quasi periodica dei parametri calcolati, che si sviluppa con un periodo caratteristico dell'ordine di 6 raggi terrestri, in accordo con i periodi tipici delle fluttuazioni dei vortici di Kelvin-Helmholtz osservati. Tale comportamento può essere interpretato come l'esistenza di una sorta di comportamento tipico o marker di tali instabilità, che emerge attraverso le proprietà statistiche del campo elettromagnetico, oggetto del nostro studio.

# Contents

<b>1</b>	<b>Introduction</b>	<b>5</b>
<b>2</b>	<b>Turbulence and intermittency</b>	<b>8</b>
1	MHD description of plasma . . . . .	8
1.1	The magnetohydrodynamic description . . . . .	12
2	MHD turbulence . . . . .	18
2.1	The Reynolds number . . . . .	18
2.2	The turbulent cascade . . . . .	20
3	Analisis of turbulent field . . . . .	23
3.1	Energy spectra . . . . .	24
3.2	Probability distribution functions (PDFs) . . . . .	25
3.3	Structure functions . . . . .	28
4	Phenomenology of turbulence and scaling laws . . . . .	28
4.1	Scaling laws of MHD . . . . .	29
4.2	Kolmogorov law . . . . .	30
4.3	Alfvén effect: the Kraichnan spectrum . . . . .	33
4.4	The structure functions scaling laws . . . . .	34
4.5	Self-similarity and the scaling of PDF shape . . . . .	34
5	Intermittency . . . . .	36
5.1	The problem of intermittency in turbulence . . . . .	36
5.2	The multiplicative cascade, fractal and multifractal models . . . . .	40
6	Summary . . . . .	47
<b>3</b>	<b>Synthetic Turbulence</b>	<b>49</b>
1	State of the art and previous models . . . . .	50
2	Description of the model . . . . .	53
2.1	Spectrum and cell hierarchy . . . . .	54
2.2	Eddy structure . . . . .	56
2.3	Turbulent cascade and intermittency . . . . .	60
2.4	Eddy superposition algorithm . . . . .	63

2.5	Anisotropic spectrum . . . . .	67
3	Testing the model . . . . .	70
3.1	Isotropic turbulence . . . . .	72
3.2	Multifractal Analysis. . . . .	80
3.3	Anisotropic turbulence . . . . .	86
4	Summary . . . . .	92
<b>4</b>	<b>Turbulence in Kelvin-Helmholtz instability</b>	<b>96</b>
1	Solar Wind and Earth's magnetosphere: description and interaction . . . . .	97
1.1	Magnetospheric plasma region . . . . .	101
1.2	Discontinuities in space plasma physics: magnifying glass on the magnetopause . . . . .	102
2	Kelvin-Helmholtz instability . . . . .	106
3	Data set overview . . . . .	109
3.1	The GEOTAIL mission . . . . .	110
3.2	The THEMIS mission . . . . .	113
4	Analysis of Geotail and THEMIS data . . . . .	115
4.1	Autocorrelation function . . . . .	123
4.2	Spectrum of magnetic energy . . . . .	123
4.3	Probability Distribution Function . . . . .	128
4.4	Kurtosis . . . . .	128
5	Transition to turbulence in the magnetosheath Kelvin-Helmholtz instability . . . . .	131
6	Summary . . . . .	147
<b>5</b>	<b>Conclusions and Perspectives</b>	<b>150</b>
	<b>BIBLIOGRAPHY</b>	<b>172</b>

# Chapter 1

## Introduction

This thesis deals with the characterisation and modelling of turbulent phenomena observed in space plasmas. We present and discuss in details a new model of synthetic turbulence, i.e., a numerical model which generates a turbulent field whose statistical properties are similar to those of a real turbulent system. The power of this model consist in the fact that it is capable to reproduce very large ranges of spatial scales with very low memory requirements and short computational times. This feature is very important in all the cases in which a high-Reynolds-number turbulence is to be represented, as typically happens in astrophysical applications. For this reason, it can be also useful in specific contexts, such as understanding fundamental scaling properties of turbulence, describing processes that involve very different spatial scales (e.g., particle transport or acceleration, diffusion, and drop formation), evaluating subgrid stresses and generating initial conditions for numerical simulations. The model has been presented in a recent paper (Malara *et al.*, 2016 [75]). An application of our model to the problem of energetic particle transport in a turbulent magnetic field is described in the paper by Pucci *et al.*, 2016 [99]. The model has been tested against the

standard diagnostics for intermittent turbulence, i.e., the spectral analysis, the scale-dependent statistics of the field increments, and the multifractal analysis, all showing an excellent response.

The same analysis tools have been performed to study the properties of plasma turbulence and intermittency inside magnetosheath, in particular along the flank low latitude boundary layer (LLBL), under northward interplanetary magnetic field. The survey was brought forward by using data from Geotail and THEMIS missions, taken during satellite magnetopause crossings. The goal is to study the evolution of the turbulence, driven by the development of the Kelvin Helmholtz instability (KH), in order to understand how the particles transport works from solar wind and magnetosphere and, more generally, what are the mechanisms of interaction between the latter ones. Finally, we have focused our attention on the study of the evolution of turbulence as a result of the develop of KH, as it moves away from the Sun in direction dawn and dusk flank of the terrestrial magnetosphere. The aim is to have a complete and quantitative characterization of turbulence and associated intermittence in this region, which is still poorly studied.

The thesis is formed by three main parts and it is organized as follow.

The Chapter 2 is devoted to the introduction of the main concepts of magnetohydrodynamics (MHD) and turbulence. The major pillars of the theory of turbulence like Kolmogorov (1941) for fluids, and then Kraichnan (1965) for MHD are described, together with the statistical properties of velocity and magnetic fields, as well as the tools used to describe it. The end of this chapter is devoted to discuss how the intermittency phenomenon can be explained through multiplicative processes. Moreover, methods which are used

to characterize intermittency and structures linked to it, will be described. In Chapter 3 we present a new model of synthetic turbulence, belonging to the class of “wavelet-based” models, able to reproduce a field with tunable spectral law, intermittency and anisotropy. After an introduction about the state of the art and previous models, a detailed description of the model is given. Then we validate the model by analyzing its statistical properties applying time-series analysis techniques. All the tests gave satisfactory results, showing that the synthetic data reproduce well the required conditions of spectral scaling and intermittency.

In Chapter 4 we initially give a broad description of solar wind and Earth’s magnetosphere interaction, by establishing a framework to ensure the comprehension of background and the phenomena in it. Then, we focus our attention on the mechanisms that develop inside this region, in particular on the KH and the several configuration in which the interplanetary magnetic field can occur. Then, we introduce the data set studied, passing through a brief description of the space missions, from which the data have been taken. Finally, a description of the statistical analysis and a discussion of the derived results is given.

# Chapter 2

## Turbulence and intermittency

### 1 The magnetohydrodynamic description of plasmas

Plasmas are the most common phase of ordinary matter in the universe, that appear in nature in various forms such as space and astrophysical plasmas (e.g. the Sun and other stars, the solar wind, the interplanetary medium between planets, the interstellar medium between star systems, the intergalactic medium between galaxies), or terrestrial plasmas, very rare on Earth, like lightning flashes during storms and polar aurorae. Plasma represents the “fourth state” of the matter, in which an important fraction of the atoms is ionized. Ionization occurs when the temperature is hot enough, so that electrons and ions are separately free. To be more accurate, this happens when the mean kinetic energy of electrons and ions exceeds the ionization potential energy of atoms, and the unbound positive and negative particles are separated. Moving charged particles produces electric currents and spatial charges, which generates electric and magnetic fields. In turn, such fields affect the motion of charged particles. For this reason, the plasma dynamic

is rather complex, because of the electromagnetic nature of the interactions between the charged particles composing the gas. Nonetheless, it can be described, using sets of equations, at different approximation levels (Akhiezer *et al.*, 1975 [1]). In order to characterize the state of the plasma it is useful to define some characteristic quantities, which are described in the following. From now on, let us consider two kinds of particles, namely electrons ( $e$ ), and a single kind of positive ions ( $i$ , mainly protons), with their density  $n_{e,i}$ , their mass  $m_{e,i}$ , and the elementary charge  $\pm e$ .

The typical particle velocity can be represented by their *thermal velocity*:

$$v_{e,i} \simeq \sqrt{\kappa_B T_{e,i} / m_{e,i}} ,$$

where  $T_{e,i}$  are the average temperatures of the particle gases, and  $k_B$  is the Boltzmann constant.

The *electron plasma frequency* is the typical oscillation frequency associated with local charge separation:

$$\omega_{pe} \simeq \sqrt{\frac{4\pi n_e e^2}{m_e}} ,$$

and its reciprocal gives the typical separation time between charges.

The *ion plasma frequency* can also be defined, using the ion mass, density and charge:

$$\omega_{pi} \simeq \sqrt{\frac{4\pi n_i e^2}{m_i}} .$$

The *Debye length* is the ratio between the thermal speed of electrons and the

plasma frequency:

$$\lambda_D \simeq \frac{v_e}{\omega_{pe}} \simeq \sqrt{\frac{k_B T}{4\pi n_e e^2}},$$

and is the typical shielding length of the charges. In fact, it represents the balance length between thermal and electrostatic effects, so that for scales larger than  $\lambda_D$ , the plasma can be seen as electrically neutral.

The number of particles in a Debye sphere is

$$N = \frac{4\pi n \lambda_D^3}{3} \propto n \lambda_D^3,$$

the shielding of individual charge is efficient if  $N$  is much larger than unity.

It is usually convenient to deal with dimensionless quantities, for this reason we define the plasma parameter  $g$  as:

$$g = \frac{1}{n \lambda_D^3}$$

This number is very small when there are many electrons in a Debye sphere and since it is proportional to the ratio of potential energy over kinetic energy, it means that the average potential energy must be (much) less than the average kinetic energy. This is also a measure of the dominance of collective interactions over single particle interactions. The number of electrons in a Debye sphere is large if  $g$  is small, therefore less likely there will be a significant force on a particle due to collisions. Plasma oscillations are an example of collective interactions. Imagining to displace a certain amount of electrons (or ions) with respect to their original configuration in a plasma, then the electric force will try to restore the system to its original position. This generates oscillations which take place at the above-defined plasma frequency.

The *cyclotron frequency* of electrons and ions is defined if an external magnetic field  $B$  is present, which is often the case in plasmas. In that case, the frequency at which electrons and ions turn around the magnetic field lines is

$$\Omega_{e,i} = \frac{eB}{cm_{e,i}}$$

where  $c$  is the speed of light.

The *plasma parameter*

$$\beta = \frac{P_K}{P_B} = \frac{8\pi n_i \kappa_B T}{B^2},$$

is the ratio between the kinetic and magnetic pressures, where  $P_K = n_i \kappa_B T$  is the kinetic pressure and  $P_B = B^2/8\pi$  the magnetic pressure. It is useful to describe the state of magnetization of the plasma, and to individuate if magnetic or kinetic effects are predominant in the dynamics.

All these quantities can be used to describe the conditions of the plasma, and to use approximations, in order to simplify the equations in the different regimes. Typical values of the previous quantities in different plasma systems are displayed in the Table 2.1, revealing the extremely wide range in which they lay.

Plasma	$T$ (K)	$n_e$	$B$ (Gauss)	$\lambda_D$ (cm)	$\omega_{pe}$ (Hz)	$\Omega_i$ (Hz)
SC	$10^6$	$10^6$	$10^2$	10	$10^8$	$10^9$
SW	$10^5$	10	$10^{-4}$	$10^3$	$10^5$	$10^3$
MS	$10^8$	1	$10^{-3}$	$10^5$	$10^5$	$10^4$
IS	$10^3$	$10^{10}$	1	$10^{-3}$	$10^{10}$	$10^7$
IM	$10^4$	1	$10^{-5}$	$10^3$	$10^5$	$10^2$

Table 2.1: Typical values of some parameters for different kinds of astrophysical plasmas: SC = Solar Corona; SW = Solar Wind at 1 AU; MS = Magnetosphere; IS = Ionosphere; IM = Interstellar Medium.

## 1.1 The magnetohydrodynamic description

Different theoretical descriptions of a plasma are adopted, according to the typical spatial and temporal scales which characterize the phenomenon under study, in comparison with the characteristic lengths and times discussed above. First, we give an overview of these different theoretical approaches:

- a *single particle description*, where the collective plasma behaviour is completely neglected, and the dynamic of the system is determined solving the equations of motion of single particles. This description is valid in low density plasmas with an external magnetic field much more intense than that generated by the individual particles.
- a *kinetic description* that adopts a statistical representation of the plasma, studying the evolution of the particles distribution function  $f(\mathbf{x}, \mathbf{v}, t)$  in the phase space, that contains a detailed information on the plasma state at any given spatial position and time. At the most detailed level, the evolution of the distribution functions of the different kind of particles are described by the Liouville equation, or by the Vlasov equation when collisions among particles are neglected. In both cases, Maxwell equations are used to describe the evolution of the electric and magnetic field. The particle densities and their velocities, as well as higher order moments, can then be obtained by integration of the distribution functions. This kind of approach is useful when a microscopic description of the system is needed.
- a *multi-fluid description* considers the dynamics of each single kind of

particles as a whole. This approach is used to obtain a description of large-scale phenomena in a plasma. Each particle population is represented as a charged fluid characterized by macroscopic parameters (density, velocity, temperature), referring to volume elements which are at the same time much smaller than the whole size of the system, but large enough to contain a great number of particles. Then, in the multi-fluid theory the plasma can be seen as a superposition of interacting fluids, each one composed of a single sorta of particles, and thus each one obeying to a (non-closed) set of fluid-like equations. The fluid description requires thermalization, so that the distribution functions of the particles can be approximated by Maxwellians. Of course this can be only done if the dynamical time scales are larger than the typical thermalization time. This condition is referred to as *local thermodynamical equilibrium (LTE)*. In that case, conservation laws can be written, by integration of the Vlasov equation, for the moments of the particle distributions, leading to the set of the moment equations. For each particle species, these are the conservation laws for mass, moment, energy and so on. A closure hypothesis, as for example a state equation, is required to close the hierarchy of the moment equations. Moreover, the Maxwell equations are needed in order to describe the electromagnetic interactions. Still, the fluid equations are quite difficult to use, and further approximations can be made in order to simplify them.

- A successive approximation of the multi-fluid theory is the *Magnetohydrodynamics (MHD) theory*, dealt with in more detail below, in which

the plasma is described as a single conducting fluid. The MHD theory provides a good description of plasmas in the event that the time variations of macroscopic quantities are slower than the above-discussed plasma time scales.

The governing equations are derived from the equations of fluid dynamics and Maxwell's equations. Since  $m_p \sim 2000m_e$ , terms containing  $m_e/m_p$  can be neglected with respect to unity or  $m_p/m_e$ . This corresponds to ignore the inertia of the electrons in the flow. In MHD only phenomena at large time scales, i.e., much larger than both the ion gyroperiod and the inverse plasma frequency, are considered. The plasma can then be seen as a ion fluid, described by a fluid-like equation, "followed" by an electron current obeying the Ohm's law. Electrical currents flowing within the fluid are due to electron motions relative to the ion background. For time scales larger than the reciprocal of the electron plasma frequency, and for spatial scales larger than the Debye length, the *quasi-neutrality of charge* is assured and the plasma can be considered as electrically neutral. Finally, when nonrelativistic regime is concerned, all the contributions of order  $(v/c)^2$  can be neglected in the equations. The conservation laws can then be written for the physical quantities involved in the system, mass density  $\rho$ , flow velocity  $\mathbf{v}$  and internal energy per mass unit  $U$  of the protons (Akhiezer *et al.*, 1975 [1]):

$$\frac{\partial \rho}{\partial t} + \nabla \cdot (\rho \mathbf{v}) = 0 \quad (2.1)$$

$$\rho \left[ \frac{\partial}{\partial t} + (\mathbf{v} \cdot \nabla) \right] \mathbf{v} = -\nabla p + \nabla \cdot \bar{\bar{\boldsymbol{\sigma}}} + \mathbf{f} \quad (2.2)$$

$$\rho \left[ \frac{\partial}{\partial t} + (\mathbf{v} \cdot \nabla) \right] U = -p(\nabla \cdot \mathbf{v}) - \nabla \cdot \mathbf{q} + \sum_{i,j} \sigma_{ij} \frac{\partial v_i}{\partial x_j} + Q. \quad (2.3)$$

In previous equations,  $\mathbf{f}$  represents the sum of the external forces acting on the magneto-flow per unit mass. The term  $\overline{\boldsymbol{\sigma}}$  is the stress tensor excluding the kinetic pressure  $p$  contribution, which is treated separately. The term  $\mathbf{q}$  is the heat flux, and  $Q$  is the heat produced inside the system. In many cases, as for the plasmas treated within the present work, the only force involved is the Lorentz force. In this case, the force term can be written as:

$$\mathbf{f} = \frac{1}{c} \mathbf{J} \times \mathbf{B} . \quad (2.4)$$

where the quasi-neutrality has been used to drop the electric field contribution to the force. The same argument holds for the heat terms, so that the Joule effect is often the only internal source of heat. It is worth mentioning again that the previous equations are not closed. In fact, a closure hypothesis is needed. It is often possible to use a state equation, so that the number of unknowns is reduced and the system is closed. For example, if the plasma behaves like a perfect gas, the state equation  $p = k_B \rho T / m$  can be used to eliminate the kinetic pressure from the equations.

The moments equations must be coupled to the Maxwell equations to include the electromagnetic properties of the plasma. The Faraday law and the Ampere law are both considered, in which the displacement current can be neglected in the non-relativistic regime:

$$\nabla \times \mathbf{E} = -\frac{1}{c} \frac{\partial \mathbf{B}}{\partial t} \quad (2.5)$$

$$\nabla \times \mathbf{B} = \frac{4\pi}{c} \mathbf{J} \quad (2.6)$$

along with the condition

$$\nabla \cdot \mathbf{B} = 0 \quad (2.7)$$

where  $\mathbf{E}$  and  $\mathbf{B}$  are the electric and magnetic fields respectively.

The Ohm's law, in the MHD framework, is rewritten in its generalized form as:

$$\mathbf{E} + \frac{1}{c} \mathbf{v} \times \mathbf{B} = \eta \nabla^2 \mathbf{B} . \quad (2.8)$$

where  $\eta$  is the resistivity of the plasma.

The Lorentz force (2.4), the last Maxwell equation (2.6) and the Ohm's law (2.8) can be now used to rewrite the conservation laws. The mass conservation law (2.1) remains invariate, and so does the energy conservation law (2.3), as far as we do not use any state equation. The impulse conservation law become

$$\rho \left[ \frac{\partial}{\partial t} + (\mathbf{v} \cdot \nabla) \right] \mathbf{v} = \frac{1}{4\pi} (\nabla \times \mathbf{B}) \times \mathbf{B} - \nabla p + \nabla \cdot \bar{\bar{\sigma}} \quad (2.9)$$

The Maxwell equation (2.5) is used to describe the evolution of the magnetic field. Defining the magnetic diffusion coefficient

$$\lambda = \frac{c^2 \eta}{4\pi} ,$$

it can be rewritten as

$$\frac{\partial \mathbf{B}}{\partial t} = \nabla \times (\mathbf{v} \times \mathbf{B}) + \lambda \nabla^2 \mathbf{B} \quad (2.10)$$

and is called the *induction equation*.

Equations (2.1), (2.9), (2.10) and (2.3) are the full set of the MHD equations, and together with the remaining Maxwell laws, the Ohm's law, and a state equation for the closure, can be used to describe the dynamics of a plasma in the magnetohydrodynamic approximation. It is clear that the heat terms  $q$  and  $Q$ , as well as the stress tensor  $\bar{\bar{\sigma}}$ , could introduce new variables in the equations, and thus need to be modeled in order to solve the

equations. The MHD equations own a similar structure to the Navier-Stokes equations (NS), which describe the dynamic of a fluid. The main characteristic of both sets of equations is the presence of non-linear terms, but the MHD equations have extra terms describing the coupling between velocity and magnetic field.

In the event that the flow is incompressible, e.g. when the density is a constant, MHD equations are subjected to strongly simplifications, as in the case of NS equations in the fluid case. The mass conservation law becomes simply under the incompressibility condition  $\nabla \cdot \mathbf{v} = \mathbf{0}$ . The energy conservation equation can also be dropped. Let us introduce the following new variable

$$\mathbf{b}(\mathbf{r}, t) = \frac{\mathbf{B}}{\sqrt{4\pi\rho}} .$$

When  $\rho$  is constant, the field  $\mathbf{b}$  is proportional to the magnetic field  $\mathbf{B}$ , but with the dimension of a velocity. Using the property of the incompressibility and replacing the magnetic field with the field  $\mathbf{b}$ , we can introduce the kinematic viscosity  $\nu$  and the magnetic diffusivity  $\mu = \frac{c^2\eta}{4\pi\rho}$ , then the (incompressible) MHD equations can be written in the simpler form:

$$\frac{\partial \mathbf{v}}{\partial t} + (\mathbf{v} \cdot \nabla) \mathbf{v} = (\nabla \times \mathbf{b}) \times \mathbf{b} - \nabla \mathbf{p} + \nu \nabla^2 \mathbf{v} \quad (2.11)$$

$$\frac{\partial \mathbf{b}}{\partial t} = \nabla \times (\mathbf{v} \times \mathbf{b}) + \mu \nabla^2 \mathbf{b} \quad (2.12)$$

$$\nabla \cdot \mathbf{v} = \nabla \cdot \mathbf{b} = \mathbf{0} . \quad (2.13)$$

A linear combinations of  $\mathbf{b}$  and  $\mathbf{v}$  allows to compact the previous equations by means the following Elsässer variables (Elsässer, 1950 [37]):

$$\mathbf{Z}^\pm = \mathbf{v} \pm \mathbf{b} \quad (2.14)$$

These variables are useful when we want to study, for example, the correlation between the fluctuations of velocity and magnetic field. Using the Elsässer variables, the MHD equations become

$$\begin{aligned} \frac{\partial \mathbf{Z}^\pm}{\partial t} + (\mathbf{Z}^\mp \cdot \nabla) \mathbf{Z}^\pm &= & (2.15) \\ = -\frac{1}{\rho} \nabla \left( p + \frac{B^2}{8\pi} \right) + \frac{\nu + \mu}{2} \nabla^2 \mathbf{Z}^+ + \frac{\nu - \mu}{2} \nabla^2 \mathbf{Z}^- & \\ \nabla \cdot \mathbf{Z}^\pm &= 0. & (2.16) \end{aligned}$$

This is a more compact and symmetric set of four equations. It is worth noting that the nonlinear term is proportional to both variables, so nonlinearities vanish if one of the Elsässer fields is zero, that is the solution  $\mathbf{Z}^\mp = \mathbf{0}$  and  $\mathbf{Z}^\pm \neq \mathbf{0}$  is a result of the nonlinear equations. In case of vanishing magnetic field, the two “+” and “-” equations (2.16) become identical, as well as the two equations (2.16), and the NS equations are recovered.

## 2 MHD turbulence

### 2.1 The Reynolds number

Turbulence represents a common phenomenon in the dynamics of weakly dissipative fluid flows. Our study is aimed at magnetohydrodynamics turbulence that involves not only the velocity field as in ordinary fluids, but also the magnetic field. A turbulent state is characterized by irregular variations of the fields (velocity and magnetic field), as well as of fluid particle trajectories. In order to clarify these concepts, we can introduce some typical values for the main variables in the MHD equations. So, let  $\ell_0$  be a typical length scale of the system,  $v_0$  and  $B_0$  typical (average) velocity and magnetic field.

It is useful to introduce the *Alfvén velocity*

$$c_A = \frac{B_0}{\sqrt{4\pi\rho}}$$

representing the typical propagation velocity for Alfvén waves (see for example Akhiezer *et al.*, 1975 [1]). In the framework of turbulence phenomenology, it is possible to individuate, within the MHD equations, different terms whose contribution to the dynamics depends on the particular regime. In particular, a key role is played by nonlinear and dissipative terms, whose balance determines whether or not the system is a turbulent state. In a fluid dynamics, the usual way to express the balance between these terms is by a typical parameter that characterizes the state of motion of a fluid, namely the (kinematic) *Reynolds number*  $R_v$ . It gives the order of magnitude of the ratio between nonlinear and dissipative terms:

$$R_v = \frac{\ell_0 v_0}{\nu} \sim \frac{|(\mathbf{v} \cdot \nabla)\mathbf{v}|}{|\nu \nabla^2 \mathbf{v}|}.$$

The same definition is used also in MHD. In analogy, in MHD a *magnetic Reynolds number*  $R_m$  is also defined as

$$R_m = \frac{\ell_0 c_A}{\mu} \sim \frac{|(\nabla \times \mathbf{v} \times \mathbf{B})|}{|\mu \nabla^2 \mathbf{B}|}.$$

For low Reynolds numbers, it is clear that the (linear) dissipative terms dominate the dynamics. In such a case, nonlinear interactions are small enough to be neglected, and the system follows a regular behaviour. In fluid dynamics, this is referred to as “laminar” regime. With increasing the Reynolds number, nonlinear effects dominate more and more the dynamics; when the Reynolds number overcomes a given threshold the system reaches a turbulent state.

## 2.2 The turbulent cascade

The effects of nonlinear terms, both in fluid dynamics and in MHD, is to transfer energy from a given spatial scale to another. A simple way to see this phenomenon is to perform a Fourier transform of the fields and to write the equations in the Fourier space. In this way, nonlinear terms give origin to convolution products. For instance, let us consider the following nonlinear term:

$$(\mathbf{v} \cdot \nabla) \mathbf{v} \rightarrow \sum_{\mathbf{k}_1, \mathbf{k}_2} \mathbf{v}_{\mathbf{k}_1} \cdot i\mathbf{k}_2 \mathbf{v}_{\mathbf{k}_2} \delta_{\mathbf{k}, \mathbf{k}_1 + \mathbf{k}_2} \quad (2.17)$$

where  $i\mathbf{k}\mathbf{v}_{\mathbf{k}}$  is the Fourier transform of  $\nabla\mathbf{v}$ , and  $\mathbf{v}_{\mathbf{k}}$  is the Fourier transform of  $\mathbf{v}$ . This indicates that the nonlinear term couples fluctuations at different wavevectors, i.e., at different spatial scale, in a triangular way, according to the relation  $\mathbf{k} = \mathbf{k}_1 + \mathbf{k}_2$ . Similar considerations can be done also for the other nonlinear terms. Concerning dissipative terms (due to viscosity and/or resistivity), since they are proportional to second derivatives of the fields, they becomes more effective at smaller scales, while they are essentially uneffective at large and intermediate scales, provided that the Reynolds numbers are large enough. Thus, the typical scenario of the turbulence is the following: energy is injected into the system at large scales by some mechanism. Nonlinear terms transfer energy from fluctuations at the large injection scale to fluctuations at smaller and smaller scales; this mechanism is called *energy cascade*. When the energy reaches small enough scales (dissipative scales), dissipation becomes effective and the fluctuation energy is dissipated into heat. The nonlinear cascade fills up with energy all the scales in between the injection and the dissipative scale. From a phenomenological point of

view, the cascade can be seen as a process of fragmentation of large-scale structures that shatter to produce smaller structures. In fluid dynamics, the energy injection process taking place at the scale  $\ell_0$  could be due, for instance, to the presence of an obstacle, or a grid of size  $\sim \ell_0$ ; the length  $\ell_0$  could also represent the distance between the walls in a channel. For low Reynolds numbers, nonlinear terms are uneffective and the resulting flow is laminar. Increasing the Reynolds number, large scale vortices form, which become more and more unsteady, and start fragmenting into smaller vortices. When the Reynolds number is larger than some critical value, the flow is said to be in *fully developed turbulence* regime. The fully developed turbulence can be considered statistically homogeneous. Statistical homogeneity is a property whereby average quantities do not depend on the position, for which the two points correlation for a given physical quantity depends only on the distance between them, but not on their position. As mentioned, the turbulence is a typical phenomenon of the highly non-linear systems and the non-linearity of equations poses several difficulties in their mathematical approach. In these conditions, the fields are highly chaotic, with overlapping of different structures over a wide range of scales. In fully developed turbulence it is possible to individuate three different ranges of scales. The large scales, characteristics of the system, at which the energy is injected from some external forcing, are called *integral scales*. The scales at which the dissipation is dominant belong to the *dissipative range*. In between the integral and the dissipative scales there is a range in which the dynamics is dominated by nonlinear effects generating energy transfers among different

wavevectors. This range of scales is usually called “inertial range”<sup>1</sup>.

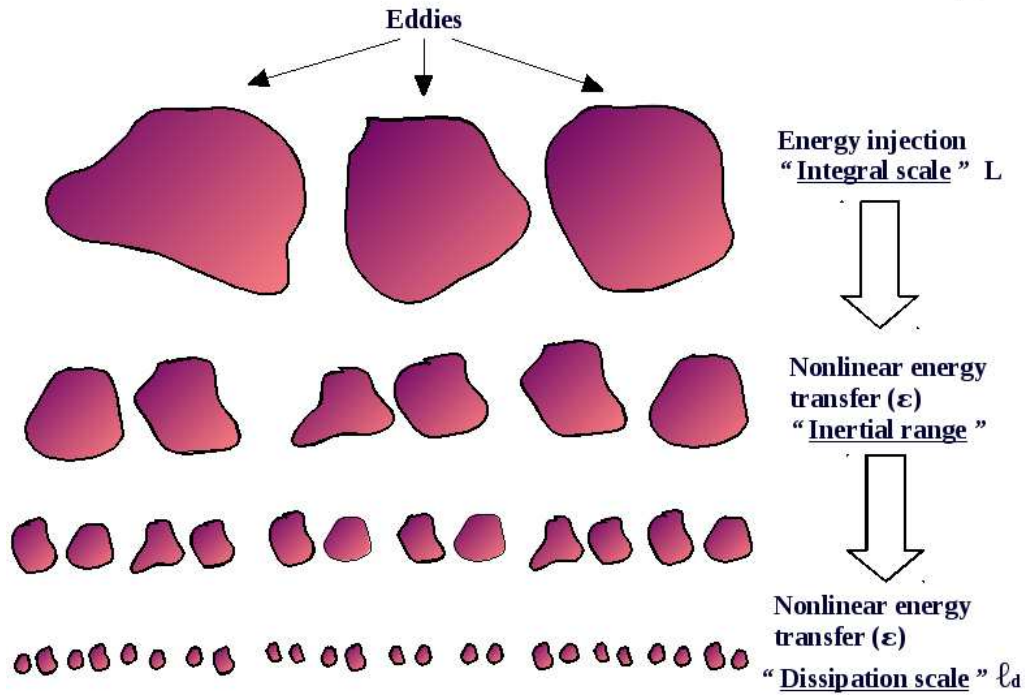


Figure 2.1: A schematic picture of the Richardson cascade. The hierarchy of structures represents the non-linear transfer of energy between different scales.

Richardson (1922) gave for the first time a pictorial representation of such cascade (see Figure 2.1), where the energy is injected in the system at the integral scale (the large scale  $\ell_0$  in the picture) at some rate  $\epsilon$ . Since nonlinear interactions are present, such energy “cascades” through a hierarchy of smaller and smaller structures within the inertial range.

In the Richardson picture, the energy transfer is assumed to have the same rate  $\epsilon$  as the energy injection. At smaller scales the dissipation become

<sup>1</sup>Due to the shape of the nonlinear terms of MHD equations, in MHD this picture is real only when the correlations between velocity and magnetic field  $\mathbf{v} \cdot \mathbf{b}$  are small.

dominant so that the cascade is eventually stopped and the energy is dissipated, always at rate  $\varepsilon$ . The usual tool to study the turbulent cascade is by means of the field increments. Starting with a field  $\psi(\mathbf{r})$  one can define the following variables:

$$\delta\psi_\ell(\mathbf{r}) = \psi(\mathbf{r} + \delta\mathbf{r}) - \psi(\mathbf{r}) , \quad (2.18)$$

where  $\ell = |\delta\mathbf{r}|$ . As can be easily understood, these variables can give informations about the presence of structures in the field at a given scale  $\ell$  (shown in the Figure 2.2). The field increments are stochastic variables, and a statistical approach is needed.

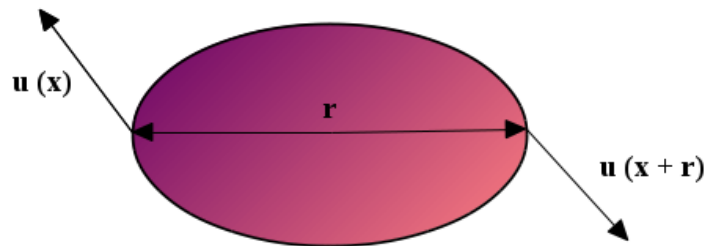


Figure 2.2: A schematic image showing how the field differences can be used to represent the presence of vortical structures. In fact, in correspondence of such structures, the velocity increment computed at the scale of the structure is high when, the velocities being directed in opposite directions at the edges of the eddy.

### 3 Analisis of turbulent field

We will now introduce some well known concepts in order to point out the relationship between the classical tools used for the analysis of turbulent

fields. A statistical approach can provide informations about the physical properties of the system, since we are working with stochastic variables.

### 3.1 Energy spectra

Given a stochastic field  $\psi(\mathbf{r})$ , the Fourier transform of its  $i$ -th component is

$$\psi_i(\mathbf{r}) = \int \hat{\psi}_i(\mathbf{k}) e^{i\mathbf{k}\cdot\mathbf{r}} d^3\mathbf{r} .$$

If homogeneity and isotropy are assumed, the associated energy spectrum is

$$E(k) = 4\pi k^2 U(k)$$

where  $U(k) = |\hat{\psi}(\mathbf{k})|^2/2$ . The energy spectrum is simply related to the autocorrelation function

$$\frac{1}{2} \langle \psi_i(\mathbf{r}) \psi_j(\mathbf{r}) \rangle = \int_0^\infty \mathbf{E}(\mathbf{k}) d\mathbf{k} . \quad (2.19)$$

Energy spectra are a powerful tool for the analysis of turbulence. In fact, they allow a description which is able to capture the main energy cascade features. In particular, it is found that the energy spectrum of a turbulent field has power-law behaviour (Kolmogorov, 1941 [68]; see also Frisch, 1995 [48])

$$E(k) \sim k^{-\alpha} \quad (2.20)$$

within the inertial range of the energy cascade. Figure 2.3 shows an example of spectrum for fluid case. The different ranges described by the Richardson cascade can be easily identified in the spectrum. It is easy to relate the energy spectra to the field increments variance. Using the relation (2.19) and recalling that:

$$\frac{1}{2} \langle \psi_i(\mathbf{r}) \psi_j(\mathbf{r} + \delta\mathbf{r}) \rangle = \int_0^\infty E(k) \frac{\sin k\delta r}{k\delta r} dk ,$$

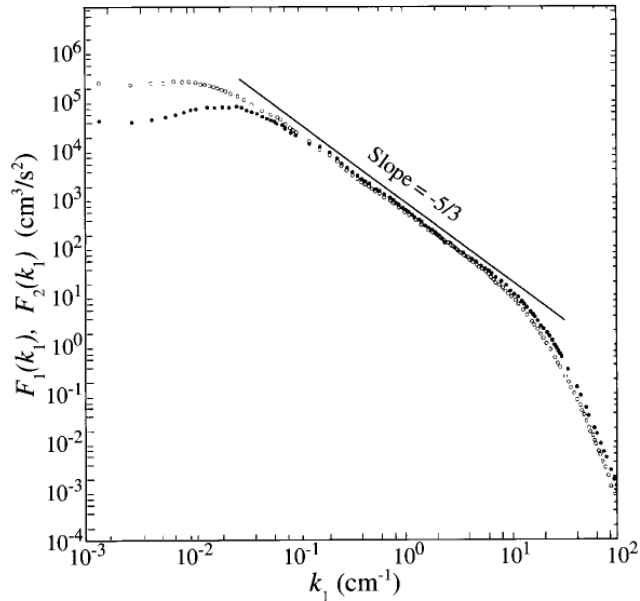


Figure 2.3: The energy spectra of the streamwise component (white circles) and lateral component (black circles) of velocity fluctuations in high Reynolds number jet (from Frisch, 1995 [48]).

it is straightforward to figure out that

$$\langle |\psi_i(\mathbf{r} + \delta\mathbf{r}) - \psi_i(\mathbf{r})|^2 \rangle = 4 \int_0^\infty E(k) \left( 1 - \frac{\sin k\delta r}{k\delta r} \right) dk . \quad (2.21)$$

If the spectrum  $E(k)$  decreases slowly enough (a power law with exponent  $\alpha > 1$ ), then the main contribution to the integral (2.21) comes from  $E(k)$ , at least for scales smaller than the large scale  $\ell_0$ , so that the energy spectrum is directly related to the second order moment of the field increments.

### 3.2 Probability distribution functions (PDFs)

The main statistical tool is the Probability Distribution Function (PDF) of the field increments. We present here some relationship between PDFs and and other quantities such as energy spectra and structure functions. If the

PDF  $P(x)$  of a stochastic variable  $x$  is known, then it is possible to compute the infinite set of moments defined as:

$$\langle x^n \rangle = \int x^n P(x) dx . \quad (2.22)$$

Let us introduce the characteristic function of  $P(x)$ , (its Fourier transform)

$$\Phi(k) = \int e^{ikx} P(x) dx = \langle e^{ikx} \rangle ;$$

using the Taylor series to expand the exponential  $e^{ikx}$ ,

$$\Phi(k) = \int dx P(x) \sum_{m=0}^{\infty} \frac{(ik)^m}{m!} x^m = \sum_{m=0}^{\infty} \frac{(ik)^m}{m!} \langle x^m \rangle , \quad (2.23)$$

Transforming backward to the physical space

$$P(x) = \frac{1}{2\pi} \int dk \sum_{m=0}^{\infty} \frac{(ik)^m}{m!} \langle x^m \rangle e^{-ikx} . \quad (2.24)$$

so that it is possible to compute the PDF of a stochastic variable if all the moments  $\langle x^m \rangle$  are known. Note that for experimental purposes, given the stochastic signal provided by some measurements, it is in principle possible to use the ergodic theorem to compute the moments of the signal without the knowledge of the PDF, as would be required to apply equation (2.25). In fact, by deriving  $n$  times equation (2.23) and putting  $k = 0$ , it is possible to recompute the moments directly from the data even if the PDF is unknown:

$$\langle x^n \rangle = \frac{1}{i^n} \left. \frac{d^n \Phi}{dk^n} \right|_{k=0} . \quad (2.25)$$

Gaussian PDFs are a peculiar case. It is a very interesting PDFs class, both because of its large presence in real systems, and for its statistical properties. In fact it is very easy to show that a Gaussian PDF needs only the first two

moments to be completely determined. The first order moment is the average, and is generally used to translate the PDF so that the new PDF is meanless. The second order moment is the variance  $\sigma^2 = \langle (x - \langle x \rangle)^2 \rangle$ . The Gaussian being an even function, the odd order moments are trivially zero. Let us compute now the even order ( $2n$ ) moments using the relation (2.25). It is well known from the Fourier transformation that the characteristic function of a Gaussian is itself Gaussian, with standard deviation  $\sigma' = 1/\sigma$ :

$$\Phi(k) = e^{-\frac{1}{2}\sigma^2 k^2} .$$

The derivative can be computed using the Hermite polynomials  $H_n(y)$  of order  $n$ , that is:

$$\frac{d^n}{dy^n} e^{-y^2} = (-1)^n e^{-y^2} H_n(y) .$$

Then, using  $y = \sigma k/\sqrt{2}$  the even moments can be written as:

$$\langle x^{2n} \rangle = (-1)^n (-1)^{2n} e^{-y^2} H_{2n}(y) \frac{d^{2n} y}{dk^{2n}} \Big|_{k=0} = (-1)^n 2^{-n} H_{2n}(0) \sigma^{2n} \quad (2.26)$$

that is, all the moments of order larger than two are trivially computed from the variance, or they are zero. So, the Gaussian PDF can be built up knowing only the average and the variance of the stochastic variables, for example using the power spectrum. In other words, energy spectra play the fundamental role in the classical picture of turbulence, where Gaussian PDFs are hypothesized. Of course, for non Gaussian distributions all the infinite set of the moments, is required to build the PDF using equation (2.24), so that the energy spectra lose their key role.

### 3.3 Structure functions

The spectral analysis does not provide a complete description of the statistical properties of the field, unless this has Gaussian PDF. In fact, we have seen that spectra are a representation of the second order moment. For non Gaussian fields, the properties of turbulence can be described using the *longitudinal structure functions* to represent the higher order moments of the field. The structure functions are defined as:

$$S_p(\ell) = \langle \delta\psi_\ell^p \rangle \quad (2.27)$$

where

$$\delta\psi_\ell = [\psi(\mathbf{r} + \ell) - \psi(\mathbf{r})] \cdot \frac{\ell}{\ell}. \quad (2.28)$$

are the longitudinal field increments. The use of structure function will be illustrated in the following pages.

## 4 Phenomenology of turbulence and scaling laws

As described by the Richardson cascade, the phenomenology of turbulence involves some fragmentation process of turbulent structures, which transfer energy through different scales. We describe below the major pillars of the theory of turbulence like Kolmogorov, 1941 [68] for fluids, and then Kraichnan, 1965 [69] for MHD (see also Dobrowolny *et al.*, 1980 [26]), giving the bases for the phenomenological analysis of turbulence.

## 4.1 Scaling laws of MHD

A class of solutions of NS equations has scaling properties (Frisch, 1995 [48]), which are invariant under particular scaling transformations. A similar property is also verified for the solution of MHD equations. Let us consider the ideal (nondissipative) MHD equations:

$$\frac{\partial \rho}{\partial t} + \nabla \cdot (\rho \mathbf{v}) = 0 \quad (2.29)$$

$$\rho \left[ \frac{\partial}{\partial t} + (\mathbf{v} \cdot \nabla) \right] \mathbf{v} = \frac{1}{4\pi} (\nabla \times \mathbf{B}) \times \mathbf{B} - \nabla p \quad (2.30)$$

$$\frac{\partial \mathbf{B}}{\partial t} = \nabla \times (\mathbf{v} \times \mathbf{B}) \quad (2.31)$$

$$\left[ \frac{\partial}{\partial t} + (\mathbf{v} \cdot \nabla) \right] \left( \frac{p}{\rho^\gamma} \right) = 0 . \quad (2.32)$$

Let us now define a typical scale  $\ell$ , a characteristic time  $t$ , the scaling factor  $\lambda$  and the characteristic scaling exponent for the time  $\alpha$ , in order to introduce the scaling transformations. When the scale changes by a factor  $\lambda$ , the time variable changes according to:

$$\ell \longrightarrow \lambda \ell' \quad , \quad t \longrightarrow \lambda^\alpha t' . \quad (2.33)$$

In a similar way, we introduce scaling exponents for the other quantities which appear into the MHD equations

$$\mathbf{v} \longrightarrow \lambda^h \mathbf{v}' \quad , \quad \mathbf{B} \longrightarrow \lambda^\beta \mathbf{B}' \quad , \quad p \longrightarrow \lambda^\nu p' \quad , \quad \rho \longrightarrow \lambda^\mu \rho' . \quad (2.34)$$

Inserting the previous relations (2.33) and (2.34) into the MHD equations, and recalling that  $\nabla \sim 1/\ell$ , we obtain

$$\lambda^{\mu-\alpha} \frac{\partial \rho'}{\partial t'} + \lambda^{\mu+h-1} \nabla' \cdot (\rho' \mathbf{v}') = 0 ,$$

$$\rho' \lambda^{\mu+h-1} \left[ \frac{\partial \mathbf{v}'}{\partial t'} \lambda^h + \lambda^{2h-1} (\mathbf{v}' \cdot \nabla') \mathbf{v}' \right] = -\lambda^{\mu-1} \nabla' p' + \frac{1}{4\pi} (\nabla' \times \mathbf{B}') \times \mathbf{B}' \lambda^{2\beta-1}$$

so that the same scaling factor is found for the whole equations if  $\alpha = 1 - h$ ,  $\mu = 2(\beta - h)$ , and  $\nu = 2\beta$ . Under these conditions, that is, if the scaling for the fields is

$$\begin{aligned} \ell &\longrightarrow \lambda \ell' \quad , \quad t \longrightarrow \lambda^{1-h} t' \quad , \quad \mathbf{v} \longrightarrow \lambda^h \mathbf{v}' \quad , \\ \mathbf{B} &\longrightarrow \lambda^\beta \mathbf{B}' \quad , \quad p \longrightarrow \lambda^{2\beta} p' \quad , \quad \rho \longrightarrow \lambda^{2(\beta-h)} \rho' \quad , \end{aligned} \tag{2.35}$$

then the MHD equations remain invariate, for each value of  $h$  and  $\beta$ . Note that in the incompressible case,  $\rho = \text{const}$ , the scaling exponent is the same for velocity and magnetic field,  $\beta = h$ . The scaling relations (2.35) just obtained reveal that a scaling solution must be expected:

$$\frac{\delta \psi_\ell}{\delta \psi_0} \sim \left( \frac{\ell}{\ell_0} \right)^h$$

( $\psi$  being  $v$  or  $b$ ).

## 4.2 Kolmogorov law

The phenomenological approach to turbulence is mainly based on dimensional analysis and physical considerations. First of all, as we did in the scaling analysis, we need to introduce a typical length  $\ell$ ; the typical values of the fields (say  $\psi$ ) corresponding to such scale can be represented for example by the field increments  $\delta \psi_\ell$ ; a characteristic time  $t_\ell$ , associated to the scale  $\ell$ , is also considered. The basic ingredients are thus typical values of the variables involved in the system. A local (in scale) Reynolds number  $R_\ell = \ell \delta \psi_\ell / \nu$  and the mean energy transfer rate  $\epsilon_\ell$  are also needed. The latter can be defined for fluids:

$$\epsilon_\ell = \frac{1}{2} \frac{\partial}{\partial t} \langle \mathbf{v}(\mathbf{r}) \cdot \mathbf{v}(\mathbf{r} + \ell) \rangle$$

and for plasmas:

$$\varepsilon = \frac{1}{2} (\varepsilon^\pm + \varepsilon^\mp)$$

where the pseudo-energy transfer rates are defined as:

$$\varepsilon^\pm = \frac{1}{2} \frac{\partial}{\partial t} \langle \mathbf{Z}^\pm(\mathbf{r}) \cdot \mathbf{Z}^\pm(\mathbf{r} + \ell) \rangle$$

and take into account both magnetic and kinetic contributions to energy transfer. In the framework of the Kolmogorov theory (K41) for fluids ( $\psi = v$ ), in fully developed turbulence, and within the inertial range, all the statistical properties of the fields depend only on the scale  $\ell$ , on the mean energy dissipation rate  $\varepsilon$ , and on the viscosity  $\nu$  (first Kolmogorov similarity hypothesis). Also,  $\varepsilon$  is supposed to be the common value of the injection, transfer and dissipation rates. Moreover, the dependence on the viscosity only arises at small scales, near the bottom of the inertial range. Under such assumptions, it is possible to compute, by dimensional analysis, the typical energy transfer (or dissipation) rate (for unit mass) as  $\varepsilon \sim \delta v_\ell^2 / t_\ell$ . The time  $t_\ell$  associated to the scale  $\ell$  is the typical time needed for the energy to be transferred on a smaller scale. By dimensional analysis,  $t_\ell \sim \ell / \delta v_\ell$ , so that a scaling law for the field increments can be obtained (Kolmogorov's law):

$$\delta v_\ell \sim \varepsilon^{\frac{1}{3}} \ell^{\frac{1}{3}} \quad (2.36)$$

It turns out, when applying the Kolmogorov law to the integral scale  $\ell_0$ , that  $v_0 \sim \varepsilon^{\frac{1}{3}} \ell_0^{\frac{1}{3}}$ . This relation can be used to eliminate the energy transfer rate from (2.36), so leading to the following scaling law for velocity increments:

$$\delta v_\ell \sim v_0 \left( \frac{\ell}{\ell_0} \right)^{\frac{1}{3}}. \quad (2.37)$$

Recalling the scaling law for the velocity arising from scaling analysis of NS equations (or MHD as in our case), the similarity hypothesis lead to  $h = 1/3$ . Note that, since from dimensional considerations the scaling of the energy transfer rate should be  $\varepsilon \rightarrow \lambda^{1-3h}\varepsilon'$ ,  $h = 1/3$  is the only possible choice to guarantee the scaling invariance of  $\varepsilon$ , required by the similarity hypothesis. At small scales, dissipation (viscosity) is involved. The typical time associated to dissipative effects can be obtained by dimensional analysis as:  $t_\ell^{(\nu)} \sim \ell^2/\nu$ . The scale at which the dissipation terms are comparable with the nonlinear transfer terms is called *Kolmogorov scale*  $\eta$ , and can be simply obtained putting  $t_\ell^{(\nu)} = t_\ell$ , so that

$$\eta \sim \left( \frac{\nu^3}{\varepsilon} \right)^{\frac{1}{4}} \quad (2.38)$$

It is straightforward to translate the dimensional analysis results to spectra. In fact, using the wave vector  $k \sim 1/\ell$ , the previous scaling laws can be written in the wave vector space. In particular, it is possible to introduce the power spectrum  $E(k) \sim \delta v_\ell^2/k$ , so that from the similarity hypothesis the spectrum has a power-law behavior within the inertial range

$$E(k) \sim \varepsilon^{\frac{2}{3}} k^{-\frac{5}{3}}. \quad (2.39)$$

The power law spectrum (2.39) is widely observed in experimental data, and is called the *Kolmogorov spectrum*. Note that in terms of the generic scaling exponent  $h$ , the spectral index is  $\alpha = 1 - 2h$ , so that the choice  $h = 1/3$  leads to the *Kolmogorov spectrum*.

### 4.3 Alfvén effect: the Kraichnan spectrum

When performing dimensional analysis of plasma turbulence, it turns out that the *Alfvén effect*, that is the presence of small scales fluctuations moving along the large-scale magnetic field in opposite directions, modified the interactions between structures. Under the same assumptions as for fluid turbulence, we can compute by dimensional analysis the typical energy flux between scales:

$$\Pi_\ell^\pm \sim \frac{|\delta z^\pm(\ell)|^2}{t_\ell^\pm}$$

$t_\ell$  being the typical duration of the energy transfer. Now, as it can be seen by looking at equations (2.16), the Alfvénic fluctuations propagate in opposite direction along the magnetic field lines, so that the interacting structures are set apart in a time  $t_A \sim \ell/c_A$ , thus modifying the actual interaction time. If the (non linear) eddy turnover time is  $t_{NL}^\pm \sim \ell/\delta z_\ell^\mp$ , then the interaction time results

$$t_\ell^\pm \sim \frac{(t_{NL}^\pm)^2}{t_A^\pm} \sim \frac{\ell c_A}{\delta v^2} \quad (2.40)$$

obtained by considering the number of non linear interactions occurring during a Alfvén time,  $t_{NL}^\pm/t_A^\pm$ , and considering similar scaling behavior between the Elsässer fields and the velocity,  $\delta \mathbf{z}^+ \sim \delta \mathbf{z}^- \sim \delta \mathbf{v}$ . The energy flux, corresponding to the energy transfer rate  $\varepsilon^\pm$ , can thus be written as:

$$\Pi_\ell^\pm \sim \varepsilon^\pm \sim \frac{\delta v^4}{\ell c_A} \quad (2.41)$$

so that the scaling law for the velocity (or magnetic field, or Elsässer fields) is modified by the Alfvén effect

$$\delta v_\ell \sim v_0 \left( \frac{\ell}{\ell_0} \right)^{\frac{1}{4}}. \quad (2.42)$$

that is  $h = 1/4$ . The spectrum is modified accordingly

$$E(k) \sim c_A^{\frac{1}{2}} \varepsilon^{\frac{1}{2}} k^{-\frac{3}{2}} . \quad (2.43)$$

The power law spectrum with Alfvénic effect has spectral index  $\alpha = -3/2$  and is called *Kraichnan spectrum*.

#### 4.4 The structure functions scaling laws

Given the Kolmogorov and Kraichnan scaling laws for fields increments (2.37) and (2.42), it is straightforward to compute the scaling law for the longitudinal structure functions from (2.28):

$$S_\ell^{(p)} = \langle \delta\psi_\ell^p \rangle \sim \ell^{\frac{p}{m}} , \quad (2.44)$$

where  $m = 4$  if Alfvén effect decorrelates the interacting structures, and  $m = 3$  if this effect is negligible. The scaling exponent of the structure functions is then a linear function of the order  $p$ , that is  $\zeta_p = p/m$ . The scaling (2.44) implies the power law scaling of the second order moment, the standard deviation:  $\sigma \sim \ell^{\frac{2}{m}}$ . If the field differences  $\delta\psi_\ell$  have Gaussian distribution, from the expression (2.26) the linear scaling of the structure functions is then obtained:

$$\langle \delta\psi_\ell^{2p} \rangle \sim \ell^{\frac{2p}{m}} .$$

In other words, the Kolmogorov and Kraichnan scalings for the field increments require Gaussian PDFs.

#### 4.5 Self-similarity and the scaling of PDF shape

Van Atta & Park (1975) [131] describe the scaling of the PDFs for self-similar fields. Here we present their argument supporting their studies. Given

the self-similar signal  $u(t)$ , let  $h$  be the self-similarity parameter, so that

$$\delta u_T \sim \lambda^{-h} \delta u_{\lambda T} . \quad (2.45)$$

The cumulative PDF of  $\delta u$  is

$$\mathcal{P}\{\delta u_T \leq \xi\} = \mathcal{P}\{\lambda^{-h} \delta u_{\lambda T} \leq \xi\} = \mathcal{P}\{\delta u_{\lambda T} \leq \lambda^h \xi\}$$

written in integral form:

$$\int_{-\infty}^{\xi} P_T(\eta) d\eta = \int_{-\infty}^{\lambda^h \xi} P_{\lambda T}(\beta) d\beta \quad (2.46)$$

where  $P_T$  is the PDF of the field increments  $\delta u_T$ . Using the relation:

$$\frac{\partial}{\partial \alpha} \int_{\phi_1(\alpha)}^{\phi_2(\alpha)} F(x, \alpha) dx = \int_{\phi_1(\alpha)}^{\phi_2(\alpha)} \frac{\partial F}{\partial \alpha} dx + \frac{d\phi_2}{d\alpha} F(\phi_2, \alpha) - \frac{d\phi_1}{d\alpha} F(\phi_1, \alpha)$$

and, recalling that  $\frac{d\phi_1}{d\alpha} = 0$ , and  $\frac{\partial P_T}{\partial \xi} = 0$ , we obtain from equation (2.46) the scaling relation for the PDFs of the field increments of a self-similar process:

$$P_T(\xi) = \lambda^h P_{\lambda T}(\lambda^h \xi) . \quad (2.47)$$

That means that when the scale changes by a factor  $\lambda$ , the amplitude of the increments varying by the factor  $\lambda^h$  for the self-similarity, the shape of the PDFs of different scales increments do not change shape if  $h$  has a constant value. If the value of  $h$  is not known, as is often the case for experimental PDFs of turbulent data, or not unique, which is true for non self-similar fields, it is however possible to compare the PDFs at different scales by normalizing them in a suitable way. Let us consider the PDF  $P_T(y)$  for which the relation (2.47) holds, and let  $\sigma_T$  be the standard deviation of  $y = \delta u_T$ . Then, introducing the standardized variable  $x = y/\sigma_T$ ,

$$\mathcal{P}\{x \leq z\} \equiv \mathcal{P}\{y \leq \sigma_T z\} = \int_{-\infty}^{\sigma_T z} P_T(y) dy .$$

Using self-similarity

$$\sigma_{\lambda T} = \lambda^h \sigma_T \quad , \quad (2.48)$$

and using the relations 2.47 and 2.48, we obtain:

$$f_{z_1} \equiv \sigma_T P_T(\sigma_T z) = \sigma_T \lambda^h P_{\lambda T}(\lambda^h \sigma_T z) = \sigma_{\lambda T} P_{\lambda T}(\sigma_{\lambda T} z) \equiv f_{z_2} \quad . \quad (2.49)$$

This relation allows to test for self-similarity by looking at the plot of  $\sigma P$  vs.  $\delta u/\sigma$ . When plotted in this form, the PDFs must superimpose if self-similarity is present. For this reason, it is always convenient to use the standardized variables  $\delta u'_T = \delta u_T/\sigma_T$  when comparing PDFs at different scales, so that, being  $\sigma'_T = 1$ , there is no need to normalize the PDFs.

To resume, self-similar fields has identical PDFs for the normalized increments at different scales. The departure from self-similarity can be seen as rescaling of the PDFs shape with the scale.

## 5 Intermittency

### 5.1 The problem of intermittency in turbulence

The Kolmogorov scaling, represented by the linear dependence of structure functions on the scaling exponent, and by the gaussianity of the PDFs of increments, is not observed in experimental data. The only exception is the  $-5/3$  spectrum which is observed everywhere in turbulence. The Kolmogorov theory (Kolmogorov, 1941 [68]), hereafter K41, includes the main fundamentals for the turbulence studies, which however need further development in the approach to turbulence (Frisch, 1995 [48]). As far as the experimental analysis was dealing with spectral analysis, the K41 theory worked well, because only the second order moment behavior was investigated. But

when the more and more accurate experimental techniques permitted the investigation of higher moments, the need for a different interpretation arised. The most discussed point, has been the uniform distribution of the energy transfer rate along the cascade, supposed by the K41 model (Landau & Lifshitz, 1987 [70]). The shape of the field increments PDFs changes with the scale in the experimental results for fully developed turbulence. The PDFs at large scales are generally nearly Gaussians, but the tails of the PDFs become higher and higher when the scale decreases. As a consequence, the moments, represented by the structure functions, scale in a different way, and this is visible by looking at their scaling exponents, which differ from the K41 prediction  $\zeta_p = p/3$ . The presence of large values of the fields increments with higher probability than in a Gaussian statistics, makes possible this peculiar behaviour. In other words, the signal is characterised by the presence of strong fluctuations in some regions of space. This is why the field fluctuations are a *intermittent* signal. In general, this kind of signals are not purely self-similar. In Figure 2.4 an example of *self-similar* signal is presented. This kind of signal displays the same statistical properties independently on the scale at which is observed. Moreover, it is similar for each region we observe. The K41 theory would lead to such a signal, for which the PDF shape would not change with the scale. On the contrary, Figure 2.5 shows a simple example of intermittent signal: the *devil staircase*, characterised by “active” zones alternated with flat regions. That is, the self-similarity of the signal in this last case depends on the position.

To understand the concept of intermittency in turbulent fields, the picture of the Richardson cascade (see previous Figure 2.1), presented to introduce

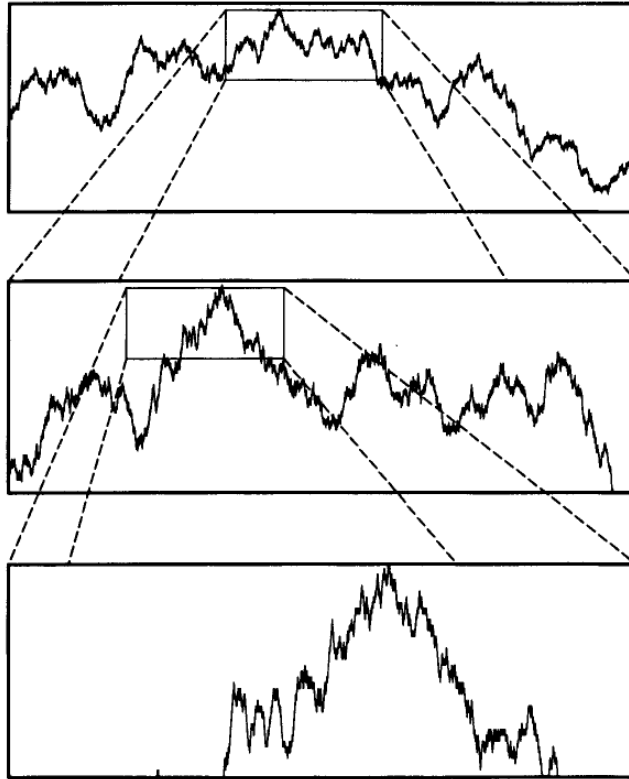


Figure 2.4: An example of self-similar signal: the brownian motion. The signal shows the same statistical properties everywhere and at all scales. The zoomed segments of signal repeat the large scale behavior in all positions (from Frisch, 1995 [48]).

turbulence, can be modified. K41 theory is based on the main point that the non linear cascade is controlled by the mean energy transfer rate  $\varepsilon$ . The actual spatial distribution of  $\varepsilon$  does not come into play at that level, the idea of universality implied by the model suggesting a uniform distribution. In the intermittent case, however, we should restate that only the *global* mean value of the energy transfer rate is constant through the cascade, while its local value can be a (stochastic) fluctuating function, presenting bursty and quiet zones alternatively. Moreover, the presence of strong activity regions is

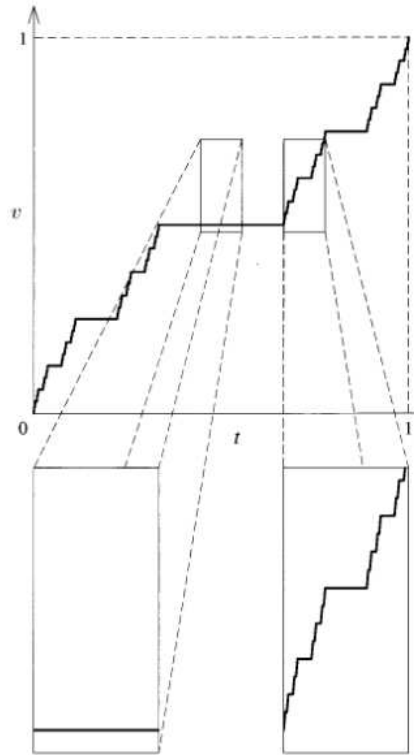


Figure 2.5: The devil staircase: an intermittent signal. The statistical properties of the signal change when we look at different scales, in different positions. The zoomed fragments of signal can be active or flat, depending on the position, and are in general different from the large scale (whole signal), which includes both (from Frisch, 1995 [48]).

scale-dependent, as can be visualized in Figure 2.6.

This modified Richardson cascade picture shows the concentration of active structures on definite positions of the space, and such concentration becomes more and more evident as the scale decreases.

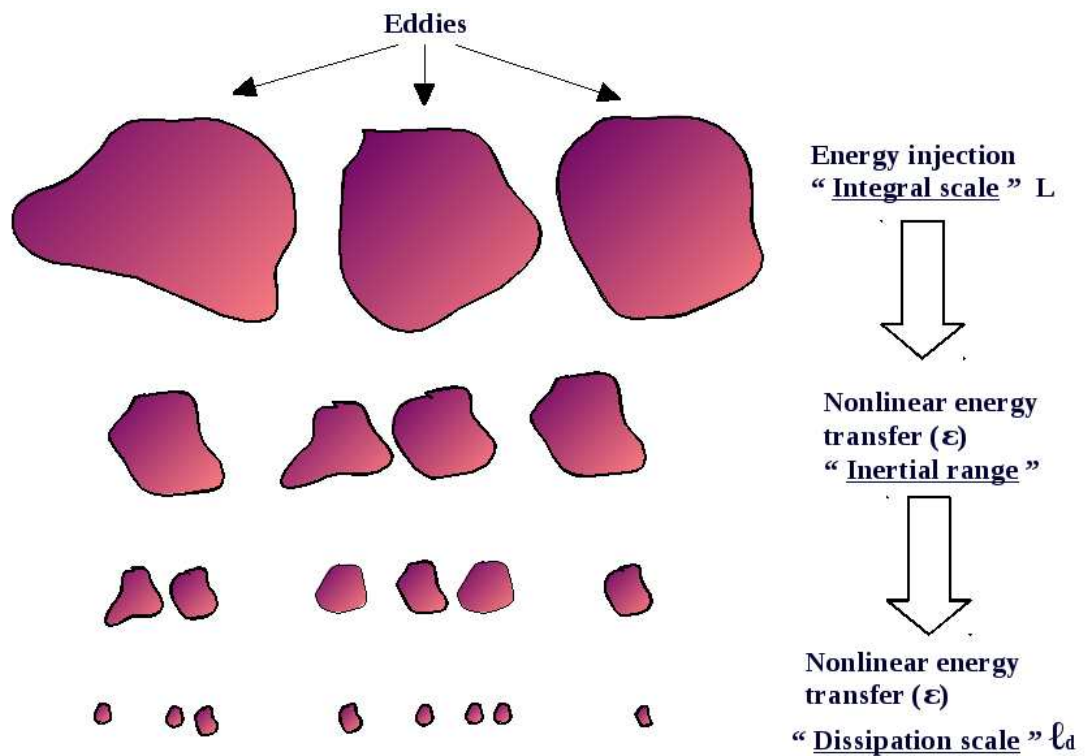


Figure 2.6: A schematic picture of the intermittent Richardson cascade. The local differences of transfer of energy are represented by concentration of active structures in regions of the space. At the dissipative scales, the dissipation field is bursty and intermittent.

## 5.2 The multiplicative cascade, fractal and multifractal models

The first correction to the K41 theory has been made by Kolmogorov himself in 1962, and is so called K62 (Kolmogorov, 1962 [67]). In this model, the local variations of the energy transfer rate are taken into account, so that  $\varepsilon_\ell(x)$  is now the value of the energy transfer rate averaged on a ball of radius  $\ell$  centered in  $x$ :

$$\varepsilon_\ell(x) = \frac{1}{\ell^3} \int_x^{x+\ell} \varepsilon(t) dt ,$$

its distribution is *log-normal*, and its variance follows a logarithmic scaling law:  $\sigma_{\log \varepsilon_\ell} = A + B \log(\ell_0/\ell)$ . As for the K41, the global mean energy transfer rate remains constant for each scale, all along the cascade, from injection to dissipation. It is possible to give a justification for the log-normal choice by considering the cascade as a multiplicative process. In that view, the local transfer of energy is considered as a random variable, for example uniformly distributed in some interval. Given the integral scale ( $\ell_0$ ) energy transfer rate  $\varepsilon_0$ , the energy transfer rate at a generic smaller scale  $\varepsilon_n = \varepsilon_{\ell_n}$ , where  $\ell_n = 2^{-n}\ell_0$ , can be then computed as the result of a multiplicative cascade

$$\varepsilon_n = \varepsilon_0 \prod_{i=1}^n \beta_i ,$$

the multiplicative factors  $\beta_i$  being random variables. Taking the logarithm of both sides of last relation:

$$\ln \varepsilon_n = \ln \varepsilon_0 + \sum_{i=1}^n \ln \beta_i .$$

When the steps number  $n$  is large enough, the central limit theorem can be applied, so that a log-normal distribution for  $\varepsilon_n$  is obtained. In terms of structure functions scaling exponents, the log-normal model provides

$$S_p(\ell) \sim \ell^{\frac{p}{m} + \frac{1}{18}\mu p(3-p)} ,$$

where  $\mu$  is a scale dependent parameter. This scaling law is more suitable to fit the experimental results than the linear prediction, but still the accord is not good. Besides experimental evidences, at large  $p$  the K62 model failed because of many problems, as claimed by Yaglom and other authors. Anyway, the idea underlying the multiplicative cascade has been used for many of the

models built up to describe intermittency. One of the first models is the  $\beta$ -*model* (Frisch *et al.*, 1978 [48]). The main idea underlying this model is that for each step of the energy cascade the volume of space occupied by active structures is a fraction  $0 < \beta < 1$  of the volume occupied by the parent generation. This is again a multiplicative process. If the scale at the step  $n$  is given by  $\ell_n = \ell_0 k^n$  (where  $0 < k < 1$  is a step factor, for example  $k = 0.5$ ), then the fraction of space where active structures lie at such step is  $\beta^n$ . The step number  $n$  can be rewritten as  $n = \ln(\ell_n/\ell_0)/\ln k$ , so that the active fraction of space can be written as

$$p_n = \beta^{\frac{\ln(\ell_n/\ell_0)}{\ln k}} = \left(\frac{\ell_n}{\ell_0}\right)^{\frac{\ln \beta}{\ln k}}.$$

The exponent  $\frac{\ln \beta}{\ln k} = 3 - D$  represents the *fractal dimension*  $D$  of the space occupied by active structures at the step  $n$ ,

$$p_n = \left(\frac{\ell_n}{\ell_0}\right)^{3-D}.$$

It is clear that the energy is transferred to smaller scales only in a subset  $S$  of the space, of fractal dimension  $D$ , so that

$$\varepsilon_n(x) \sim \begin{cases} \ell_n^D & \text{if } x \in S \\ 0 & \text{if } x \notin S \end{cases} \quad (2.50)$$

Considering that the energy transfer is  $\varepsilon_n \sim \frac{\delta v_{\ell_n}^3}{\ell_n} \left(\frac{\ell_n}{\ell_0}\right)^{3-D}$ , the velocity increments scaling law becomes:

$$\delta v_\ell \sim \delta v_0 \left(\frac{\ell}{\ell_0}\right)^{\frac{1}{m} - \frac{3-D}{3}}.$$

The scaling exponent  $h = 1/m - (3 - D)/3$  leads to the following law for the structure functions scaling exponents:

$$S_p(\ell_n) \sim \delta v_0^p \left(\frac{\ell}{\ell_0}\right)^{\zeta_p}, \quad \zeta_p = \frac{p}{m} + (3 - D) \left(1 - \frac{p}{m}\right).$$

Since  $\zeta_p$  from the  $\beta$ -model is a linear function of the order  $p$ , the model cannot describe the experimental data. In particular, this means that the shape of the increments PDFs, even if it is no longer Gaussian, does not change with the scale. Anyway, the model is very important because of the introduction of the concept of fractal dimension of the structures. In fact, a further step can be done and the *multifractal* model can be introduced starting from the idea of the fractal  $\beta$ -model.

The multifractal idea is to consider a continuous spectrum of possible values of the scaling exponent  $h$ , as for the scaling of the equations. That is, the space can be considered as composed by an infinite number of subsets  $S_h$ , each one of fractal dimension  $D(h)$ , and on each of which the scaling is described by the exponent  $h$  (Frisch & Parisi, 1994). Summing together all the subspaces contribution to the scaling of the fields gives:

$$\delta v_\ell(x) \sim \delta v_0 \left( \frac{\ell}{\ell_0} \right)^h, \quad x \in S_h.$$

The structure functions can now be considered as the superposition of infinite power-laws, each one representing the set where its exponent is valid:

$$S_p(\ell) \sim \delta v_0^p \int_{h_{min}}^{h_{max}} \left( \frac{\ell_n}{\ell_0} \right)^{ph+3-D(h)} d\mu(h).$$

$\mu(h)$  being the measure representing the probability distribution function of the exponents  $h$ . The integral can be solved exactly with the saddle point method and leads to

$$\zeta_p = \inf_h [ph + 3 - D(h)].$$

From an heuristic point of view, this can be understood by noting that, since  $(\ell/\ell_0) \ll 1$ , the leading exponent for each value of the order  $p$  is the

minimum allowed. This behavior is not determined, since it needs of course some assumption on the measure  $\mu$  (Paladin & Vulpiani, 1987).

Many of the models developed to describe intermittency are multifractal, as for example the *random  $\beta$ -model* (Benzi *et al.*, 1984 [10]), the *She and Lévéque model* (She & Lévéque, 1994 [111]) and the *p-model* introduced by Meneveau and Sreenivasan, 1987 [87].

The *random  $\beta$ -model* assumed that  $\beta$  is a random variable instead of being a constant. It was the first multifractal multiplicative model able to fit the scaling exponent of the structure functions. In that model, at a scale  $\ell_n$  there are  $N_n$  mother eddies. The daughter eddies of size  $\ell_{n+1}$  cover a fraction  $\beta_{n+1}(k)$  of the mother  $k$ , with  $k = 1, \dots, N_n$ . The velocity increment at a scale  $\ell_n$  is given by the typical velocity  $v_n(k)$  of the corresponding eddy whose lifetime is  $\tau \sim \frac{\ell_n}{v_n}$ . The energy transfer rate is therefore

$$\epsilon_n \sim \frac{v_n^3}{\ell_n}.$$

As a consequence that the energy transfer is constant throughout the cascade, one has

$$\frac{v_n^3}{\ell_n} = \beta_{n+1}(k) \frac{v_{n+1}^3}{\ell_{n+1}}.$$

After  $n$  cascade steps, an eddy is individuated by a particular history of fragmentation (i.e. a sequence of random variables  $\beta_1, \dots, \beta_n$ ), so that it covers a fraction of the fluid volume  $\prod_i \beta_i$ . Assuming that the  $\beta_i$ 's are independent, identically distributed random variables, the structure function  $\langle v_n^p \rangle$  scale with exponents

$$\zeta_p = -\frac{p}{3} - \log_2 \bar{\beta}^{1-p/3}, \quad (2.51)$$

where the overbar indicates the average over the probability distribution of  $\beta$ . If  $\beta$  is a constant, i.e.  $\beta_n(k) = 2^{D-3}$  for all  $n$  and  $k$ , one recovers the results of the beta model. Phenomenological arguments suggest restricting the choice of the  $\beta$  probability distribution to a dichotomic distribution with a free parameter  $x$ :

$$P(\beta) = x\delta(\beta - 1) + (1 - x)\delta(\beta - 2^{3h_{min}-1}) . \quad (2.52)$$

The two limiting case are  $x = 1$ , corresponding to the K41 theory, and  $x = 0$ , corresponding to the usual beta model, where the end of the cascade the energy dissipation concentrates on a fractal structure with dimension

$$D = 2 + 3h_{min} .$$

She and L ev eque proposed a different random multiplicative model with a hierarchy of fluctuation structures associated with vortex filaments. The resulting formula for the exponents of the structure functions

$$\zeta_p = -\frac{p}{9} + 2 - 2\left(\frac{2}{3}\right)^{p/3} , \quad (2.53)$$

corresponds to assuming that the energy transfer rate has a log-Poisson distribution (Dubrulle, 1994 [30]), and can be obtained from the random- $\beta$  model by taking in the equation (2.52) the simultaneous limits  $x \rightarrow 1$  and  $n(1 - x) = C$  when the cascade step  $n \rightarrow \infty$ . In other words the probability  $x$  of having a space-filling eddy fragmentation of Kolmogorov depends on the length scale and tends to unity for the lowest eddy size considered.

Meneveau and Sreenivasan presented in 1987 a simple model to describe the energy-cascading process in the inertial range, that fits remarkably well

the entire spectrum of scaling exponents for the dissipation field in fully developed turbulence. In the so-called “p-model” (Meneveau and Sreenivasan, 1987 [87]) a one-dimensional (1D) spatial distribution of the energy flux at different spatial scales, is reconstructed through a multiplicative process. Each eddy breaks down into two new ones. This cascade terminates when the eddies are of the size of the Kolmogorov scale  $\eta$  (Figure 2.7). This version

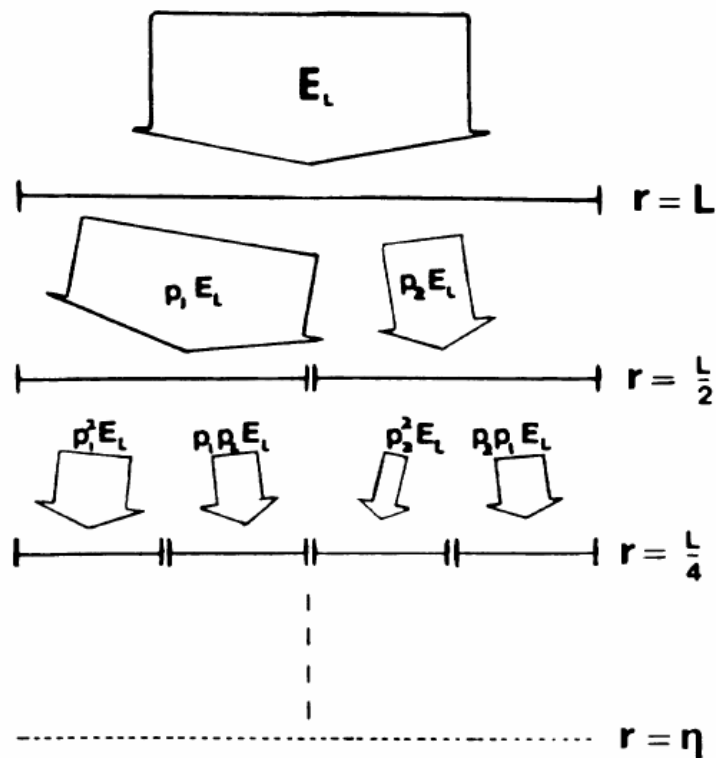


Figure 2.7: Fig.1 One-dimensional version of a cascade model of eddies (Meneveau and Sreenivasan, 1987 [87])

is a simple generalized two-scale Cantor set (Halsey *et al.*, 1986 [53]), with equal scales but unequal weights. Thus, an eddy at a given scale  $\ell$  breaks in two eddies at the scale  $\ell/2$ , and the energy flux  $\epsilon$  associated with the parent eddy is unequally distributed to the two daughter eddies, with fractions given

by  $2p\epsilon$  and  $2(1-p)\epsilon$ , respectively, with  $0.5 \leq p \leq 1$ . Thus, going from larger to smaller scales, the energy flux tends to become more and more spatially localized. This feature reproduces the increasing structure localization at smaller scales, which is typical of intermittency.

## 6 Summary

In this chapter we have introduced the main concepts of magnetohydrodynamics (MHD) and turbulence. We have given an overview of different ways to study the plasma system and after we have described in more details the MHD theory, discussing the corresponding equations. The attention was focused on the statistical properties of velocity and magnetic fields, as well as on the tools used to describe them. The main characteristic of this sets of equations is the presence of nonlinear terms similar as in the fluid equations, and extra terms describing the coupling between velocity and magnetic field. These nonlinearities are responsible for scaling properties of the equations, which is prelude to turbulence. As described by the Richardson cascade, the phenomenology of turbulence involves some fragmentation process of turbulent structures, which transfers energy through different scales. We have described the major pillars of the theory of turbulence like the theory by Kolmogorov (1941) for fluids, and by Kraichnan (1965) for the MHD case, giving the bases for the phenomenological analysis of turbulence. We have seen that intermittency is linked to the presence of structures, and can modify the statistics of the fields increments. The rest of the chapter was devoted to the characterization of intermittency and of such structures. Finally, fractal and multifractal models were presented to understand how the intermittency

phenomenon can be explain throughout multiplicative processes.

In the next chapter we will present and discuss in details a new model of synthetic turbulence, i.e., a numerical model which generates a turbulent field whose statistical properties are similar to those of a real turbulent system, which we have described in the present chapter.

# Chapter 3

## Synthetic Turbulence

As we discussed in the previous chapter, the dynamics of different kinds of fluids is characterized by turbulence. It plays a key role in determining various phenomena for the very efficient transfer of energy across scales, establishing the connection between the macroscopic flow and the microscopic dissipation of its energy. Turbulence represents an universal phenomenon with a peculiar property represented by intermittency (Frisch, 1995 [48]). Considering the increments  $\Delta\mathbf{v}(\mathbf{x}, \mathbf{X}) = \mathbf{v}(\mathbf{x} + \mathbf{X}) - \mathbf{v}(\mathbf{x})$  of a turbulent field  $\mathbf{v}$  at a given displacement  $\mathbf{X}$  for all the possible positions  $\mathbf{x}$ , their statistical distribution  $f(\Delta\mathbf{v})$  is not self-similar at all the scales  $\ell = |\mathbf{X}|$ . In particular,  $f(\Delta\mathbf{v})$  is essentially Gaussian at large scales, while for decreasing  $\ell$  the tails of the distribution  $f(\Delta\mathbf{v})$  become more and more significant, indicating that fluctuations with amplitude much larger than the root mean square value become more and more frequent, with decreasing the scale  $\ell$ . Nonlinear dependence of scaling exponent  $\zeta_q$  of structure functions  $S_q(l)$  of order  $q$ , prove the lack of self-similarity, where  $S_q(\ell) \propto \ell^{\zeta_q}$  being the  $q$ -order moment of the distribution  $f(\Delta\mathbf{v})$  at the scale  $\ell$  (Frisch, 1995 [48]).

In consequence of intermittency, large-amplitude fluctuations at small scales

appear to be localized in space. It has been assumed that intermittency is a consequence of a spatially nonuniform spectral energy flux. An intermittent signal is a function that manifests activity only in certain regions of space or take place over a period of time that decrease with the scale. According to the definition, Gaussian signals are not intermittent just as signals, that satisfy the Kolmogorov's theory (Kolmogorov, 1941 [68]). In this respect it is also noted that the fluctuating energy tends to concentrate at locations where the spectral flux is larger. Energy localization becomes more noticeable at smaller scales due to a cumulative effect. Most of the models for the description of intermittent turbulence are based on this idea. Examples are the random- $\beta$  model (Benzi *et al.*, 1984 [10]), the She and L ev eque model (She & L ev eque, 1994 [111]), and the  $p$ -model (Meneveau and Sreenivasan, 1987 [87]), as mentioned under Chapter 2 above.

## 1 State of the art and previous models

Models built up over time have been aimed at reproducing the main features of turbulence including intermittency. A natural way to obtain a representation of turbulence is by direct simulations in which a numerical solution of fluid equations, within a given spatial domain, is calculated starting from suitable initial conditions. Like every approaches, it presents advantages and drawbacks. The main advantage consists in being based on first principles (such as mass, momentum, and energy conservation); in particular, direct simulations of both fluid and MHD equations reproduce intermittency self-consistently. The main limitation is the finite space resolution, which determines the extension of the range of spatial scales. This disadvantage can

become very severe in 3D configurations: for high-Reynolds number fluids, as typically happens in astrophysical contexts, realistic simulations would require huge computational efforts. It is very important to address this problem and a step in this direction is represented by the so-called “synthetic turbulence”. In particular, we built up a new synthetic turbulence model, which will be described and discussed in detail in the remainder of the present chapter. The model has been presented in a paper (Malara *et al.*, 2016 [75]), and an application of the model to transport of particles in a turbulent magnetic field is given in Pucci *et al.*, 2016 [99]. The main advantage of this approach is its reduced computational requirement with respect to direct simulations. This allows to represent, for instance, spatial scale ranges that are larger than in direct simulation, but employing smaller computing resources. Synthetic turbulence is able to reproduce the main properties of a turbulence field starting from simplified models that mimic the processes taking place in real turbulence. It can be also useful in specific context, such as understanding fundamental scaling properties of turbulence (Juneja *et al.*, 1994 [61], Arneodo *et al.*, 1998 [5]); describing processes that involve very different spatial scales (e.g., particle transport or acceleration, diffusion, and drop formation) (Sardina *at al.*, 2015 [108]); evaluating subgrid stresses (Scotti and Meneveau, 1999 [110], Kerstein *et al.*, 2001 [63], McDermott *et al.*, 2005 [86]) and generating initial conditions for numerical simulations (Rosales and Meneveau, 2006 [103]). Different methods to generate synthetic turbulence have been conceived with different features, in according to the applications they are designed for (Bensi *et al.*, 1993 [9], Biferale *et al.*, 1998 [11]). Juneja *et al.* [61] presented a “wavelet-based” model, which produces a function with the sta-

tistical properties of a signal measured along a line in a turbulent field; in particular, intermittency is reproduced with a multiplicative procedure and has the same properties as those of turbulent energy dissipation rate  $\epsilon$ . This scheme was implemented in one dimension. A generalization in three dimensions of such a model has been proposed by Cametti *et al.*, 1998 [16], where a spatially localized 3-D structures are superimposed at different scales. The amplitude of each structure is chosen in order to reproduce a given spectrum and the spectral energy flux is determined by a multiplicative process similar to the p-model. 3D models obtained by a superposition of random-phased Fourier modes with a given spectrum have been used to study transport processes in turbulent magnetic fields (Zimbardo *et al.*, 2000 [139], Ruffolo *et al.*, 2006 [105]); such models can include spectral anisotropy, but phase randomness does not allow for the inclusion of intermittency. Time dependence has been included in a 1D model by Lepreti *et al.*, 2006 [72], where time variation is obtained by means of an associated shell model. A minimal Lagrangian map method has been proposed by Rosales & Meneveau, 2006 [103] and also 2008 [102], to reproduce 3D hydrodynamic turbulence. The procedure is a simple method for generating synthetic vector fields. Using a sequence of low-pass filtered fields, fluid particles are displaced at their rms-speed for some scale-dependent time interval, and then interpolated back to a regular grid. Fields produced in this way are seen to possess certain properties of real turbulence. A recent generalization to the MHD case has been presented by Subedi *et al.*, 2014 [125]. Finally, a method to reconstruct a 3D magnetic turbulence with nearly constant magnetic field intensity and a prescribed spectrum has been proposed by Roberts, 2012 [101].

In this work we present a new model of synthetic turbulent field, which belongs to the class of “wavelet-based” models (Juneja *et al.*, 1994 [61]). Our model has many aspects similar to the model by Cametti *et al.*, 1998 [16], but with important differences. The model by Cametti *et al.* suffers from strong limitations due to large memory requirements when increasing the range of spatial scales. Through employing a different algorithm our model allows us to reproduce very large ranges of spatial scales with very low memory requirements and short computational times. This feature is very important in all the cases in which a high-Reynolds-number turbulence is to be represented, as typically happens in astrophysical applications.

## 2 Description of the model

We have built up a new model of synthetic turbulence, which will be described and discussed in detail in the following. The model has also been presented in a recent paper (Malara *et al.*, 2016 [75]). An application of our model to the problem of energetic particle transport in a turbulent magnetic field is described in the paper by Pucci *et al.* 2016[99].

Our synthetic turbulence model generates a three-component solenoidal time-independent turbulent field, which will be denoted by  $\mathbf{v} = \mathbf{v}(\mathbf{x}) = (v_x, v_y, v_z)$ . The field is defined within a 3D spatial domain in the form of a parallelepiped  $D = \{\mathbf{x} = (x, y, z)\} = [0, L_x] \times [0, L_y] \times [0, L_z]$ . Periodicity is imposed on all the boundaries of the domain  $D$ . The velocity field is obtained as a suitable superposition of localized “basis functions”, each of which represents an eddy characterized by its spatial scale  $\ell$ , position, amplitude, and spatial profile to simulate the turbulent cascade. The scales  $\ell$  have discrete values  $\ell_m$  that span

a range corresponding to the inertial range of the turbulence. The amplitudes of the eddies are derived taking into account both their relationship with the average spectral energy flux and the intermittent character of the local energy flux.

## 2.1 Spectrum and cell hierarchy

To simulate the process of the eddy breaking within the turbulent cascade, we build a hierarchy of cells at different spatial scales. Each scale is identified by the (integer) index  $m = 0, \dots, N_s$ , where  $N_s$  is the number of scales included in the model. Each cell roughly corresponds to the support of a localized function representing an eddy. At the largest scale, identified by the index  $m = 0$ , there is only one cell, which coincides with the whole domain  $D$ ; thus, the corresponding typical size is  $L_0 = (L_x L_y L_z)^{1/3}$ . The cells at the next scale  $m = 1$  are obtained by dividing all the edges of  $D$  in two equal parts, thus obtaining eight equal parallelepipeds, each occupying  $1/8$  of the volume of  $D$ . Such a process is recursively repeated a number  $N_s$  of times. Thus, at the  $m$ th scale, the cell size is

$$\ell_{x,m} = 2^{-m} L_x, \quad \ell_{y,m} = 2^{-m} L_y, \quad \ell_{z,m} = 2^{-m} L_z \quad (3.1)$$

along  $x$ ,  $y$  and  $z$ , respectively, with  $m = 0, \dots, N_s$ . At the  $m$ -th scale, the domain is divided into  $2^{3m}$  cells, each occupying a volume  $V_m = 2^{-3m} L_0^3$  and with a typical size

$$\ell_m = (\ell_{x,m} \ell_{y,m} \ell_{z,m})^{1/3} = 2^{-m} L_0 \quad (3.2)$$

It is especially important to note that every cell at any scale present the same aspect ratio as the domain  $D$ ; At any given scale  $m$ , all the cells form a  $3D$

lattice filling the whole domain  $D$ . We indicate the cells by

$$C^{(i,j,k;m)} = \{(x, y, z)\} = [(i-1)\ell_{x,m}, i\ell_{x,m}] \times [(j-1)\ell_{y,m}, j\ell_{y,m}] \times [(k-1)\ell_{z,m}, k\ell_{z,m}] \quad (3.3)$$

Hereafter the indexes  $i, j, k = 1, \dots, 2^m$  will identify the cell position within the 3D lattice at the  $m$ -th scale. The total number of cells contained in the model is indicated by

$$N_{cell} = \sum_{m=0}^{N_s} 2^{3m} \quad (3.4)$$

Note that in the models by Juneja *et al.* [61] and Cametti *et al.* [16], no cell hierarchy is used because each eddy can occupy any position within the spatial domain.

Size of the cells at the smallest scale is of the order of  $\ell_{N_s} = 2^{-N_s} L_0$ .

We assume that the eddy amplitudes are non-vanishing in the range of scales  $\ell_I \leq \ell_m \leq \ell_d$ , where  $\ell_I = 2^{-m_I} L_0$  and  $\ell_d = \ell_{N_s}$  correspond to the energy injection scale and to the dissipative scale, respectively. Such a range represents the inertial range of the turbulence. In order to have statistical homogeneity, the injection scale  $\ell_I$  must be sufficiently smaller than the largest scale  $\ell_0$ ; we set  $m_I = 2$ , corresponding to  $\ell_I/\ell_0 = 1/4$ . An important parameter of the model is the spectral width  $r$  defined as the ratio

$$r = \ell_I/\ell_d = 2^{N_s - m_I} \quad (3.5)$$

Within the inertial range, the mean fluctuation amplitude  $\Delta v_m$  at the scale  $\ell_m$  follows a power law

$$\Delta v_m = \Delta v_I \left( \frac{\ell_m}{\ell_I} \right)^h \quad (3.6)$$

where  $\Delta v_I$  is the fluctuation amplitude at the injection scale  $\ell_I$ . The exponent  $h$  is equal to  $1/3$  in the case of a Kolmogorov spectrum. As usual, an expression for the dissipative scale can be found by imposing that at the scale  $\ell_d$  the nonlinear time  $\tau_{nl}(\ell) = \ell/\Delta v(\ell)$  is equal to the dissipative time  $\tau_d(\ell) = \ell^2/\nu$ , where  $\nu$  is the dissipative coefficient. Using the relation (3.6), this gives

$$\ell_d \sim \left( \frac{\nu}{\Delta v_I} \right)^{\frac{1}{1+h}} \ell_I^{\frac{h}{1+h}} = \frac{\ell_I}{Re^{\frac{1}{1+h}}} \quad (3.7)$$

where  $Re = \Delta v_I \ell_I/\nu$  is the Reynolds number. From equation (3.7), using the relation (3.5) the Reynolds number  $Re$  can be related to the ratio  $r$  and to the parameters of the model:

$$Re \sim \left( \frac{\ell_I}{\ell_d} \right)^{1+h} = r^{1+h} = 2^{(N_s - m_I)(1+h)} \quad (3.8)$$

The tests of the model described in the next section have been performed using  $N_s = 16$ . This corresponds to a spectral width  $r = 2^{14} \simeq 1.6 \times 10^4$  giving a spectrum more than 4 decades wide. Using equation (3.8) with  $h = 1/3$  this gives an estimation for the Reynolds number  $Re \sim 2^{56/3} \simeq 4 \times 10^5$ . This value of  $Re$  is more than two orders of magnitude larger than what can be typically reached in 3D direct simulation with present day standard computational resources.

## 2.2 Eddy structure

The turbulent field is modeled as a superposition of spatially-localized eddies. Each eddy is associated with a cell, so that the total number of eddies coincides with  $N_{cell}$ . We indicate by  $\Delta \mathbf{v}^{(i,j,k;m)}$  the field of the eddy associated with the cell  $C^{(i,j,k;m)}$ . Since the field is solenoidal, we write it in

terms of a vector potential  $\Psi^{(i,j,k;m)}$ :

$$\Delta \mathbf{v}^{(i,j,k;m)}(\mathbf{x}) = \nabla \times \Psi^{(i,j,k;m)}(\mathbf{x}) = a^{(i,j,k;m)} \nabla \times \Phi^{(i,j,k;m)}(\mathbf{x}) \quad (3.9)$$

where the vector function  $\Phi^{(i,j,k;m)}$  determines the spatial form of the field  $\Delta \mathbf{v}^{(i,j,k;m)}$ . We choose the order of magnitude of  $\nabla \times \Phi^{(i,j,k;m)}$  such as

$$|\nabla \times \Phi^{(i,j,k;m)}(\mathbf{x})| \sim 1 \quad (3.10)$$

for any scale  $m$ . With this choice, the quantity  $a^{(i,j,k;m)}$  in equation (3.9) represents the amplitude of the eddy. Both  $\Delta \mathbf{v}^{(i,j,k;m)}(\mathbf{x})$  and  $\Phi^{(i,j,k;m)}(\mathbf{x})$  are defined in the subdomain

$$\begin{aligned} D^{(i,j,k;m)} = \{(x, y, z)\} = & \left[ \left( i - \frac{3}{2} \right) \ell_{x,m}, \left( i + \frac{1}{2} \right) \ell_{x,m} \right] \times \\ & \times \left[ \left( j - \frac{3}{2} \right) \ell_{y,m}, \left( j + \frac{1}{2} \right) \ell_{y,m} \right] \times \left[ \left( k - \frac{3}{2} \right) \ell_{z,m}, \left( k + \frac{1}{2} \right) \ell_{z,m} \right] \end{aligned} \quad (3.11)$$

and are vanishing outside  $D^{(i,j,k;m)}$ . Thus,  $D^{(i,j,k;m)}$  represents the support of the functions  $\Delta \mathbf{v}^{(i,j,k;m)}$  and  $\Phi^{(i,j,k;m)}$ . Comparing equations (3.3) and (3.11) we see that the sub-domain  $D^{(i,j,k;m)}$  is wider than the corresponding cell  $C^{(i,j,k;m)}$  by a factor 2 along each space direction. Thus, the fields of adjacent cells partially overlap. Indeed, if  $D^{(i,j,k;m)}$  and  $C^{(i,j,k;m)}$  were coincident, the fluctuating field at a given scale would vanish at any surface border of adjacent cells; this would introduce an artificial periodicity at all the scales that would affect statistical homogeneity. Eddy overlapping is implemented in order to avoid this problem. Within a given sub-domain  $D^{(i,j,k;m)}$  a set of linearly rescaled local spatial coordinates are defined by the relations:

$$X^{(i;m)} = X^{(i;m)}(x) = \frac{1}{2\ell_{x,m}} \left[ x - \left( i - \frac{1}{2} \right) \ell_{x,m} \right]$$

$$\begin{aligned}
Y^{(j;m)} &= Y^{(j;m)}(y) = \frac{1}{2\ell_{y,m}} \left[ y - \left( j - \frac{1}{2} \right) \ell_{y,m} \right] \\
Z^{(k;m)} &= Z^{(k;m)}(z) = \frac{1}{2\ell_{z,m}} \left[ z - \left( k - \frac{1}{2} \right) \ell_{z,m} \right]
\end{aligned} \tag{3.12}$$

The origin  $(X^{(i;m)}, Y^{(j;m)}, Z^{(k;m)}) = (0, 0, 0)$  of rescaled coordinates corresponds to the center of the sub-domain  $D^{(i,j,k;m)}$ , while each rescaled coordinate varies in the interval  $[-1/2, 1/2]$  when the point  $(x, y, z)$  varies inside  $D^{(i,j,k;m)}$ . The explicit form of the vector function  $\Phi^{(i,j,k;m)}$  is given in terms of the rescaled coordinates by the following expression

$$\Phi^{(i,j,k;m)}(x, y, z) = \frac{\ell_m}{L_0} F(\xi^{(i,j,k;m)}) F(\eta^{(i,j,k;m)}) F(\zeta^{(i,j,k;m)}) \tag{3.13}$$

where the variables  $\xi^{(i,j,k;m)}$ ,  $\eta^{(i,j,k;m)}$  and  $\zeta^{(i,j,k;m)}$  are defined below [Eqs. (3.14)], and  $F(t)$  is a polynomial function which determines the spatial profile of the eddy. We used the form:

$$\begin{aligned}
F(t) &= 256t^8 - 256t^6 + 96t^4 - 16t^2 + 1 \quad , \quad \text{for} \quad -\frac{1}{2} \leq t \leq \frac{1}{2} \\
F(t) &= 0 \quad \text{elsewhere}
\end{aligned}$$

A plot of the function  $F(t)$  is given in the top panel of Figure 3.1.

The function  $F(t)$  has one single maximum at  $t = 0$  ( $F(0) = 1$ ) and vanishes with its derivatives up to the 4-th order at  $t = \pm 1/2$ . Then, equation (3.13) corresponds a localized eddy which matches with neighboring eddies with continuous derivatives up to the 4-th order. This implies that the turbulent field is continuous with all its derivatives up to the third order; in particular, the vorticity (if we interpret  $\mathbf{v}$  as a velocity field) or the current density (if we interpret  $\mathbf{v}$  as a magnetic field) are continuous with their first derivatives. This feature is different from what done in the models by

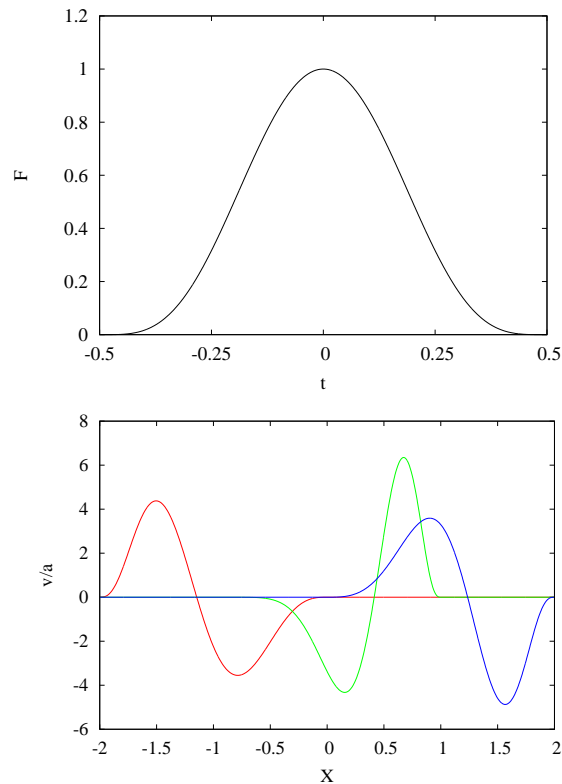


Figure 3.1: Top panel: the profile of the undistorted base function  $F(t)$ . Bottom panel: an example of superposition of neighboring distorted eddies in a given interval along the  $x$  direction.

Juneja *et al.* [61] and Cametti *et al.* [16], in which the profile of the eddy is simpler (a piecewise-linear function), but discontinuities are present in the first derivatives of the turbulent field. The choice of having a more regular field has mainly been done in the perspective of employing the model in test-particle studies; this is useful, for instance, if a term proportional to the current density (the resistive electric field) is included in the motion equation of particles. We also note that  $F(t) \sim 1$ , in the interval  $-1/2 \leq t \leq 1/2$ .

The variables  $\xi$ ,  $\eta$  and  $\zeta$  are related to the rescaled coordinates by the

nonlinear relations:

$$\begin{aligned}
\xi^{(i,j,k;m)} &= X^{(i;m)} + \gamma_x^{(i,j,k;m)} \left( X^{(i;m)^2} - \frac{1}{4} \right) \\
\eta^{(i,j,k;m)} &= Y^{(j;m)} + \gamma_y^{(i,j,k;m)} \left( Y^{(j;m)^2} - \frac{1}{4} \right) \\
\zeta^{(i,j,k;m)} &= Z^{(k;m)} + \gamma_z^{(i,j,k;m)} \left( Z^{(k;m)^2} - \frac{1}{4} \right)
\end{aligned} \tag{3.14}$$

where  $\gamma_x^{(i,j,k;m)}$ ,  $\gamma_y^{(i,j,k;m)}$ ,  $\gamma_z^{(i,j,k;m)}$  are constants which are randomly chosen in the interval  $[-1, 1]$ . The nonlinear mapping (3.14) introduces a distortion in the spatial profile of the eddy along the three spatial directions, whose entity is determined by the three random numbers  $\gamma_x^{(i,j,k;m)}$ ,  $\gamma_y^{(i,j,k;m)}$  and  $\gamma_z^{(i,j,k;m)}$ . This effect has been introduced in order to improve the statistical homogeneity of the fluctuating field. Note that the above regularity properties of the vector potential are preserved by the mapping (3.14). A plot illustrative of the profile of few distorted and overlapped eddies is given in the bottom panel of Figure 3.1.

Finally, using the definitions (3.1), (3.2), (3.12), and (3.14), it can be verified that the form (3.13) of the vector function  $\Phi^{(i,j,k;m)}$  satisfies the assumption (3.10).

### 2.3 Turbulent cascade and intermittency

The amplitudes  $a^{(i,j,k;m)}$  of the eddies are determined considering the phenomenology of the turbulent cascade. In a stationary situation, the mean energy transfer rate  $\langle \epsilon \rangle$  at a given spatial scale  $\ell$  is independent of  $\ell$  (Kolmogorov, 1941 [68]), where spatial brackets indicate a spatial average. For hydrodynamic turbulence  $\langle \epsilon \rangle \sim [\Delta v(\ell)]^3 / \ell$ , implying that the mean fluctuation at the scale  $\ell$  is  $\Delta v(\ell) \propto \ell^{1/3}$ . This scaling law corresponds to the Kolmogorov

spectrum, where the spectral energy density is  $e(k) \propto k^{-5/3}$ , with  $k$  the wave number. In general, we assume that in the inertial range  $\Delta v$  follows the power law given in equation (3.6), corresponding to  $e(k) \propto k^{-(2h+1)}$ . However, it turns out from experimental observation that the energy transfer rate  $\epsilon$  is not spatially uniform, but rather change from place to place according to the effectiveness of nonlinear couplings (Kolmogorov, 1962 [67]). Consequently, the amplitude of fluctuations is not spatially uniform, but fluctuations stronger than the average value  $\langle \Delta v(\ell) \rangle$  form locally, which are separated by regions of weaker fluctuations. This feature propagates to smaller scales through a multiplicative process, becoming more and more relevant with decreasing  $\ell$ . Thus, at small scales the field is characterized by very strong and localized fluctuations with wide “quiet” regions in between: this is the phenomenology of intermittency.

In our model such a process is modeled as in the  $p$ -model by Meneveau & Sreenivasan, 1987 [87], where  $p$  is a fixed parameter chosen in the interval  $[1/2, 1]$ . Energy flows from large to smaller eddies with an unequal rate  $\epsilon$ : each “parent” eddy at a scale  $\ell_m$  gives energy to its eight “daughter” eddies at the scale  $\ell_{m+1}$  with two possible rates; namely,  $\epsilon_{m+1} = 2p\epsilon_m \geq \epsilon_m$  for four daughter eddies and  $\epsilon_{m+1} = 2(1-p)\epsilon_m \leq \epsilon_m$  for the remaining four daughter eddies. For  $p = 1/2$  we have  $\epsilon_{m+1} = \epsilon_m$ , i.e. the rate  $\epsilon$  is equal at all the scales and positions; this corresponds to a non-intermittent fluctuating field. With increasing  $p$  above the value  $1/2$ , differences between the rates increase and the level of intermittency increases, as well. In our synthetic turbulence model  $p$  is a free parameter that we use to investigate the effects of intermittency. More specifically, the transfer rate is recursively determined

for the eddies daughters of the “ $(i, j, k; m)$ ” parent eddy by:

$$\epsilon_{m+1,n} = 2p \epsilon_m \beta_n^{(i,j,k;m)} + 2(1-p) \epsilon_m (1 - \beta_n^{(i,j,k;m)}), \quad (3.15)$$

$$m = 0, \dots, N_s, \quad n = 1, \dots, 8$$

where  $\beta_n^{(i,j,k;m)} = 1$  for four randomly chosen daughters (for instance,  $n = 3, 5, 7, 8$ ) who receive more energy, while  $\beta_n^{(i,j,k;m)} = 0$  for the remaining four daughters ( $n = 1, 2, 4, 6$ ) who receive less energy. The choice of the four daughter eddies which will receive more energy and of those which will receive less energy is made among twelve possible ”heritage patterns”, which are sketched in Figure 3.2.

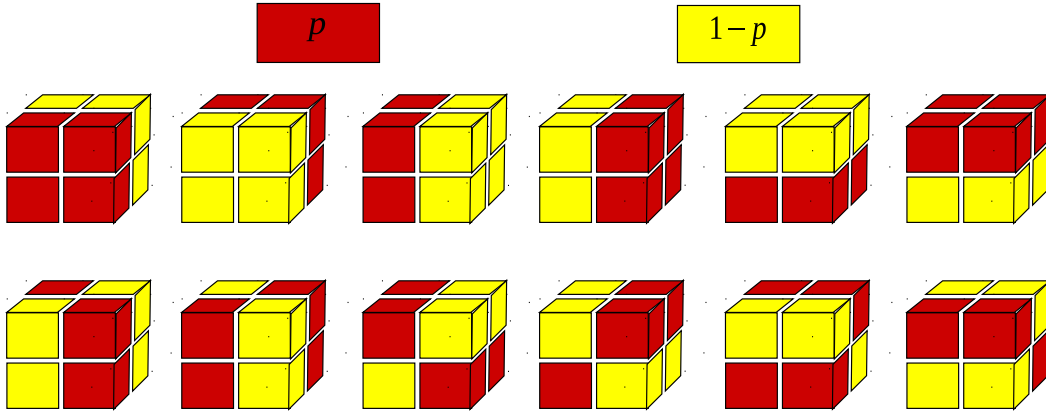


Figure 3.2: A graphic representation of the twelve ”heritage patterns”. In each pattern, cells which receive more (less) energy are represented in red (yellow).

Finally, the amplitude of any eddy is given by

$$a^{(i,j,k;m)} = \sigma^{(i,j,k;m)} a_0 \left[ \frac{\epsilon_m^{(i,j,k;m)} \ell_m}{\epsilon_0 \ell_0} \right]^h \quad (3.16)$$

where  $a_0 = a^{(1,1,1;0)}$  and  $\epsilon_0 = \epsilon^{(1,1,1;0)}$  are the amplitude and the energy transfer rate at the largest scale, respectively, and the exponent  $h$  is related

to the spectral slope. The quantity  $\sigma^{(i,j,k;m)}$  in equation (3.16) represents the sign of the eddy and it is randomly chosen as  $\sigma^{(i,j,k;m)} = 1$  or  $\sigma^{(i,j,k;m)} = -1$ .

In conclusion, the turbulent field is given by

$$\mathbf{v}(\mathbf{x}) = \sum_{m=m_I}^{N_s} \sum_{i,j,k=1}^{2^m} \nabla \times \Psi^{(i,j,k;m)}(\mathbf{x}) = \sum_{m=m_I}^{N_s} \sum_{i,j,k=1}^{2^m} a^{(i,j,k;m)} \nabla \times \Phi^{(i,j,k;m)}(\mathbf{x}) \quad (3.17)$$

where the derivatives in the  $\nabla$  operator are to be calculated with respect to the coordinates  $x$ ,  $y$  and  $z$ , and the index  $m_I$  identifies the injection scale  $\ell_I$ . Using the expressions given in equations (3.12)-(3.14), the analytical form of all the quantities appearing in the equation (3.17) can be explicitly calculated.

## 2.4 Eddy superposition algorithm

Equation (3.17) gives the turbulent field as a superposition of fluctuating fields, each one associated with a particular eddy. As mentioned before, in our model the total number of eddies coincides with the number  $N_{cell}$  of cells, given in equation (3.4). Then, the number of eddies exponentially increases with the number of scales  $N_s$  included in the model; for instance, using  $N_s = 16$  we have  $N_{cell} \simeq 3 \times 10^{14}$ , which is a very large number of eddies. The storage of the whole information defining all the eddies in the computer memory for high values of  $N_{cell}$  would represent a difficulty because of large memory requirements. This is the case for example in the 3D model by Cametti *et al.*, 1998 [16], where the position of each eddy is randomly chosen within the spatial domain; as a result, the memory requirement exponentially increases with  $N_s$  and obliges one to use relatively small values for  $N_s$ , i.e., relatively small spectral widths  $r$ . In fact, the spectral width considered in

the paper (Cametti *et al.*, 1998 [16]) is of the order of two decades. In the present model we use a different algorithm which avoids to use large memory storage power, even for very large values of  $N_{cell}$ . This allows us to reach larger spectral widths  $r$  with a modest computational effort. This aspect is important for having a low-cost synthetic turbulence model, as desirable. In the following we describe how our algorithm is built.

a) In our model eddies are not randomly translated. Thus, the location of the support  $D^{(i,j,k;m)}$  of any eddy is known *a priori* (eq. (3.11)). As a consequence, when calculating  $\mathbf{v}$  at a given spatial point  $\mathbf{x}$ , only a small number of terms give a non-vanishing contribution to the sum of equation (3.17): namely, those terms corresponding to eddies whose support contains the point  $\mathbf{x}$ . Taking into account the partial overlapping of neighboring eddies, it can be verified that, for a given position  $\mathbf{x}$  and for a given value of the scale index  $m$ , only eight eddies satisfy the following condition

$$\mathbf{x} \in D^{(i,j,k;m)} \quad (3.18)$$

and then contribute to build the field  $\mathbf{v}$  at the position  $\mathbf{x}$ . The algorithm first selects these eddies on the base of the position  $\mathbf{x}$ , taking into account the partial overlapping of neighbouring eddies, as well as periodicity in the case eddies are close to the boundaries of the spatial domain. We indicate the eight selected eddies satisfying the condition (3.18) and belonging to the  $m$ -th scale by the indexes  $(\mu;\mathbf{x};m)$ , with  $\mu = 1, \dots, 8$ . Thus, the equation (3.17) is replaced by

$$\mathbf{v}(\mathbf{x}) = \sum_{m=m_I}^{N_s} \sum_{\mu=1}^8 \nabla \times \Psi^{(\mu;\mathbf{x};m)}(\mathbf{x}) \quad (3.19)$$

where  $\Psi^{(\mu;\mathbf{x};m)}$  is the vector potential associated to the eddy whose support

is  $D^{(\mu;\mathbf{x};m)}$ , satisfying the condition (3.18). Equation (3.19) indicates that the number of terms that have to be calculated when evaluating the field at a position  $\mathbf{x}$  is now  $N_{term} = 8 N_s$ , which is much smaller than  $N_{cell}$ . Moreover, while  $N_{cell}$  increases exponentially with the number  $N_s$  of scales,  $N_{term}$  is simply proportional to  $N_s$ . This fact allows for an extremely fast evaluation of the turbulent field, even for large spectral width. For instance, using a number  $N_s = 16$  of scales, corresponding to a spectral width larger than 4 decades ( $r \simeq 1.6 \times 10^4$  with  $m_I = 2$ ), only 128 terms are included in the sum (3.19). Moreover, increasing the number of scales  $N_s$  by a factor 2 would increase the spectral range by a factor  $2^{N_s}$  while the computation time would simply be increased by a factor 2.

b) As explained above, the vector potential  $\Psi^{(i,j,k;m)}$  associated with each eddy is characterized by a set of random parameters, that are: (i)  $\gamma_n^{(i,j,k;m)}$ , defining the distortion of each eddy (equation (3.14)) ; (ii) the sign  $\sigma^{(i,j,k;m)}$  (eq. (3.16)); and (iii)  $\beta_l^{(i,j,k;m)}$  defining the energy transfer rate of each eddy in terms of the rate of its parent eddy (eq. (3.15)), which, in turn, determines the eddy amplitude. In order to calculate the sum in equation (3.19) we have to know all these parameters for the  $N_{term}$  eddies involved in the sum. In principle, this could be done by calculating *a priori* these random quantities for all the eddies and storing this information in the computer memory. Then, when a given eddy is involved in the field evaluation, the corresponding quantities could be recalled and used to calculate the field. However, the total number of eddies  $N_{cell}$  can be very large; for instance, using a number of scales  $N_s = 16$ , we have  $N_{cell} \simeq 3 \times 10^{14}$  (eq. 3.4). In that case, storing the information defining all the eddies would require a huge amount of memory.

For that reason, we used a different procedure, which is described in the following. Since the eddies involved in the sum of eq. (3.19) have been selected only on the base of their location with respect to the position  $\mathbf{x}$  (condition eq. (3.18)), their defining parameters must depend only on the location of the eddies within the lattice of cells. Such parameters are determined in the following way: for any given cell, an integer  $\lambda^{(i,j,k;m)}$  is calculated using the expression

$$\lambda^{(i,j,k;m)} = i + (j - 1)2^m + (k - 1)2^{2m} + \nu_m \quad (3.20)$$

where the integer  $\nu_m$  is defined as follows:

$$\nu_m = \begin{cases} 0 & \text{if } m = 0; \\ \sum_{n=0}^{m-1} 2^{3n} & \text{if } m \geq 1. \end{cases} \quad (3.21)$$

It can be verified that, for  $m$  varying between 0 and  $N_s$  and for  $i$ ,  $j$  and  $k$  varying between 1 and  $2^m$ , the expression (3.20) generates all the integers between 1 and  $N_{cell}$ . This defines a one-to-one correspondence between the set  $\{1 \leq \lambda \leq N_{cell}, \lambda \text{ integer}\}$  and the set of cells. In other words,  $\lambda^{(i,j,k;m)}$  represent an absolute address for any cell. The integer  $\lambda^{(i,j,k;m)}$  is used as a seed for a random number generating routine (RNGR), which is called a fixed number  $i_{sample}$  of times, with  $i_{sample}$  an integer. Finally, the resulting number calculated by the RNGR is used to generate the parameters  $\gamma_n^{(i,j,k;m)}$ ,  $\sigma^{(i,j,k;m)}$ , and  $\beta_l^{(i,j,k;m)}$ , which define the eddy associated with the given cell. In this way, the properties of the  $N_{term}$  eddies appearing in the sum (3.19) are univocally determined as functions of the given position  $\mathbf{x}$ . This completely defines all the quantities in eq. (3.19) and allows for an explicit evaluation of

the field  $\mathbf{v}$  at any spatial position  $\mathbf{x}$ . Moreover, different choices of the integer  $i_{sample}$  lead to different realizations of the turbulent field. This allows us to build an ensemble of configurations for the turbulent field. Strictly speaking, the parameters  $\gamma_n^{(i,j,k;m)}$ ,  $\sigma^{(i,j,k;m)}$  and  $\beta_l^{(i,j,k;m)}$  are not random quantities because they are univocally determined as soon as the position  $\mathbf{x}$  has been chosen. On the other hand, the set of possible values of the seed  $\lambda^{(i,j,k;m)}$  is formed by  $N_{cell}$  of values, which is an extremely large value (eq. (3.4)). This fact, in practice, ensures a global randomness of the parameters which define the structure of single eddies. We note that in the above-described algorithm nothing needs to be kept in memory: each time the field  $\mathbf{v}$  is to be calculated at a position  $\mathbf{x}$ , this is done deducing all the properties of the  $N_{term}$  involved eddies directly from their absolute address  $\lambda^{(i,j,k;m)}$ . Finally, at variance with other methods, no spatial grid is used; on the contrary the field is directly calculated at the given spatial point without any interpolation procedure.

## 2.5 Anisotropic spectrum

In many examples of real-world flows, the turbulence spectrum is not isotropic in the wave-vector space. For instance, this happens in MHD when a large-scale magnetic field  $\mathbf{B}_0$  is present. In this case,  $\mathbf{B}_0$  introduces a preferential direction and the energy cascade tends to preferentially develop in the directions perpendicular to  $\mathbf{B}_0$ . This generates anisotropic spectra both for the velocity and for the magnetic field perturbations, in which perpendicular wave-vectors prevail over parallel ones. This has been shown in theoretical studies (e.g., Shebalin *et al.*, 1983 [115], Carbone and Veltri, 1990 [17], Oughton *et al.*, 1994 [93]). Moreover, observations indicate that in the so-

lar wind turbulence spectrum the distribution of wave-vectors of magnetic fluctuations has a significant population quasi-perpendicular to the mean magnetic field (Matthaeus *et al.*, 1986 [82], 1990 [83]).

Within that context, Goldreich & Sridhar, 1995 [51] introduced the principle of “critical balance”. In that formulation it is assumed that the non-linear time for an eddy with sizes  $\ell_{\parallel}$  and  $\ell_{\perp}$  (parallel and perpendicular to  $\mathbf{B}_0$ , respectively) depends only on the transverse size  $\ell_{\perp}$ :  $\tau_{nl} = \ell_{\perp}/\Delta a(\ell_{\perp})$ ,  $\Delta a(\ell_{\perp}) \propto \ell_{\perp}^{1/3}$  being the velocity/magnetic field fluctuation amplitude which is assumed to follow the Kolmogorov scaling law. Moreover, all along the spectrum a balance is assumed to hold between  $\tau_{nl}$  and the propagation time  $t_A = \ell_{\parallel}/c_A$ , which is the time a perturbation takes to travel over a distance  $\ell_{\parallel}$  along  $\mathbf{B}_0$  at the Alfvén velocity  $c_A$ . This gives a relationship between parallel and perpendicular lengths of eddies:

$$\ell_{\parallel} \propto \ell_{\perp}^{2/3} \tag{3.22}$$

equation (3.22) indicates that, when going from large to small scales,  $\ell_{\parallel}$  decreases slower than  $\ell_{\perp}$ , i.e., structures more and more elongated in the  $\mathbf{B}_0$  direction are found at small scales. This corresponds to a spectrum which is more anisotropic at small scales than at large scales. We explored the possibility to reproduce the anisotropy corresponding to the critical balance principle by our synthetic turbulence model. This has been done by modifying the above-described cell hierarchy in the following way. First,  $z$  has been conventionally chosen as the direction parallel to the background magnetic field  $\mathbf{B}_0$ . Second, we introduce the possibility to have anisotropic cell divisions; this means that, when going from the  $m$ -th scale to the  $(m + 1)$ -

th scale, all the cells at the  $m$ -th scale are divided only along the  $x$  and  $y$  directions, while no division is performed in the  $z$  direction. In other words, the aspect ratio of cells at the  $m$ -th scale is different from that of cells at the  $(m + 1)$ -th scale, the latter being more elongated along  $z$  than the former. In contrast, in the previously-described isotropic cell division, when going from the  $m$ -th to the  $(m + 1)$ -th scale, the cells are equally divided along all the three spatial directions, keeping the same aspect ratio at all the scales. These two possibilities are described by the equations:

$$\ell_{x,m+1} = \ell_{x,m}/2 \quad , \quad \ell_{y,m+1} = \ell_{y,m}/2 \quad , \quad \ell_{z,m+1} = \ell_{z,m}/\rho_m \quad (3.23)$$

where  $\rho_m = 2$  in the case of isotropic division, while  $\rho_m = 1$  in the case of anisotropic division. The relation (3.22) between parallel and perpendicular lengths can be reproduced by a suitable choice of the coefficients  $\rho_m$  in equation (3.23), given by the following sequence:

$$\{\rho_m, m = 0, \dots, N_s\} = \{2, 2, 1, 2, 2, 1, 2, 2, 1, \dots\} \quad (3.24)$$

corresponding to one anisotropic division every three divisions.

In the anisotropic version of the model, some definitions used in the previously-described isotropic case must be modified accordingly. The  $m$ -th scale in the  $z$  direction (equation (3.1)) is now defined as  $\ell_{z,m} = L_z/\pi_m$ , where

$$\pi_m = \prod_{i=0}^m \rho_i \quad (3.25)$$

The index  $k$ , which identifies the cell position in the  $z$  direction within the lattice (see, e.g., equation (3.3)), now varies in the interval  $k = 1, \dots, \pi_m$ . Since the smallest size of an eddy is now  $\ell_{\perp,m} = \ell_{x,m} = \ell_{y,m} \leq \ell_{z,m}$  we now

adopt the following expression for the vector function  $\Phi^{(i,j,k;m)}$  (compare with equation (3.13)):

$$\Phi^{(i,j,k;m)}(x, y, z) = \frac{\ell_{\perp,m}}{L_0} F(\xi^{(i,j,k;m)}) F(\eta^{(i,j,k;m)}) F(\zeta^{(i,j,k;m)}) \quad (3.26)$$

Finally, since in the critical balance principle the spectrum is assumed to follow a Kolmogorov law with respect to  $k_{\perp}$ , the equation (3.16) defining the eddy amplitude is now replaced by

$$a^{(i,j,k;m)} = \sigma^{(i,j,k;m)} a_0 \left[ \frac{\epsilon_m^{(i,j,k;m)} \ell_{\perp,m}}{\epsilon_0 \ell_0} \right]^{1/3} \quad (3.27)$$

All the other features of the model and of the algorithm remain unchanged. It is worth mentioning that the model can be adapted to reproduce other anisotropy types, such as the ones generated in shear, rotating, or wall-bounded flows. Such flexibility makes the model suitable to describe diverse physical systems.

### 3 Testing the model

In order to test the model, the standard diagnostics for the description of intermittent turbulence have been routinely performed on the synthetic data. A number of realizations of the synthetic turbulent field  $\mathbf{v}(\mathbf{x})$  have been generated both for the isotropic and for the anisotropic version of the model. For each run, one single sample was generated with  $i_{sample} = 1$ . The typical Kolmogorov scaling exponent  $h = 1/3$  was imposed for all runs, while the strength of the intermittency was changed by allowing the parameter  $p$  to take the following values:  $p = 0.5$ , corresponding to non-intermittent turbulence;  $p = 0.7$ , a realistic value close to the typical observations in ordinary fluid

turbulence;  $p = 0.9$ , representing a “super-intermittent” case, which will be mostly used as benchmark for the parametric description of the model. The relevant scales were imposed (the integral scale  $\ell_I = L_0/4$ ) or estimated by looking at the spectra (the dissipation scale  $\ell_d \simeq L_0/(2 \times 10^4)$ , see Figure 3.6), resulting in the effective Reynolds number  $Re \sim (\ell_I/\ell_d)^{4/3} \simeq 8.5 \times 10^4$ , which is smaller but close to the estimation given in the eq. (3.8). From each run, synthetic trajectories of length  $L = 40\ell_I$  were extracted as one-dimensional samples, with spatial resolution  $dr \simeq 1.5 \times 10^{-5}\ell_I$  chosen as to ensure the inclusion of the whole inertial range in the spectrum. For each trajectory, the longitudinal field increments  $\Delta v$  were computed at different scales  $l$ ,  $\langle v \rangle$  and  $\sigma_v$  being respectively their mean and standard deviation. Since from now on we will only consider the component of the field along the virtual trajectory, we will simplify the notation by defining  $v(s) \equiv \mathbf{v}(\mathbf{x}) \cdot \hat{\mathbf{s}}$ , where  $\hat{\mathbf{s}}$  is the unit versor of the trajectory. For each realization of the turbulent field, the following quantities have been obtained: (1) the autocorrelation function  $A_c(l) = \langle [v(s) - \langle v \rangle][v(s+l) - \langle v \rangle] \rangle / \sigma_v^2$ , which gives useful information about the correlation scale of the field,  $l_c$ ; (2) the associated energy power spectrum  $E(k)$  ( $k = 2\pi/l$  being the wave-vector associated with the scale  $l$ ), whose power-law scaling exponent has to be compared with the one imposed for the model field fluctuations,  $h$ ; (3) the Probability Distribution Functions (PDFs) of the scale-dependent increments,  $P(\Delta v)$ , whose deviation from Gaussian will qualitatively illustrate the presence of intermittency; (4) the structure functions  $S_q(l) = \langle |\Delta v|^q \rangle \sim l^{\zeta_q}$ , i.e. the scale-dependent  $q$ -th order moments of the field increment distribution, and their anomalous scaling exponents  $\zeta_q$ ; (5) the kurtosis  $K = S_4/S_2^2$ , an alternative, quantita-

tive measure of intermittency (fully determined by the scaling of the structure functions), along with its scaling exponent  $\kappa$ ; (6) and, finally, a box-counting based multifractal analysis, providing some finer detail on the geometrical properties of the flow.

It should be noticed that the present version of our model does not include the skewness of the PDFs, a crucial ingredient of intermittency universally observed in real turbulence (Frisch, 1995 [48]). For this reason, it will be necessary to use the absolute value of the fluctuations to prevent the odd-order structure functions to vanish.

### 3.1 Isotropic turbulence

Examples of the field longitudinal component  $v(s)$ , extracted from one of the realizations of isotropic turbulence, is shown in the top panels of Figure 3.3 for two values of the intermittency parameter  $p$ . Along with the longitudinal field component, the increments  $\Delta v$  at two different scales  $l$  are included in the figure. The presence of intermittency is revealed by the scale-dependent general properties of the increments, and in particular by their increasing burstiness towards smaller scales.

#### Two-dimensional Spectrum.

For the isotropic runs, a preliminary study of the full spectral properties of the fields revealed the presence of a weak residual anisotropy, probably due to the shape of the generating functions. Indeed, the two-dimensional cut of the spectrum presented in Figure 3.4 displays an excess of power along the diagonals, which results in roughly squared rather than circular isocontours.

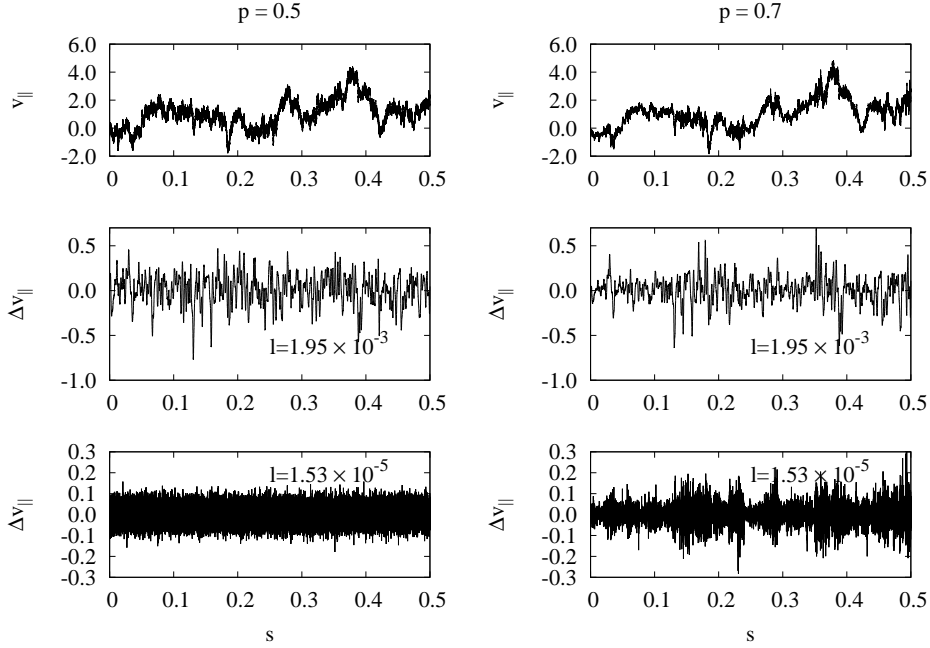


Figure 3.3: Examples of profile of the longitudinal component of the field  $v$ , together with the increments  $\Delta v$  evaluated at two different scales (see legend). Left panels: no intermittency ( $p = 0.5$ ); right panels: standard intermittency ( $p = 0.7$ ).

This feature is consistently observed in all of the three two-dimensional spectral cuts (not shown). In order to mitigate this weak deviation from isotropy, and to increase the statistical significance of the sample, for each realization ten different trajectories were selected at varying angles with the domain axes, so that the solid angle was homogeneously sampled. Each sample was analyzed separately using the tools described above. The results were finally averaged over the ten different samples from all the trajectories. The corresponding standard deviation was used as an estimate of the uncertainty in the model parameters.

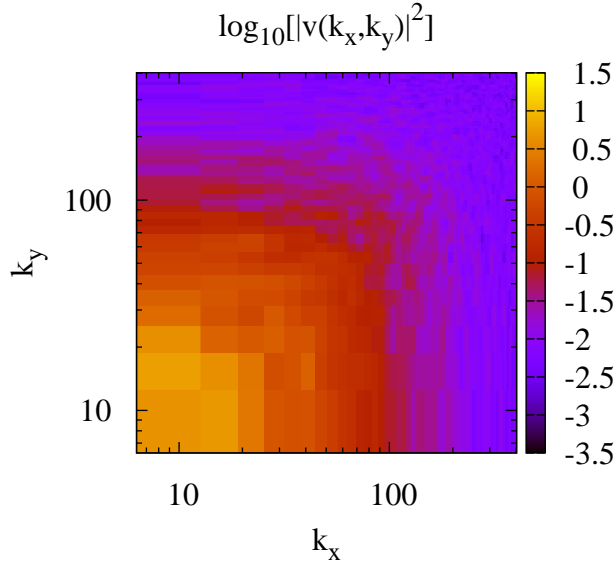


Figure 3.4: Isocontours of the two-dimensional spectrum in the plane  $k_x, k_y$  for the total power associated to the intermittent field  $\mathbf{v}$ . The image refers to the case  $p = 0.7$ . Similar results hold for the other levels of intermittency (not shown).

### Autocorrelation Function.

Figure 3.5 shows examples of the autocorrelation function versus the separation scale  $l$ , for different values of the intermittency parameter  $p$ .

The autocorrelation functions display the typical behaviour for turbulent fields, with a parabolic decay near the origin (not shown). A faster, quasi-exponential decay follows toward large separation, where eventually the small-amplitude fluctuations around zero determine the noise level. As customary, an estimate of the correlation scale can be obtained as the scale at which the autocorrelation function reaches the uncorrelated-scale noise level.

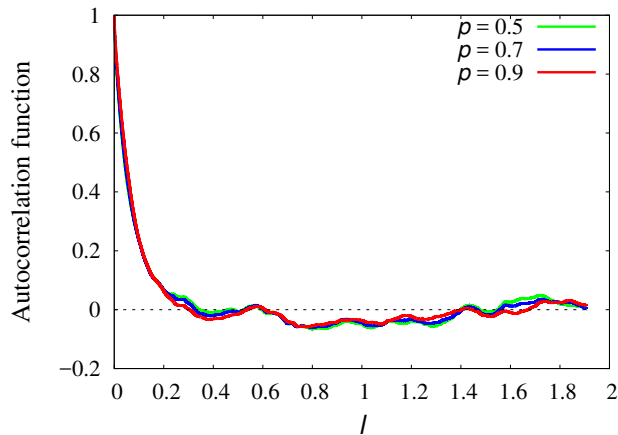


Figure 3.5: The autocorrelation function for the longitudinal field component, for the three values of the intermittency parameter  $p$ .

The values obtained for the three cases are collected in Table 3.1, and are consistent with the imposed integral scale  $\ell_I = L_0/4$ . There is no relevant difference between the three runs, as intermittent corrections to the autocorrelation function are expected to be small.

### **Omnidirectional spectrum.**

For all runs, the energy power spectra evaluated along each trajectory and then averaged, provide quick information about the scaling properties of the fluctuations, and are given in Figure 3.6, along with power-law fits in the inertial range.

At small scale, a quasi-exponential decay indicates the smoothness of the field, due to the differentiability of the mother functions, and mimicking the dissipation scale of turbulence. On the contrary, at very large scales the absence of correlation weakly flattens the spectrum. The spectral indexes obtained from the power-law fit within the inertial range are listed in Table 3.1.

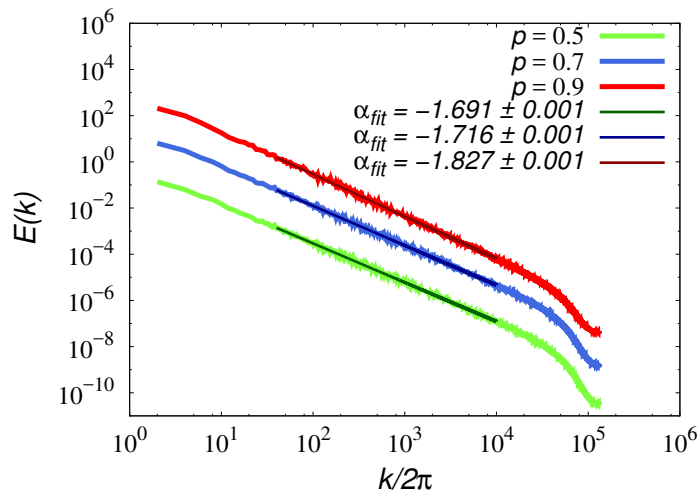


Figure 3.6: The one-dimensional power spectra  $E(k)$  for the longitudinal component of the synthetic field, for the three runs. Power-law fits are also superposed. The scaling exponents are collected in Table 3.1, showing good agreement with the imposed Kolmogorov-like spectrum.

For all runs, the exponents are slightly larger than the values expected using the simple relation  $\alpha = 2h + 1$ , with the input parameter  $h = 1/3$ . This is evident for the case  $p = 0.5$ , for which  $\alpha = 1.69$  instead of  $5/3$ . Such weak discrepancy is consistently observed for the other two runs with  $p \neq 0.5$ , when considering the intermittent correction.

### Probability Distribution Functions of longitudinal increments.

In order to account for inhomogeneities of the energy flux in the cascade process, i.e. of intermittency, examples of the increment PDFs at different scales are collected in Figure 3.7 for three values of  $p$ .

The increments have been previously standardized for each scale, in order to allow a proper comparison. It is evident that in the absence of intermittency ( $p = 0.5$ ) the distribution functions are roughly Gaussian, and almost iden-

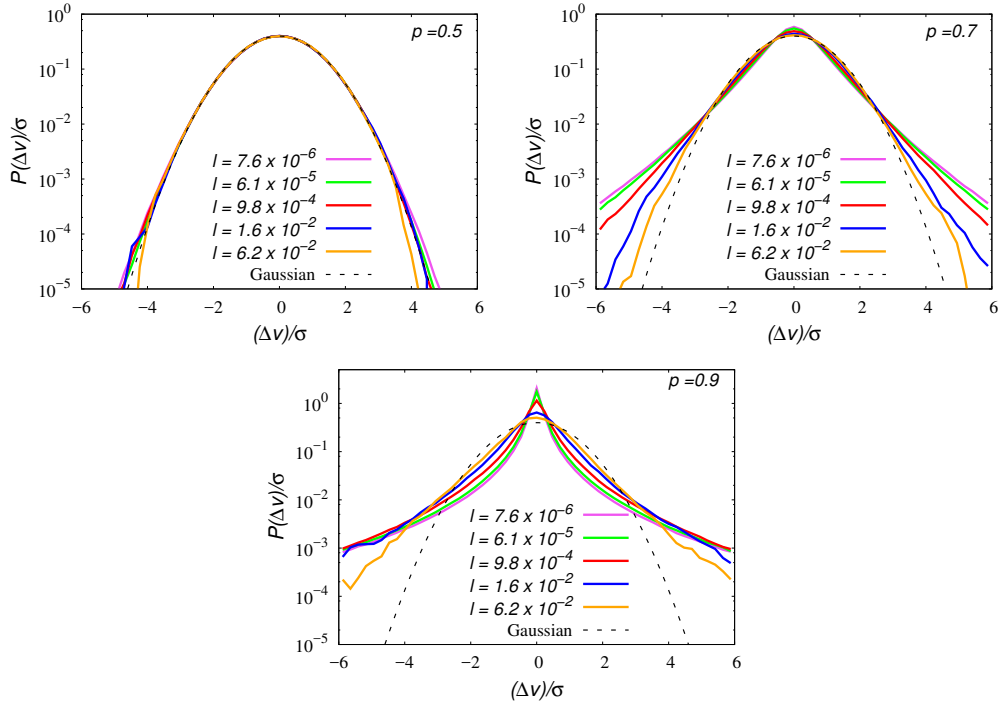


Figure 3.7: Probability Distribution Functions of the standardized field increments on different scales (see legend) for the three runs. Top panel:  $p = 0.5$ ; central panel:  $p = 0.7$ ; bottom panel:  $p = 0.9$ .

tical at all scales. This indicates self-similarity of the fluctuations and is the result of an homogeneous redistribution of the energy along the cascade. For "realistic" values of the intermittent parameter ( $p = 0.7$ ), the typical increase of the distribution tails toward small scales is observed (Frisch, 1995 [48]). This captures the increasing localization of energy as the scale decreases, spontaneously arising in turbulent flows and well reproduced by the model. The "super-intermittent" case ( $p = 0.9$ ) shows even more evident high tails of the distributions.

### Structure Functions.

An alternative description of the intermittency is obtained by means of the anomalous scaling of the structure functions  $S_q(l)$ . Examples are shown in the top panel of Figure 3.8 for the realistic intermittency case  $p = 0.7$ , for orders up to  $q = 6$  (convergence of the moments has been tested following Dudok de Wit, 2004 [32], and Dudok de Wit *et al.*, 2013 [31]). In the intermediate range of scales, roughly corresponding to the spectral inertial range, the structure functions have been fitted to power laws. The resulting scaling exponents are collected in the bottom panel of Figure 3.8 for the three different values of the parameter  $p$ . Their deviation from the linear prediction  $\zeta_q \sim hq$  identifies the effects of intermittency. For a more quantitative estimate, the scaling exponents have been fitted to a  $p$ -model [87], whose prescription gives

$$\zeta_q = 1 - \log_2 \left[ p^{hq} + (1 - p)^{hq} \right]. \quad (3.28)$$

The fitting curves are indicated in the figure as lines, showing good agreement with the data. The corresponding empirical intermittency parameters  $p_{fit}$  are collected in Table 3.1, and are consistent with the prescribed values. This confirms that the model is able to effectively generate the desired degree of intermittency in the data by adjusting the parameter  $p$ .

### Kurtosis.

Figure 3.9 shows the scaling behavior of the kurtosis  $K(l)$  for the three values of  $p$ . The non-intermittent run gives the constant value  $K = 3$  at all scales, as expected for a Gaussian variable. When intermittency is included, the kurtosis is Gaussian at large scales, roughly down to the correlation scale,

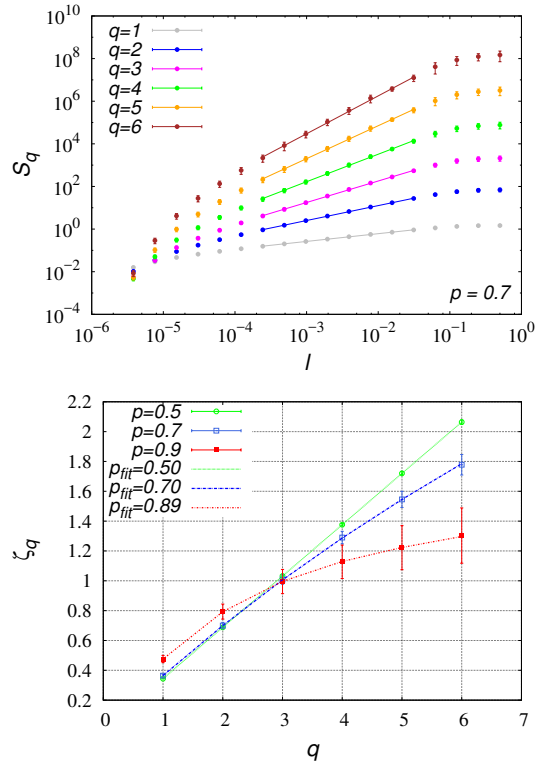


Figure 3.8: Top panel: the structure functions for the longitudinal component of the field for the case  $p = 0.7$ . Power-law fits used to evaluate the scaling exponents  $\zeta_q$  are superimposed. Bottom panel: The anomalous scaling of the structure functions, highlighted by the nonlinear order dependency of the scaling exponents  $\zeta_q$ , for three values of  $p$ . Fits with the  $p$ -model, equation (3.28), are indicated as lines. The agreement of the data with the model is excellent.

and increases toward small scales as a power law  $K(l) \sim l^{-\kappa}$ .

In Navier-Stokes turbulence, it is often observed that  $\kappa \simeq 0.1$  (also described by the  $p$ -model and by the She-L ev eque model), which is consistent with the value obtained by fitting the case  $p = 0.7$ . As expected, saturation of the kurtosis is evident for scales smaller than the dissipative scale  $\ell_d$ . Furthermore, note that the largest kurtosis attained by the model in the realistic intermittency case ( $k_{max} \simeq 10$ ) is compatible with the values normally found

Table 3.1: For the three isotropic runs with different intermittency levels  $p$ , we show here: the correlation length  $l_c$ , as estimated from the autocorrelation function; the spectral index  $\alpha$ , as obtained fitting the spectrum with a power-law; the empirical value of the parameter  $p_{fit}$ , as obtained from a  $p$ -model fit of the structure functions scaling exponents; and the scaling exponent of the kurtosis  $\kappa$ , as estimated through a power-law fit. For the case  $p = 0.5$ , the value  $\kappa = 0$  was assumed without fitting the kurtosis.

$p$	$l_c$	$\alpha$	$p_{fit}$	$\kappa$
0.5	$0.21 \pm 0.07$	$1.691 \pm 0.005$	$0.5 \pm 0.1$	0
0.7	$0.21 \pm 0.06$	$1.716 \pm 0.001$	$0.71 \pm 0.02$	$0.101 \pm 0.006$
0.9	$0.20 \pm 0.04$	$1.827 \pm 0.001$	$0.89 \pm 0.02$	$0.42 \pm 0.03$

in many experimental observations with a comparable inertial range extension (or Reynolds number). For the case with  $p = 0.9$ , the scaling exponent of the kurtosis is larger, consistent with a more efficient intermittency. All the diagnostics described above shows that the synthetic data are consistent with the prescribed values of power spectral decay and intermittency. This demonstrates that the data are representative of a real-world, tunable turbulence, and can therefore be used for numerical studies.

### 3.2 Multifractal Analysis.

A different way of characterizing the intermittent behavior is the determination of the multifractal properties of the signal under study, in particular of generalized multifractal dimensions and the singularity spectrum associated with an appropriate measure (Paladin and Vulpiani, 1987 [94]). The multifractal formalism (Frisch and Parisi, 1983 [47], Halsey *et al.*, 1986 [53]) was originally introduced in the context of fully developed turbulence and

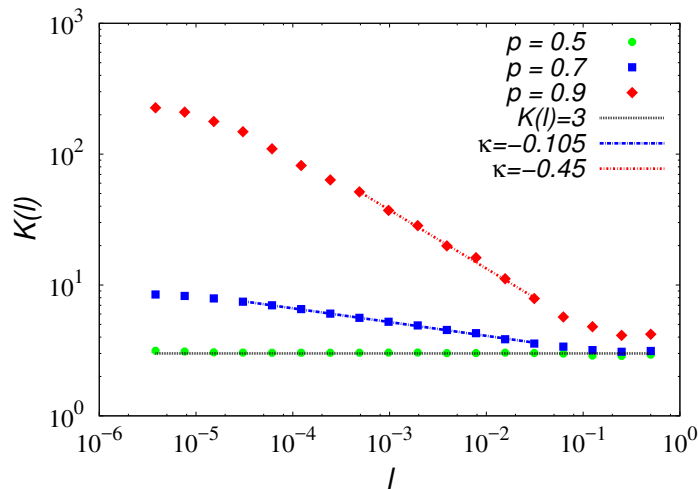


Figure 3.9: The scaling dependence of the kurtosis  $K$ , for the three values of the intermittency parameter. The Gaussian value  $K = 3$  is indicated, as well as a power-law fit in the inertial range for the two intermittent cases.

chaotic systems (Mandelbrot, 1977 [77]), but since then it has become a standard tool to analyze phenomena observed in disordered system (Paladin and Vulpiani, 1987 [94]). Multifractal analysis is able to capture the spatial inhomogeneities of the turbulent energy cascade, so that *global* scale-invariance and self-similarity are usually associated with monofractal measures, while *local* scale-invariance, or local self-similarity, is associated a to multifractals. For the analysis of our model fields, a suitable choice of an associated scalar quantity is the squared derivative along the trajectory  $\partial_s$  of the velocity field component  $v(s)$ , estimated as the longitudinal velocity increment at the resolution scale,  $\partial_s v(s)^2 = \Delta v(s, dr)^2$ . To investigate the multifractal structure of this signal we use the standard box-counting method (Vio *et al.*, 1992 [133], Halsey *et al.*, 1986 [53]). Given the scalar signal  $\Delta v(s)^2$ , the generalized

box-counting partition function of order  $q$  is defined as

$$\chi_q(l) = \sum_{i=1}^{N(l)} \mu_i(l)^q , \quad (3.29)$$

where  $N(l)$  is the minimum number of one-dimensional segments  $Q_i(l)$  of length  $l$  necessary to cover the trajectory  $L$ , and  $\mu_i(l)$  is a suitably defined scale-dependent measure on the line:

$$\mu_i(l) = \frac{\sum_{s \in Q_i(l)} \Delta v(s)^2}{\sum_{s \in L} \Delta v(s)^2} \quad (3.30)$$

High values of  $q$  in the partition function  $\chi_q$  enhance the strongest singularities, say the most intense values of the signal under analysis, while small values of  $q$  represent the regular regions. Conversely, negative values of  $q$  emphasizes regions where the measure  $\mu_i(l)$  is smaller, or the “voids” in the signal. The generalized dimensions  $D_q$  are then formally defined by:

$$D_q = \frac{1}{q-1} \lim_{l \rightarrow 0} \frac{\log \chi_q(l)}{\log l} \quad (3.31)$$

The definition given in equation (3.31) implies a scaling behavior of the partition function  $\chi_q(l)$  for small  $l$ :

$$\chi_q(l) \sim l^{\tau_q} , \quad \text{where } \tau_q = (q-1)D_q \quad (3.32)$$

and  $\tau_q$  is the  $q$ -order “mass” exponent (also called Rényi scaling exponent) of the generalized partition function. The box-counting method consists of calculating the partition functions  $\chi_q$ , then derive  $\tau_q$  from the power-law fit of  $\chi_q$ , obtain the generalized dimensions  $D_q$  through equation (3.32), and then the multifractal spectrum  $f(\alpha)$  through a Legendre transform, given by:

$$f(\alpha) = q\alpha - \tau_q ,$$

$$\alpha = \frac{d\tau_q}{dq} .$$

The latter basically gives the distribution of fractal dimensions of the subsets where the field has a given singularity strength (Chhabra *et al.*, 1989 [23], Paladin and Vulpiani, 1987 [94]). Multifractal systems display nonlinear order dependence of the scaling exponents  $\tau_q$ , which implies non single-valued dimensions  $D_q$ , and which result in a broad multifractal spectrum  $f(\alpha)$  (Chhabra *et al.*, 1989 [23], Paladin and Vulpiani, 1987 [94]). In order to test the multifractality of our model as a signature of intermittency, we thus compute the partition functions  $\chi_q(l)$  by varying the value of the exponent  $q \in [-9, 9]$  with step  $dq = 0.2$ , for each of the ten trajectories considered in the domain of the system, and for the three isotropic runs with  $p = 0.5, 0.7, 0.9$ . For each run, we then compute the average partition functions over the ten trajectories, as already done for the other statistical quantities, and we derive  $\tau_q$  by fitting the functions  $\chi_q(l)$  to power laws. Partition functions and the relative power-law fits are shown in Figure 3.10 for the run with  $p = 0.7$ .

The behavior of  $\tau_q$  as function of  $q$  is the result of this procedure, and is depicted in Figure 3.11 (left panel). The linear dependence observed for the run with  $p = 0.5$  indicates fractal characteristics, while the degree of multifractality increases for larger  $p$ . This is also evident by looking at the generalized dimension  $D_q$ , shown in the right panel of Figure 3.11, which is constant for  $p = 0.5$  and increasingly broadens for larger  $p$ . The same behaviour is observed in the multifractal spectrum  $f(\alpha)$ , shown in the bottom panel of

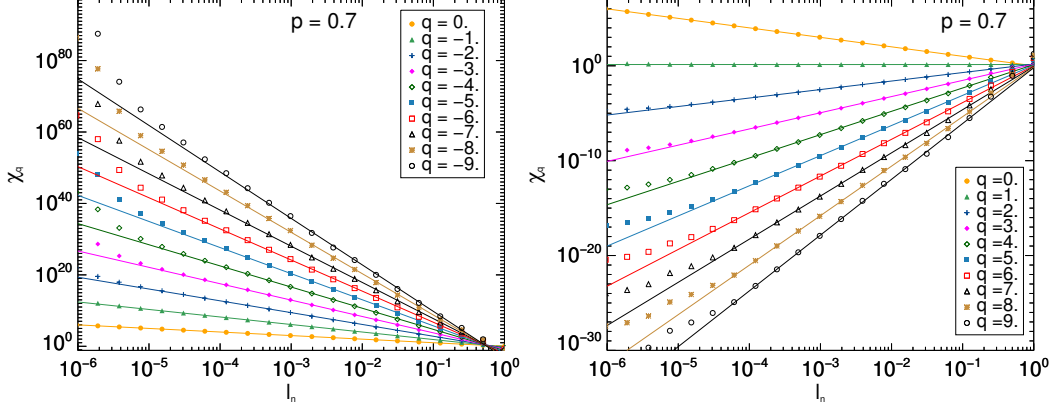


Figure 3.10: The partition functions  $\chi_q$  ( $q < 0$  left panel,  $q > 0$  right panel) for the case  $p = 0.7$ . Power law fits (solid lines) are performed in a wide range of scales, roughly corresponding to the spectral inertial range.

Figure 3.11. In the non-intermittent case, the spectrum is single-valued, indicating that one single singularity exponent characterizes the whole space. As the model parameter  $p$  is increased to induce intermittency, the spectrum becomes evidently broader, indicating a greater variety of the singularity exponents, or inhomogeneity of the cascade. Finally, in order to have a more quantitative estimate of multifractal properties of the field, we fit the scaling exponents  $\tau_q$  with the  $p$ -model prescription  $\tau_q = -\log_2[p^q + (1-p)^q]$  (Meneveau and Sreenivasan, 1987 [87]). We then compare the values obtained from the fit,  $p_{fit}$ , with the prescribed intermittency parameter  $p$ , as already done for the structure functions analysis. The fits and the values of  $p_{fit}$  are indicated in the three panels of Figure 3.11.

The graphics show a good qualitative agreement, i.e. multifractality grows as the imposed intermittency increases.

However, the quantitative comparison between  $p$  and  $p_{fit}$  shows some

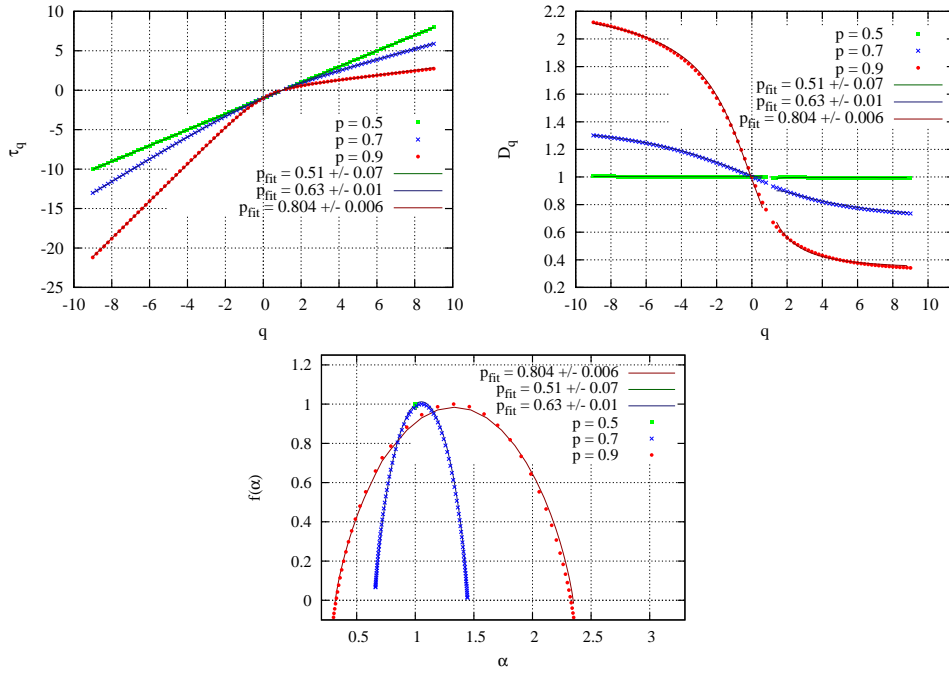


Figure 3.11: The multifractality highlighted by the shape of Rényi scaling exponent  $\tau_q$  vs  $q$  (top-left panel), the generalized dimension  $D_q$  (top-right panel), and the multifractal spectrum  $f(\alpha)$ . The case with  $p = 0.5$  is a monofractal, while the case with  $p = 0.7$  displays a multifractal degree smaller than for  $p = 0.9$ . In the plots, solid lines represent the  $p$ -model fits performed on the scaling exponents  $\tau_q$  and then transformed into the other quantities. The values of the fitting parameter  $p_{fit}$  are indicated.

discrepancy, the fitted values being somewhat smaller than the imposed ones for the two intermittent runs. This could be due to the model limitations in capturing the finer geometrical properties of the intermittent structures. The specific choice of the field used for the analysis in this paper could also have an effect on the measure. Different such choices have been tested giving similar results, but a more detailed study is deferred to a future work. Nevertheless, the overall response of the model to multifractal analysis is satisfactory, at least qualitatively.

### 3.3 Anisotropic turbulence

When anisotropy is introduced in the model, it is necessary to test the intermittency as a function of the virtual trajectory direction. Since the imposed anisotropy is gyrotropic, it is sufficient to study the angular variation with respect to the anisotropy axis (in the present case along the  $z$  axis), corresponding for example to the mean magnetic field direction in a MHD turbulence. The imposed symmetry also allows us to use one quadrant only, so that ten trajectories have been selected to scan the non-gyrotropic angle  $0^\circ < \theta < 90^\circ$ . Each of these trajectories has been divided in ten subsets of size  $L \gg \ell_I$ , and the results of the different diagnostic tools have been averaged for each angle. Again, their standard deviation represents the statistical uncertainty. The analysis has been performed on the non-intermittent case, i.e.  $p = 0.5$ , and on the intermittent case with  $p = 0.7$ .

#### **Spectral analysis.**

The two-dimensional spectrum for the  $p = 0.7$  run is shown in Figure 3.12, where the anisotropic distribution of power is evident.

Figure 3.13 shows the power spectra for different angles  $\theta$  between  $15^\circ$  and  $75^\circ$ , for the intermittent case  $p = 0.7$  (top panel).

The fitted power-law index as a function of the angle  $\theta$  is shown in the bottom panel of the same figure, both for the intermittent and for non-intermittent runs. As can be seen, the spectral index is reasonably constant for intermediate angles  $15^\circ < \theta < 60^\circ$ , and roughly coincides with the prescribed Kolmogorov value  $\alpha \simeq 5/3$ . For quasi-perpendicular trajectories with  $\theta > 80^\circ$ , the spectral index increases, and reaches values as large as  $\alpha = 2.1$ .

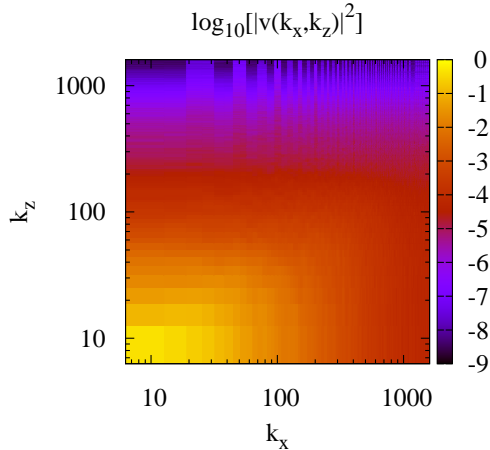


Figure 3.12: Isocontours of the two-dimensional spectrum in the plane  $k_x, k_y$  for the total power associated to the intermittent field  $v$  in the anisotropic case. The image refers to the case  $p = 0.7$ .

This behavior is qualitatively consistent with the prediction of critically balanced turbulence (Goldreich and Sridhar, 1995 [51]) and with some observations in numerical simulation and in solar wind measurements (Horbury *et al.*, 2008 [60], Chen *et al.*, 2011 [20]).

### Structure Functions.

In order to evaluate the effects of anisotropy on intermittency, in Figure 3.14 we show the structure functions scaling exponents  $\zeta_q$  for five different values of the angle  $\theta$ , for the two runs with and without intermittency (top and central panel). As for the isotropic case, the fit of the scaling exponents with the  $p$ -model provides a quantitative estimate of intermittency through the parameter  $p$ , which is plotted in the bottom panel of Figure 3.14 as a function of the angle  $\theta$ , for the intermittent run considered (the non-intermittent

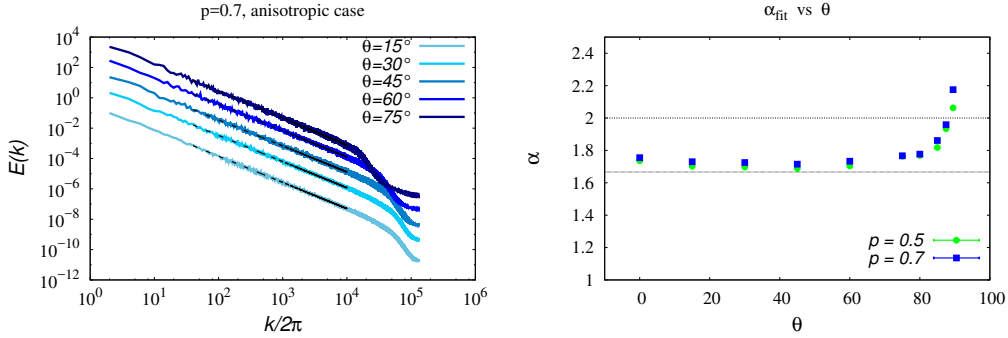


Figure 3.13: Top panel: the one-dimensional power spectrum  $E(k)$  of the virtual trajectories within the synthetic field, shown here for five different directions at an angle  $\theta$  with respect to the anisotropy direction for the  $p = 0.7$  case. Power-law fits are also superposed, showing good agreement with the imposed Kolmogorov-like spectrum for intermediate angles. Bottom panel: the power-law index as a function of the virtual trajectory angle  $\theta$ , for  $p = 0.5$  and  $p = 0.7$ . The deviation toward larger values for  $\theta > 80^\circ$  is evident.

case consistently provides  $p = 0.5$ ).

It is evident that even in the presence of anisotropy, the intermittency prescription is recovered in the synthetic data (Sorriso-Valvo *et al.*, 2006 [119], 2010 [121], Yordanova *et al.*, 2015 [138], Pei *et al.*, 2016 [97]) for recent results on intermittency in solar wind anisotropic turbulence. Only the case at  $\theta = 90^\circ$  displays a discrepancy, showing no intermittency even when  $p = 0.7$ . This is probably due to the shape of the synthetic eddies along the axes, which is also responsible for the weak anisotropy of the spectral power in the isotropic case. Once again, this suggests that for an optimal response of the model, trajectories should be selected with an (even small) angle with respect to the system axes.

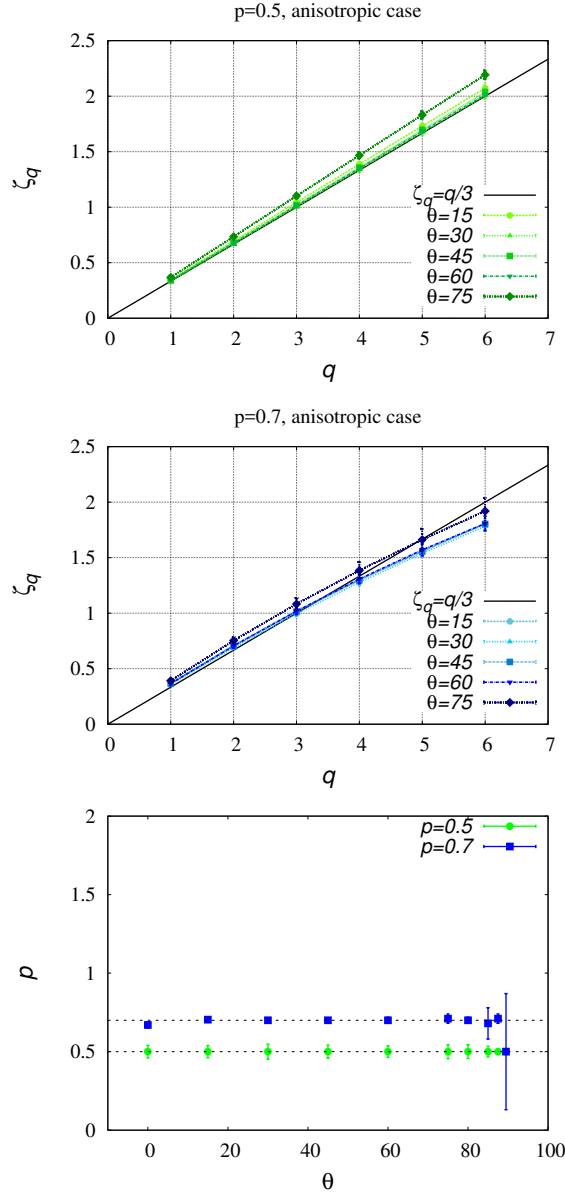


Figure 3.14: The anomalous scaling of the structure functions for five different angles  $\theta$  for the non-intermittent case  $p = 0.5$  (top) and for the intermittent case  $p = 0.7$  (center).  $p$ -model fits are shown as thick solid lines. Bottom panel: the angle dependence of the fitting parameter  $p_{fit}$  for the two cases, with the horizontal lines indicating the input values  $p$ .

### **Kurtosis.**

Finally, in Figure 3.15 we show the variation of the kurtosis with the angle, for the intermittent case (top panel; as expected, the non-intermittent case gives Gaussian values  $F = 3$  and  $\kappa = 0$  at all angles, not shown).

When intermittency is present, the overall effect of anisotropy is to modulate the scaling exponent  $\kappa$  of the kurtosis in response to the variations of the spectral exponent  $\alpha$  increase with the angle (see Figure 3.13), and in particular for large angles  $\theta > 80^\circ$  (bottom panel). The anisotropic realization of the synthetic turbulence presented here is therefore able to capture the major characteristics of spectral anisotropy, and to preserve the intermittency properties.

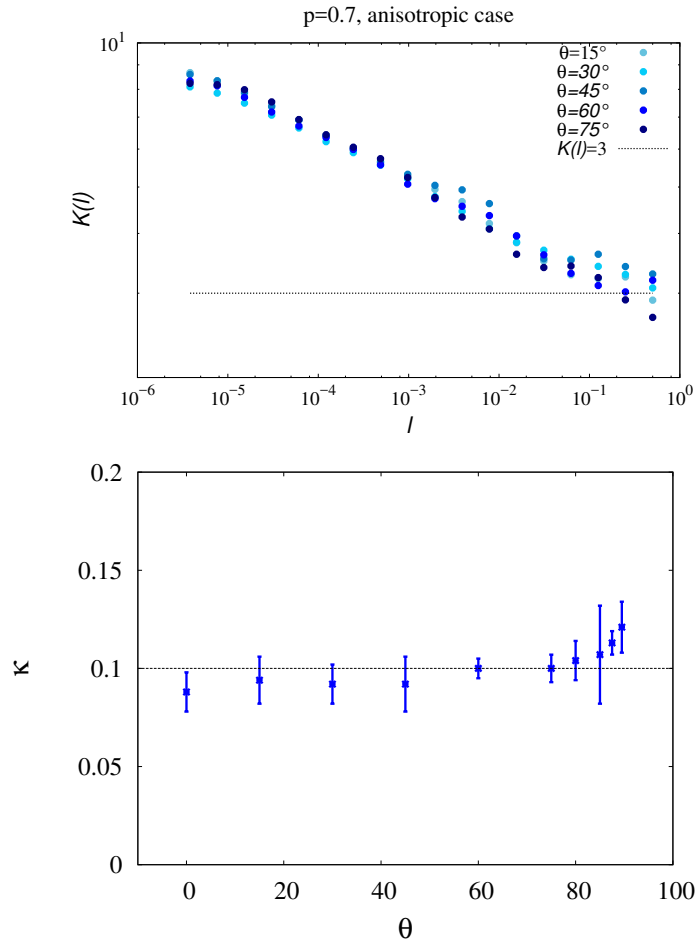


Figure 3.15: Top panel: The scaling dependence of the Kurtosis  $K$  for the  $p = 0.7$  case, and for five angles  $\theta$ . The Gaussian value  $K = 3$  is indicated. Bottom panel: The angular dependence of the scaling exponent  $\kappa$ , which shows an increase at large angles, as observed for the spectral index  $\alpha$  (Figure 3.13).

## 4 Summary

Synthetic turbulence models represent a useful tool which can be used in a variety of situations, mainly when it is necessary to have a realistic representation of a turbulence (either hydrodynamic or MHD) with an extended inertial range. This happens typically in astrophysical contexts, like in the solar wind, where *insitu* measurements have shown the presence of a turbulence with a spectrum extending over several decades of spatial scales. A new model of synthetic turbulence have been presented and discussed, belonging to the class of “wavelet-based” models, in which the synthetic field is obtained by a superposition of base functions at different spatial scales, whose amplitude is determined so as to reproduce a given spectral law for the turbulent field. Moreover, the model reproduces intermittency in the turbulent field by means of a  $p$ -model technique (Meneveau and Sreenivasan, 1987 [87]), in which the spectral energy flux from a given spatial scale to the smaller one is unevenly distributed in space. The modelled turbulent field is three-dimensional in space and solenoidal, so it can be used to describe either an incompressible flow or a turbulent magnetic field. No time dependence is included in the model. Our model shares many aspects with models by Juneja *et al.*, 1994 [61] and by Cametti *et al.*, 1998 [16], but with relevant differences in the algorithm. In fact, one important limitation in the 3D model by Cametti *et al.* [16] is in the memory requirement, which rapidly increases when considering increasing spectral width. In the study presented by these authors the spectral extension is limited to (about) two decades. The algorithm employed by our model has been designed so as to avoid both

large memory employments and long computational times in the evaluation of the turbulent field at a given spatial position. In particular, the computational time  $t_C$  scales proportional to  $\log_2(L_0/\ell_{N_s})$ , where  $\ell_{N_s}$  is the smallest scale included in the model. This is perhaps the most important feature of the model, because it allows to describe a turbulence with a very extended spectral range using a modest computational effort. All the results presented in this paper have been obtained running the model on a desktop computer: in a typical run, which took about 20 min of CPU time, the turbulent field with a spectral extension between 4 and 5 decades has been calculated in a number of spatial positions of the order of  $2.5 \times 10^6$ . Moreover, the memory requirement is very low: each time the field is to be evaluated at a given position, all the parameters defining the involved eddies are re-calculated without keeping any information in the computer memory. The model contains few parameters, namely: (i) the parameter  $h$ , which contributes to determine the index  $\alpha$  of the power-law spectrum; (ii) the parameter  $p$ , which sets the “level” of intermittency and contributes (to a smaller extent) to determine  $\alpha$ ; (iii) the spectral width, fixed by the ratio  $L_0/\ell_{N_s}$ . Such parameters can be tuned in order to reproduce different physical situations. Finally, we explored the possibility to include an anisotropic spectrum, trying to reproduce the situation described by the so-called “critical balance” principle, postulated by Goldreich & Sridhar, 1995 [51] in the case of a MHD turbulence, often advocated for the description of solar wind turbulence. In order to assess the validity of the model and its reliability in reproducing realistic flows, we have run the standard diagnostics for intermittent turbulence and verified that the synthetic field indeed possesses the characteristics that were chosen as input.

To this aim, we have obtained a series of isotropic runs by fixing the scaling exponent  $h$ , and varying the intermittency parameter, which was given three values:  $p = 0.5$  (no intermittency),  $p = 0.7$  (standard Navier-Stokes intermittency),  $p = 0.9$  (strong intermittency). We have then extracted synthetic one-dimensional cuts within the model domain, and have applied time-series analysis techniques: autocorrelation function, power spectrum, probability distribution functions of the field increments, their structure functions, the kurtosis, and a standard multifractal analysis. All the tests gave satisfactory results, showing that the synthetic data reproduce well the required conditions of spectral scaling and intermittency. A small anisotropy originated by the particular shape of the eddy functions is present along the three axes of the system. This was easily mediated by choosing trajectories with an angle with the three axes. We have also explored the geometry of the system by using two anisotropic runs, with  $p = 0.5$  and  $p = 0.7$ , and by imposing the critical balance conditions. Even in the anisotropic case, the output satisfactorily reproduces the expected values of spectral slope and intermittency for all the observables. We can conclude that the model provides a good representation of intermittent turbulence, and is sensitive to the choice of the input parameters, which allows to fine tune the type of turbulence as desired. It is important to acknowledge that the present version of our model is not able to reproduce the skewness of the field increment PDFs, i.e., their nonvanishing third-order moment, universally observed in fully developed turbulence. An improved version of the model that accounts for the appropriate description of the skewness is currently in progress.

Finally, we wish to note that a preliminary version of the present model has been recently employed to study the problem of energetic particle diffusion in a magnetic turbulence (Pucci *et al.*, 2016 [99]). The highly suprathermal speed of the energetic test particles, as observed, for example, in the solar wind, allowed the use of the static turbulent field generated by our model. That investigation has singled out relevant effects on the particle transport related to both large spectral extensions and to intermittency. Thus, a representation of a 3D turbulence with a wide spectrum, as well as a tunable level of intermittency, have been crucial aspects of employing the present synthetic turbulence model in this study. Furthermore, when using our model to run test-particle simulations the integration of particle trajectories is considerably simplified by the possibility to calculate the turbulent field directly at any spatial position, thus avoiding interpolations on a spatial grid (Benzi *et al.*, 1984 [10], Meneveau and Sreenivasan, 1987 [87]).

# Chapter 4

## Turbulence in Kelvin-Helmholtz instability

Turbulence at the interface between the solar wind and the magnetosphere is a very important subject in space physics. Connections between Sun and Earth have been investigated all along in space plasma physics, with the aim of understanding how solar wind interacts with the Earth's magnetosphere. The purpose of this work is to describe this region, characterized by strong gradients of density and magnetic field, by using data taken during satellite magnetopause crossings, in order to study the evolution of the turbulence at low latitude in the boundary layer system, driven by the development of the Kelvin Helmholtz instability (KH). For this work we have used data from Themis and Geotail spacecraft. This is motivated by the need to investigate, mainly magnetopause under northward magnetic field conditions, at low latitude boundary layer. It is very important to be able to determine the properties of plasma turbulence and intermittency inside magnetosheath, given the great interest in the mechanisms associated with KH and terrestrial magnetosphere. Properties of turbulence can help to understand how

the particles transport works from solar wind and magnetosphere and, more generally, what are the mechanisms of interaction between these two regions of the near-Earth space. Moreover, it is interesting to study the evolution of turbulence, as a result of the development of KH instability as it moves away from the Sun along the tail-flank magnetopause, both on the dawn and on the dusk flanks of the terrestrial magnetosphere. Thus, the same analysis tools used for the study of intermittent turbulence generated by the synthetic model (see Chapter 2), will be also employed for the analysis of space plasma data. Our aim is to provide a complete and quantitative characterization of turbulence and of the associated intermittency in this region, which is still poorly studied.

## **1 Solar Wind and Earth's magnetosphere: description and interaction**

The Sun's plasma comes from the hot corona, where temperature is so high that the Sun's gravity cannot confine it. This high speed plasma, called "solar wind", is a stream of ionized particles, mainly electrons, protons and  $\alpha$  particles, observed indirectly for the first time by Parker, 1958 [95]. Presence of unexpected double tails in comets and phenomena like aurorae had led him to assume the presence of an ionized flux of particles, later observed thanks to space mission that followed afterwards. During low solar activity periods, the solar wind can be separated in two major components that alternate in space, characterized by different bulk speed and originating in different type of regions on the solar surface (see Figure 4.1): fast ( $\sim 700$  km/s), tenuous and relatively homogeneous solar wind at high heliolatitudes

emanating from large polar coronal holes that persisted throughout most of the solar cycles (McComas *et al.*, 2008 [85]) characterized by almost open magnetic field lines configuration; slower ( $\sim 400$  km/s), denser, and highly variable wind at lower latitudes (McComas *et al.*, 2000 [84]), coming instead from equatorial regions of the Sun. Solar wind flows in all directions and

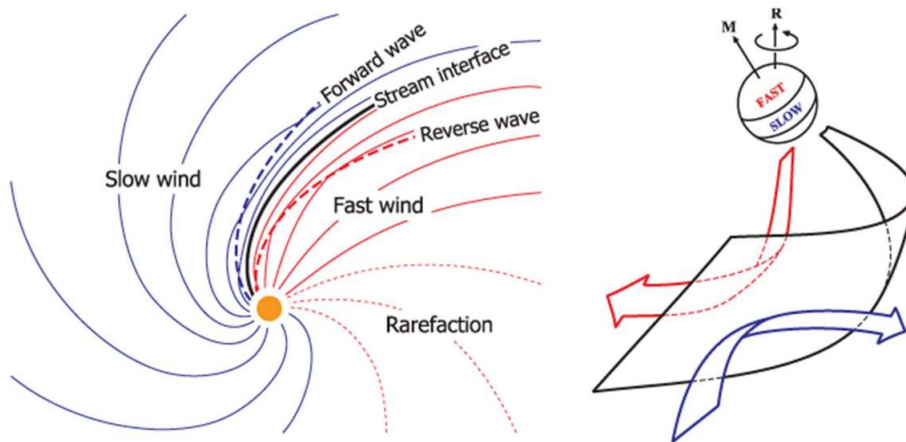


Figure 4.1: Co-rotating interaction region where fast and slow wind zone are highlighted in the Parker's Spiral, taken by <http://solarphysics.livingreviews.org/Articles/lrsp-2013-5/CIR-2panel.png>

it interacts with the magnetosphere of the planets, a region of space where the magnetic field of the planet dominates on the plasma dynamics. This also happens for the Earth where the interplanetary magnetic field (IMF) plays a huge role in how the solar wind interacts with Earth's magnetosphere. Because of the rotation of the Sun, the magnetic field has a spiral shape, known as Parker Spiral (Parker, 1958 [95]), with a complex geometry because of the combination of the wind radial motion and the rotation of the Sun. Plasma and magnetic field lines are linked one to each other, according to the frozen-in theorem due to Alfvén, 1940 [3], which states that,

in the MHD regime and for negligible resistivity, the motion of the plasma particles and of the magnetic field line is strongly coupled, so that one can “transport” the other. The solar wind exerts a pressure on Earth’s magnetic field, which is compressed on the Sun-facing side and stretched into a very long tail on the side away from the Sun. This complex magnetic envelope is called magnetosphere.

The IMF component  $B_z$  perpendicular to the ecliptic has a fundamental role in solar wind plasma transfer into the magnetosphere. In Figure 4.2 two different configurations of the geomagnetic field are shown, according to the interplanetary solar wind conditions. The magnetosphere configuration is classified as “open” (top panel) or “closed” (bottom panel), according on how it interacts with the interplanetary magnetic field.

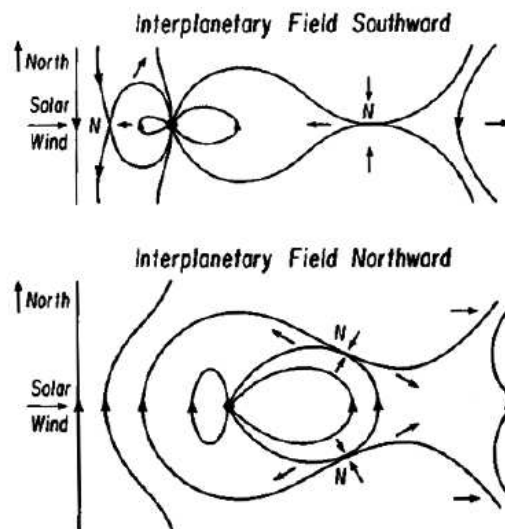


Figure 4.2: Magnetosphere configurations: “open” in the top figure and “closed” in the bottom. Arrows indicate the direction of the flowing plasma (taken by Dungey,1961 [33]).

The magnetic field of the Earth’s magnetosphere essentially points northward. Then, when the north-south component ( $B_z$ ) of the interplanetary magnetic field is oriented southward, it is antiparallel with geomagnetic field lines. This makes possible magnetic reconnection processes, that take place both at the nose and at the tail of the magnetosphere (see Figure 4.2 top panel). The solar wind particles are accelerated and pushed inside the magnetosphere, as a consequence of the reconnection process (Dungey, 1961 [33]), and enter the magnetosphere much easily. Solar wind particles are guided into the atmosphere by Earth’s magnetic field lines, colliding with the oxygen and nitrogen atoms that make up our atmosphere and causing phenomena like auroras. During periods characterized by a prevalently northward interplanetary magnetic field, instead, there is no dayside reconnection, but reconnection takes place at the south and north geomagnetic poles, as revealed by satellites observations (Terasawa *et al.*, 1997 [129], Borovsky *et al.*, 1998 [12], Wing and Newell, 2002 [136]). Under this conditions cold dense solar wind plasma is still injected into magnetosphere, in particular along the flanks. Moreover, a broad boundary layer is observed to be present at low latitude, referred to as “low-latitude boundary layer” (LLBL) (Fujimoto *et al.*, 1998 [49], Hasegawa *et al.*, 2004 [58], Sckopke *et al.*, 1981 [109]), where a mixture of solar wind and magnetospheric populations coexist (Fujimoto *et al.*, 1998 [49]). Different possible mechanisms have been proposed to explain these observations: high latitude magnetic reconnection called “double lobe reconnection” (Song and Russell, 1992 [117]), anomalous diffusion across the magnetopause, (Matsumoto and Seki, 2010 [79]) and low latitude Kelvin-Helmoltz instability (see section 2).

## 1.1 Magnetospheric plasma region

On the Sun-facing side, the solar wind compresses the magnetosphere to a distance of about  $\sim 10$  Earth radii (hereafter indicated by  $R_E$ ); on the downwind side, the magnetotail stretches for more than  $\sim 1000 R_E$ . The magnetosphere is filled with tenuous plasmas of different densities and temperatures, which originate from the solar wind and the ionosphere. When solar wind approaches the magnetosphere, its velocity slows down abruptly because of the planet magnetic field which hinders the flow giving rise to a bow shock (see Figure 4.3). Just after the shock, solar wind forms the

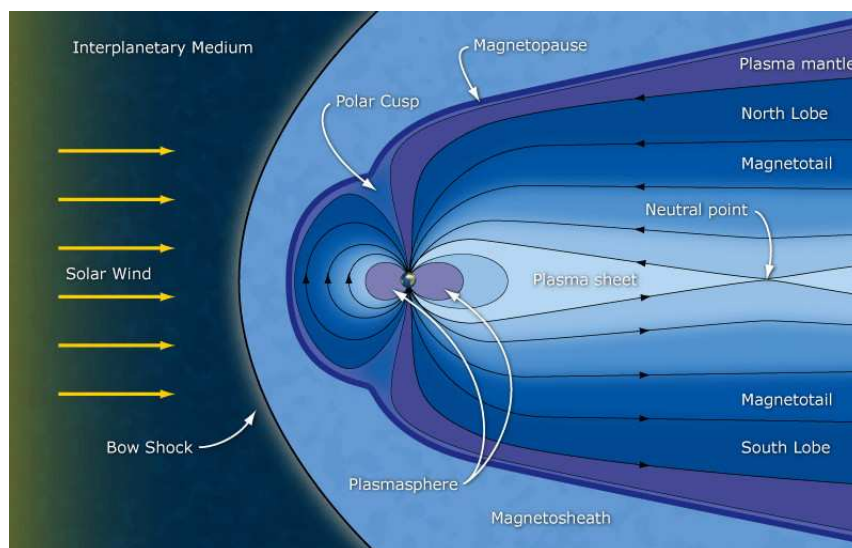


Figure 4.3: Scheme of the interaction between solar wind and Earth's magnetosphere (Copyright: ESA, adopted from picture courtesy C. Russel).

magnetosheath about  $10 - 13 R_E$  far from the Earth, a region characterized by a very turbulent medium where both the magnitude and the direction of the magnetic field strongly vary. Just below the magnetosheath we find the magnetopause (MP) boundary, that separates the solar wind from the

planetary magnetic field. Magnetopause location is determined by pressure equilibrium between planetary magnetic pressure and solar wind dynamic pressure. The MP has a bullet-shaped front, gradually changing into a cylinder, not being a static layer, but rather moving towards or away from the Earth at velocities between 10 – 20 km/s. Often satellites cross the MP, because of this rapid motion rather than of the velocity of the satellite itself and during these crossings they alternately enter or exit the magnetosphere (multiple crossings). In the absence of a magnetic field perpendicular to the layer it can be characterized as a tangential discontinuity. This argument is discussed in more detail in the next section.

## 1.2 Discontinuities in space plasma physics: magnifying glass on the magnetopause

Shocks and discontinuities are nonlinear phenomena that are commonly observed in space plasmas. The interplanetary space is filled with plasma having different properties. The interaction between different plasmas allows for the formation of very thin separation layers known as discontinuities, surfaces where physical quantities exhibit abrupt variations. Magnetospheric discontinuities are mainly classified into tangential or rotational discontinuities and shocks. A clear scheme for tangential and rotational discontinuities can be found in Burlaga, 1995 [15] (see Figure 4.4). In the left panel a tangential discontinuity is represented, characterized by no mass or magnetic flux across it and balanced total (kinetic + magnetic) pressure. Velocities and magnetic field can change across the discontinuity, but the normal components  $B_n$  and  $v_n$  are both vanishing. The right panel represents a rotational

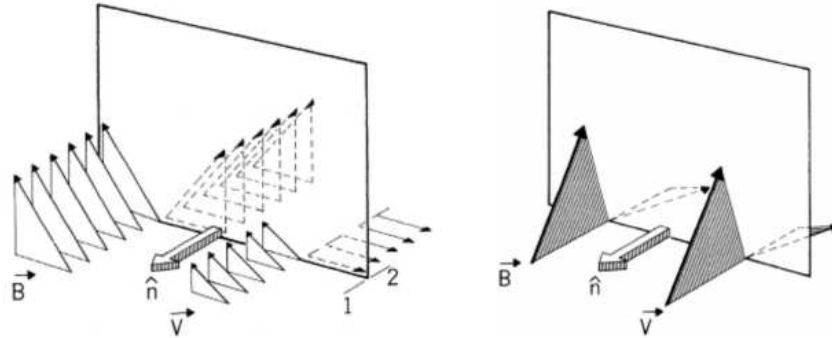


Figure 4.4: Types of discontinuities in IMF: tangential discontinuity (left panel) and rotational discontinuity (right panel) (Burlaga, 1995 [15]).

discontinuity, characterized by a finite normal mass flow but a continuous  $v_n$ , where the magnetic field direction changes with a non-zero component normal to the current layer. The rotational discontinuity is not static and it propagates along the direction of the normal to the surface with the Alfvén speed  $v_A = B_n/\sqrt{4\pi\rho}$ . Another type of discontinuity is called a shock if there are both mass flux and magnetic flux across it, characterized by the coplanarity of the magnetic field (Belmont *et al.*, 2013 [8]), i.e. the magnetic field vectors on the two sides of the shock are coplanar with the shock normal vector. In addition to this, there is a change in the density, as well. Sometimes, the rotational discontinuity is classified also as a non-compressional shock because there is no density variation across the layer. We focus our attention on the magnetopause, a finite thickness discontinuity defined by the balance between the solar wind dynamic pressure and the magnetosphere magnetic pressure. This complex layer presents several configurations, according to the direction of the interplanetary magnetic field. These configurations may approximately correspond either to a rotational or a tangential discontinuity.

The closed magnetopause, where there is no magnetic reconnection between the solar wind and the geomagnetic field lines (see Figure 4.2 bottom panel), corresponds to a tangential discontinuity. Instead, the open magnetopause is a rotational discontinuity, and it occurs when the IMF is directed southward and when magnetic reconnection takes place at the dayside magnetopause, as shown in the top panel in Figure 4.2. It is also notable that some quantities like as normal velocity, mass density and thermal pressure should be continuous across the discontinuity layer, while these conditions are not often satisfied at the magnetopause. For this reason magnetopause is defined as a disturbed tangential discontinuity (Volland 1995 [134]), having a small normal component of magnetic field,  $B_n \geq 0$ . In Figure 4.5 a schematic illustration of Earth's magnetotail is shown, emphasizing the different plasma regions. In the equatorial plane, the magnetopause layer is represented by a smooth curve, that extends from the "day" towards the geomagnetic tail anti-sun direction. Instead, a continuous solution that connects the dayside of the magnetopause to the nightside does not exist on the meridian plane. Indeed, at high latitude the tangent to the magnetopause is discontinuous at one point called cusp, due to the particular geometry of the magnetic field dipole. However, although the surface is uneven, the magnetic field lines are not affected by any discontinuity but just changing their topology from type "day force lines" to "night force line" such as stretched force lines in the geomagnetic tail. Magnetic field rotates through the magnetopause, moving from low intensity interplanetary magnetic field to a much more intense magnetospheric field. This implies that the magnetopause has the structure of a current layer as shown in Figure 4.6. Ions and electrons are specularly

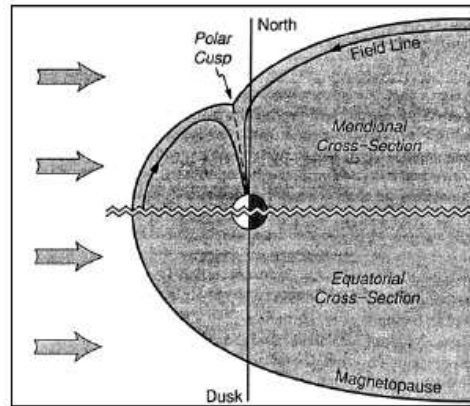


Figure 4.5: Sections of magnetopause on the meridian and equatorial plane (Baumjohann and Treumann, 1999 [6]).

reflected inside the magnetopause. Particles run through the middle of the circular orbit of radius equal to their radius of gyration, and then return to the “magnetosheath”. Because of the difference between the senses of rotation of ions and electrons, a current layer is generated. The latter has a thickness of the order of the radius of gyration of the ions. This current has a direction such as to generate an additional magnetic field, that compresses the field on the magnetospheric side increasing its intensity, while reducing the magnetic field on the magnetosheath side. According to this description, the Earth’s magnetic field near the magnetopause on the “day” is different from the dipolar and may be represented in terms of a “compressed” dipole. This current layer separates the magnetic field of the magnetosheath from that of the magnetosphere. A key feature of the magnetopause is the presence of a “boundary layer” (BL), adjacent to it and located inside the magnetosphere, where plasma has characteristics similar to that of magnetosheath. This BL extends on the magnetopause at all latitudes although its properties

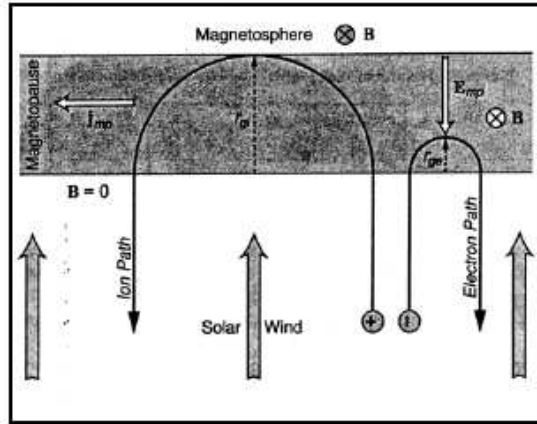


Figure 4.6: Mirror reflection of ions and electrons on the magnetopause (Baumjohann and Treumann, 1999 [6]).

vary substantially from region to region. It is possible to identify three main regions: the “low latitude boundary layer” (LLBL), the “entry layer” (EL) and the “plasma mantle” (PM) (Hones *et al.*, 1972[59]; Rosenbauer *et al.*, 1975 [104]; Paschmann *et al.*, 1976 [96]; Haerendel *et al.*, 1978 [52]; Eastman and Hones, 2000 [36]). These regions are shown schematically in Figure 4.7.

## 2 Kelvin-Helmholtz instability

Turbulence at the interface between the solar wind and the magnetosphere is a subjects worth studying in space physics. The Kelvin-Helmholtz Instability (KH) can drive waves at the magnetopause. These waves can grow to form rolled-up vortices and facilitate transfer of plasma into the magnetosphere. This mechanism is considered one of the most important responsible for populating the LLBL during periods of northward interplanetary mag-

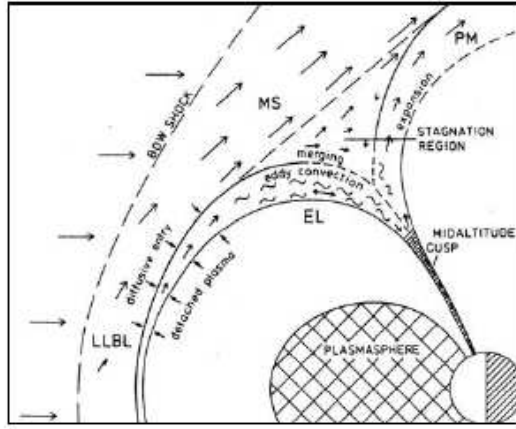


Figure 4.7: Schematic representation of magnetopause and BL at various latitude on the meridian plane (Haerendel and Paschmann, 1978 [52]).

netic field (IMF), when reconnection at the equatorial magnetopause is less effective (Bavassano Cattaneo *et al.*, 2010 [7]). Kelvin-Helmholtz instability originates when at any time two layers of a fluid (or two different fluids) are in relative motion. In a plasma, the presence of a sufficiently intense magnetic field can inhibit the development of this instability. The Kelvin-Helmholtz instability can grow at the low-latitude magnetopause, situated between the magnetosheath, characterized by an antisunward flow of shocked solar wind, and the outer plasma sheet characterized by stagnant or weak sunward flows (Hasegawa *et al.*, 2009 [57]). When the IMF is northward, the equatorial component of the magnetic field can be negligible at low latitude and so the KH instability can develop eventually producing fully rolled-up vortices. There is an extensive literature for understanding development of this instability along the inner edge of the low-latitude boundary layer (LLBL) (Sonnerup, 2008 [118]; Scokpe *et al.*, 1981 [109]). The resulting waves or vortices are

suggested to have some relation to aurorae with spatially periodic forms (e.g., Lui *et al.*, 1989 [74]; Yamamoto, 2008 [137]). There are observational evidence of the KH in the form of surface waves propagating antisunward along the magnetopause (Sckopke *et al.*, 1981 [109]; Chen *et al.*, 1993 [22]; Kivelson and Chen, 1995 [64]; Fairfield *et al.*, 2000 [39]). A shared point of view considers KH waves or vortices to be more frequent during northward IMF conditions than during southward IMF (Kivelson and Chen, 1995 [64]; Fujimoto *et al.*, 2003 [50]; Hasegawa *et al.*, 2006 [55]). Those vortices are believed to be a key ingredient for the formation of the thick LLBL (Mitchell *et al.*, 1987 [88]) and of the cold and dense plasma sheet (CDPS) (Terasawa *et al.*, 1997 [129]; Wing and Newell, 2002 [136]), both encountered predominantly under northward IMF. KH waves are known to develop at a planetary magnetopause, where small scale perturbations gain energy from the velocity shear between the magnetospheric and magnetosheath plasma and thereby grow into large scale rolled up vortices (Sundberg, 2012 [126]). When the waves reach a turbulent state, plasma and energy are transported from the dense magnetosheath into the more rarified magnetosphere. There are many observational evidence to demonstrate presence of KH waves on both the dawn and dusk flank of the terrestrial magnetosphere spanning approximately from the dawn-dusk meridian to 30 Earth radii down the magnetotail (e.g., Chen and Kivelson, 1993 [21]; Kokubun *et al.*, 1994 [66]; Fairfield *et al.*, 2000 [39], 2003 [40], 2007 [41]; Otto and Fairfield, 2000 [92]; Farrugia *et al.* 2000 [43]; Hasegawa *et al.* 2004 [56]). It looks like that the events arise in the proximity of the equatorial plane, where the magnetopause is believed to be susceptible to the KH instability (e.g., Hasegawa *et al.*, 2004 [56]; Foullon *et al.*,

2008 [44]).

### 3 Data set overview

In this work we analyze a collections of events, on the basis of the Geotail observations, made over 9 years from 1995 to 2003. To enrich the dataset, additional two events of THEMIS observations made during November 2008, have been investigated. Events are encountered along the flank magnetopause, most of which are behind the dawn-dusk terminator, consistent with the roll-up from Geotail observations, showing quasi-periodic plasma and field fluctuations in the flank low-latitude boundary layer (LLBL) under northward IMF, associated with KH waves. Geotail events have been studied by Hasegawa *et al.*, 2006 [55], Fujimoto *et al.*, 1998 [49], Fairfield *et al.*, 2000 [39], 2003 [38] and Stenuit *et al.*, 2002 [123], while THEMIS events have been studied by Lin *et al.*, 2014 [73]. Their survey shows that such rolled-up events do occur on both dawn and dusk flanks and are not rare for northward IMF conditions. In addition, in all the rolled-up cases, magnetosheath-like ions are detected on the magnetospheric side of the boundary. These findings indicate that the KH plays a nonnegligible role in the formation of the flank LLBL under northward IMF. As a result, a total of 18 rolled-up events were identified by Hasegawa *et al.*, 2006 [55], nine events on each flank of the magnetosphere. In the same region Lin *et al.*, 2014 [73] identified 14 events with rolled-up vortices under the northward IMF at the LLBL and they collected 42 events from the observations of the Geotail, Double Star TC-1, and Cluster, for a statistical study of the KH wave properties. This prelude and research were done to collect a big enough dataset of KH events,

with the aim of characterizing the intermittent turbulence that takes place inside them. Furthermore, we study the evolution of turbulence as a result of the development of KH along the flank magnetopause. Each event has been analysed employing the standard diagnostics we have used previously (i.e. the spectral analysis and the scale-dependent statistics of the field increments). For each event we have obtained: the autocorrelation function which gives useful information about the correlation scale of the field; the associated energy power spectrum, whose power-law scaling exponent has to be compared with Kolmogorov-like spectrum observed at MHD scales, while a steeper power law is suggested below proton scales; the Probability Distribution Functions (PDFs) of the scale-dependent increments, whose deviation from Gaussian will qualitatively illustrate the presence of intermittency and finally the kurtosis with its scaling exponent.

### **3.1 The GEOTAIL mission**

GEOTAIL is a collaborative mission of Japan and the USA, of the agencies JAXA/ISAS (Japan Aerospace Exploration Agency/Institute of Space and Astronautical Science that became part of JAXA in October 2003), and NASA (National Aeronautics and Space Administration), respectively. Together with Wind, Polar, SOHO, and Cluster projects, it constitute a cooperative scientific satellite project designated the International Solar-Terrestrial Physics (ISTP) program, which aims at gaining improved understanding of the physics of solar terrestrial relations. The spacecraft was designed and built by ISAS, while the launch was provided by NASA's Goddard Space Flight Center on July 24, 1992.

The Geotail mission measures global energy flow and transformation in the magnetotail to increase understanding of fundamental magnetospheric processes. This will include the physics of the magnetopause, the plasma sheet, reconnection and neutral line formation (i.e., the mechanisms of input, transport, storage, release and conversion of energy in the magnetotail).

The Geotail mission is divided into two phases. During the initial two-year phase, the orbit apogee was kept on the night side of the Earth by using the Moon's gravity in a series of double-lunar-swing. After fulfilling its original objective of studying the dynamics of the Earth's magnetotail over a wide range of distance, extending from the near-Earth region ( $8R_E$  from the Earth) to the distant tail (about  $200R_E$ ), its orbit was changed. In February 1995, phase two was commenced as the apogee was reduced to  $30R_E$ , where it has provided data on most aspects of the solar wind interaction with the magnetosphere. This orbit also allows us to study the boundary region of the magnetosphere, as it skims the magnetopause at perigees. Real-time telemetry data transmitted in the X-band are received at the Usuda Deep Space Center (UDSC) in Japan. There are two tape recorders on board, which allow daily 24-hour data coverage. The data are collected in playback mode by the NASA Deep Space Network (DSN). The GEOTAIL spacecraft carries seven scientific instruments<sup>1</sup>: an EDF (Electric Field Detector) used to study of the coupling of the E-field in the near-Earth magnetosphere and in the ionosphere (in particular during substorms); a MGF (Magnetic Field Measurement) that studies the magnetic field in a frequency range  $< 50Hz$ ;

---

<sup>1</sup>Websites for more details: [www.jaxa.jp/projects/sat/geotail/](http://www.jaxa.jp/projects/sat/geotail/), [www.isas.jaxa.jp/e/enterp/missions/geotail/](http://www.isas.jaxa.jp/e/enterp/missions/geotail/), [www.isas.jaxa.jp/e/enterp/missions/geotail/index.shtml](http://www.isas.jaxa.jp/e/enterp/missions/geotail/index.shtml).

a HEP (High Energy Particles Experiment) for measurement of high energy particles up to 25 MeV for electrons, 35 MeV for protons, and 210 MeV/charge for ions. Measurements may indicate the plasma boundary surfaces and reflect whether magnetic field lines are open or closed; a LEP (Low Energy Particles Experiment) to study of the dynamics of the magnetotail plasmas, plasma circulation and its variability in response to fluctuations in the solar wind and in the interplanetary magnetic field. Measurement of electrons from 6 eV to 36 keV, and ions from 7 eV to 42 keV/charge. The LEP consists of three sensors: LEP-EA (measures the 3-D velocity distributions of hot plasma in the magnetosphere), LEP-SW (measures the 3-D velocity distributions of solar wind ions), and LEP-MS (energetic ion mass spectrometer), with common electronics (LEP-E); a PWI (Plasma Waves Investigation) for the study of the wave phenomena related to plasma dynamics in the different regions on various scales (phenomena include magnetic-field-line merging, moving plasmoids, and particle acceleration); an EPIC (Energetic Particle and Ion Composition Experiment) used to measure the charge, mass, and energy of ions, for the study of the relative importance of ion sources and mechanisms for acceleration, transport and loss of particles, the formation and dynamics of magnetospheric boundary layers; a CPI (Comprehensive Plasma Investigation) that measures the 3-D plasma in the Earth's magnetotail. The plasma data from GEOTAIL are supposed to be correlated with the magnetic field, plasma waves, electric particles, and auroral imaging data to determine magnetotail plasma dynamics.

### 3.2 The THEMIS mission

The Time History of Events and Macroscale Interactions during Substorms (THEMIS) mission was originally a constellation of five NASA satellites (THEMIS A through THEMIS E) launched on February 17, 2007 from Cape Canaveral. Three of the satellites remain in the magnetosphere, while two have been moved into orbit near the Moon. Those have been renamed ARTEMIS for Acceleration, Reconnection, Turbulence and Electrodynamics of the Moon's Interaction with the Sun. THEMIS B became ARTEMIS P1 and THEMIS C became ARTEMIS P2. The five THEMIS spacecraft (probes) were placed in highly elliptical orbits where the spacecraft line up at apogee every four days. Three inner probes  $\sim 10R_E$  from Earth monitor current disruption onset, while two outer probes at 20 and  $30R_E$  remotely monitor plasma acceleration due to lobe flux dissipation. Magnetic field lines map phenomena occurring at the inner spacecraft to the ground arrays, where they can be observed as nightside auroral displays and geomagnetic perturbations. The apogee rotates slowly around the Earth to cover the dayside, dawnside, nightside, and duskside of the magnetosphere. Initially, right after launch in 2007, THEMIS spacecraft were lined up in the same orbit. Since 2011, P1 and P2 have become ARTEMIS and orbit the moon, while the 3 remaining Earth-orbiting probes are able to synergize observations with other heliophysics missions such as Van Allen Probes (VAP) and Magnetospheric Multiscale (MMS). During the first summer season (May-September 2007), the THEMIS spacecraft was arrayed like pearls on a string following identical orbits with apogees in the dayside magnetosheath. With separa-

tion distances ranging from 100's of km to one Earth radii, the spacecraft was able to make the observations on scales suitable for studies of reconnection micro and meso-physics, magnetopause boundary layer structure and motion, and wave propagation in the magnetosheath. Instead, during the second summer season (May-September 2008), the THEMIS spacecraft was arrayed in orbits, which permit them to simultaneously observe the pristine solar wind, foreshock, magnetosheath, and outer magnetosphere. This configuration is ideal for determining how kinetic and magnetohydrodynamic processes in the region upstream from the Earth modify the nature of the solar wind-magnetosphere interaction. In particular, the observations were used to determine the characteristics of hot flow anomalies and diamagnetic cavities within the foreshock, the propagation of transmitted solar wind discontinuities through the magnetosheath, and to search for solar wind triggers of magnetopause instabilities. The five satellites carry identical instrumentation: a fluxgate magnetometer (FGM) that measures the background magnetic field and its low frequency fluctuations (up to 64 Hz) in the near-Earth space; an electrostatic analyzer (ESA) used to measure plasma over the energy range from a few eV up to 30 keV for electrons and 25 keV for ions; a solid state telescope (SST) that analyze superthermal particle distribution functions, namely the number of ions and electrons coming towards the spacecraft from specified directions with specified energies within the energy range from 25 keV to 6 MeV; a search-coil magnetometer (SCM) measures low-frequency magnetic field fluctuations and waves in three directions, which antennas cover the frequency bandwidth from 0.1 Hz to 4 kHz; an electric field instrument (EFI) that measures the electric fields in three directions.

## 4 Analysis of Geotail and THEMIS data

We have consulted the ASCII listings of Geotail MGF high resolution magnetic field data (1/16 sec sampling), where we got the data of magnetic field. Instead, the ASCII listings of Geotail LEP ion moment data (12 sec sampling) was adopted to get the data of density and plasma velocity. The official website <http://themis.ssl.berkeley.edu> provides THEMIS data. We have worked with magnetic field data by FGM instrument at high resolution (1/128 s sampling), density and plasma velocity data taken by MOM (on-board moments) instrument at low resolution (3 sec sampling). We have chosen 17 events from the entire collection of 19, reported by Hasegawa et al., 2006 [55]. The reason is to achieve a set of events with enough points to allow the analysis, neglecting those with few points and many data gaps which could affect the statistical analysis. A similar selection procedure was done for the THEMIS events. In that case we have chosen 2 events from the set of 14, reported by Lin *et al.*, 2014 [73]. All events are listed in the table in Figure (4.8), in which their observed conditions are also included. The latter figure shows the following informations (taken by Hasegawa *et al.*, 2006 [55]): the date; the time interval; the GSM position measured in  $R_E$ ; the IMF condition, where the symbol NBZ means northward IMF; the ion mixing status and the fluctuation period, related to the rolled-up vortices. The ion mixing status consists of two definitions: the “mixed” status means that a significant amount of cool magnetosheath-like ions, was present on the magnetospheric side of the magnetopause, where density  $n > 1/cm^3$ , while “weakly-mixed” means that magnetosheath-like ions were found on magnetospheric side, but

GEOTAIL MISSION					
Date	Time Interval	GSM Position(RE)	IMF Condition	Ion Mixing Status	Fluctuation Period
1995-03-24	0600-0800 UT	(-15, 20, 4)	Extended strong NBZ <sup>a</sup>	Mixed <sup>d</sup>	2 - 3 min
1997-01-10	2050-2400 UT	( -7, 16, 4)	ND <sup>b</sup> NBZ after N-turning	Weakly mixed <sup>d</sup>	2 - 3 min
1997-01-11	0400-0500 UT	(-13, 16, 4)	Extended strong NBZ	Mixed	~ 3 min
1997-02-12	1430-1600 UT	(-13, 22, 3)	Extended strong NBZ	Mixed	~ 2 min
1998-04-13	0315-0430 UT	(-18, 20, 4)	Extended strong NBZ	Mixed	2 - 3 min
1998-08-01	0530-0730 UT	( 0, 14, -3)	Extended strong NBZ	Mixed	~ 3 min
1998-12-27	1800-2100 UT	(-21,-22,-4)	Extended strong NBZ	Mixed	3 - 4 min
1999-02-15	1445-1515 UT	(-4, 16, 2)	NBZ after N-turning	Mixed	~ 2 min
1999-07-20	0630-0730 UT	(-3, 16,-2)	Extended strong NBZ	Mixed	2 - 3 min
2000-11-01	1030-1200 UT	(-8, -16, 6)	Extended strong NBZ	Mixed	2 - 3 min
2001-01-25	1330-1630 UT	(-22,-21, 0)	Extended strong NBZ	Mixed	~ 5 min
2001-11-16	1900-2000 UT	(-7,-18, 2)	Extended NBZ (often ND)	Weakly mixed	2 - 3 min
2001-12-07	2000-2130 UT	(-11,-19,-1)	SNBZ <sup>c</sup> after N-turning	Weakly mixed	~ 3 min
2002-03-25	0530-0900 UT	(-12,-17,-2)	Extended strong NBZ	Mixed	2 - 3 min
2002-03-25	1000-1300 UT	(-8, -16, -1)	Extended strong NBZ	Mixed	2 - 3 min
2002-10-15	2100-2300 UT	(-1, -14, 3)	Extended NBZ	Mixed	2 - 3 min
2003-07-17	0330-0500 UT	(-13, 23, -1)	ND NBZ after N-turning	Weakly mixed	~ 2 min

THEMIS MISSION					
Date	Time Interval	GSM Position(RE)	IMF Condition	Ion Mixing Status	Fluctuation Period
2008-11-06	0850-0920 UT	(-0.3,-15.3,4.6)	not specified	not specified	not specified
2008-11-18	0720-0730 UT	(-2.3,-17,3.4)	not specified	not specified	not specified

<sup>a</sup>NBZ: northward IMF; <sup>b</sup>ND: non dominant; <sup>c</sup>SNBZ: strong NBZ; <sup>d</sup>Mixed/Weakly mixed means that a significant/small amount of magnetosheath ions was identified, i.e.,  $n > (\leq) 1/cm^3$ , in the BL.

Figure 4.8: Event List of rolled-up vortices detected by Geotail over 9 years from 1995 to 2003, adapted from Hasegawa *et al.*, 2006 [55]. The last two events were detected by THEMIS probe C, adapted by Lin *et al.*, 2014 [73].

their density was lower than  $n < 1/cm^3$ . The fluctuation period instead, corresponds to the perturbations in the flow that are interpreted by Hasegawa *et al.*, 2006 [55] as being due to vortical motions of plasma (e.g., Fujimoto *et al.*, 2003 [50]), whereas those in the field are due to deformation of the field lines when those near the magnetopause are brought into rolled-up vortices (Hasegawa *et al.*, 2004 [58]; Takagi *et al.*, 2006 [127]).

The locations of the events are presented in Figure (4.9). The coordinate system is the Geocentric Solar Magnetospheric (GSM) system, described in more details in Appendix B.

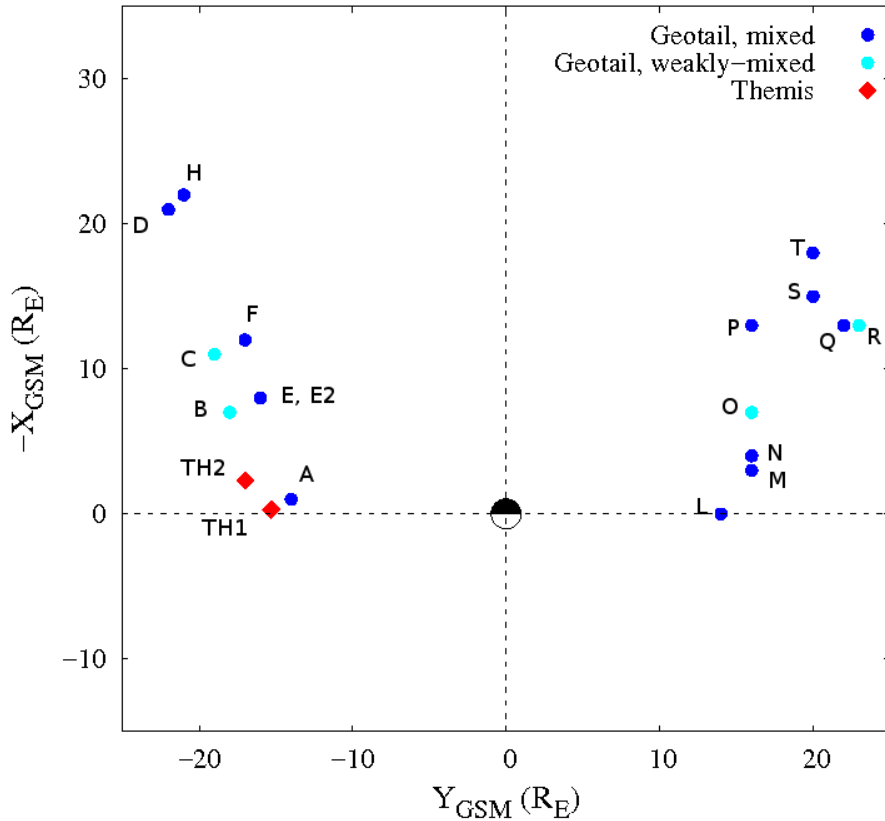


Figure 4.9: Locations of rolled-up KH events identified from Geotail (light-blue/blue dot) and THEMIS (red diamond).

As can be seen, all events are located along the flank magnetopause, most of them are behind the dawn-dusk terminator, and more precisely: nine on the dawnside (left-side in the Figure (4.9)) and nine on the duskside (right-side in the Figure (4.9)). The events E and E2 present the same coordinate X (GSM), so they are overwritten on each other.

Before proceeding to the analysis of the turbulence properties in the dataset, it is necessary to test the validity of the Taylor hypothesis, which allows the switch between time and space measurements (Taylor, 1938 [128]). In particular, the time series of a field can be assumed to be an instantaneous spatial scan of the field if the typical velocities associated with the dynamics are slower than the probe speed inside the medium.

In the cases under examination we need to test whether the plasma speed in the spacecraft frame  $v'_{ms}$  (the subscript “ms” indicates “magnetosheath” region, where our dataset is located) is faster than the typical speed of dynamical processes. For space plasmas, such dynamics is usually associated to the Alfvén speed  $v_A$ , which is the typical propagation speed of the plasma fluctuations. Of course,  $\mathbf{v}'_{ms} = \mathbf{v}_{ms} - \mathbf{v}_{sc}$ , where  $\mathbf{v}_{ms}$  and  $\mathbf{v}_{sc}$  are the plasma speed and the spacecraft speed in the GSM frame, respectively. Since  $v_{ms} \gg v_{sc}$ , then we can assume that  $\mathbf{v}'_{ms} \simeq \mathbf{v}_{ms}$ . To be more precise, for a turbulent distribution of modes in wavevector space, the plasma-frame frequency term  $\omega$  and spatial advection term  $\mathbf{k} \cdot \mathbf{v}_{ms}$ , both contribute to the spacecraft-frame frequency (Klein *et al.*, 2014 [65]), according to the relation (Taylor, 1938 [128]):

$$\omega_{sc} = \omega + \mathbf{k} \cdot \mathbf{v}_{ms} \quad (4.1)$$

As stated above, assuming  $\omega \sim kv_A$ , and since the solar wind has typically a super-Alfvénic velocity,  $v_{ms} \gg v_A$ , then equation (4.1) implies  $\omega_{sc} \simeq \mathbf{k} \cdot \mathbf{v}_{ms}$ , thereby relating the spacecraft-frame frequency directly to the wavenumber of spatial fluctuations. This corresponds to the Taylor hypothesis (Taylor, 1938 [128]; Fredricks and Coroniti, 1976 [46]).

Values of the mean bulk speed and of the Alfvén speed were estimated for each sample, and their values are listed in the table in Figure (4.10).

	<b>B<sub>0</sub> (nT)</b>	<b>δB (nT)</b>	<b>v<sub>A</sub> (km/s)</b>	<b>v<sub>ms</sub> (km/s)</b>
<b>A</b>	41.7	4.00	547	332
<b>B</b>	20.1	3.25	315	183
<b>C</b>	19.6	2.31	345	257
<b>D</b>	12.5	1.30	204	247
<b>E</b>	24.3	2.84	268	298
<b>E2</b>	22.7	1.98	400	299
<b>FsetA</b>	22.8	1.88	402	299
<b>FsetB</b>	26.9	2.51	344	347
<b>H</b>	11.4	1.72	182	182
<b>L</b>	29.7	4.16	286	92
<b>M</b>	26.9	3.20	200	230
<b>N</b>	17.8	5.72	234	279
<b>O</b>	23.1	6.28	232	169
<b>P</b>	26.1	5.69	268	219
<b>Q</b>	13.2	2.16	181	281
<b>R</b>	12.1	2.14	260	419
<b>S</b>	20.4	2.80	173	227
<b>T</b>	24.9	5.13	456	312
<b>TH1</b>	18.6	2.11	219	288
<b>TH2</b>	19.8	1.46	307	348

Figure 4.10: The mean value of magnetic field  $B_0$ , the rms magnetic field  $\delta B$ , the Alfvén speed  $v_A$  and the plasma velocity  $v_{ms}$ .

As clearly visible, in all cases the two speeds are of the same order.

In order to quantitatively compare the two speeds, Matthaeus and Goldstein, 1982 [80], proposed a test for the validity of the Taylor hypothesis based on the following prescription:

$$\frac{v_{ms}}{v_A} \gg 2\pi \frac{\delta B}{B_0} \quad (4.2)$$

If this condition is satisfied, then the Taylor hypothesis is valid, the fluctuations can be considered “frozen” into the flow, so that the time series at a single point corresponds to the spatial structure of the fluctuations at the integral scale. We have tested our datasets with this strict relation, and we have obtained the set of ratio values given in the table reported in Figure 4.11.

	$v_{ms} / v_A$	$2\pi\delta B/B_0$	$(v_{ms} / v_A)/(2\pi\delta B/B_0)$
<b>A</b>	0.61	0.60	1.02
<b>B</b>	0.58	1.01	0.57
<b>C</b>	0.75	0.74	1.01
<b>D</b>	1.21	0.65	1.86
<b>E</b>	1.11	0.73	1.52
<b>E2</b>	0.75	0.55	1.36
<b>FsetA</b>	0.74	0.52	1.42
<b>FsetB</b>	1.01	0.58	1.74
<b>H</b>	1.00	0.95	1.05
<b>L</b>	0.32	0.88	0.36
<b>M</b>	1.15	0.74	1.55
<b>N</b>	1.19	2.01	0.59
<b>O</b>	0.73	1.71	0.43
<b>P</b>	0.82	1.37	0.60
<b>Q</b>	1.56	1.03	1.51
<b>R</b>	1.61	1.11	1.45
<b>S</b>	1.31	0.86	1.52
<b>T</b>	0.68	1.29	0.53
<b>TH1</b>	1.32	0.71	1.86
<b>TH2</b>	1.13	0.46	2.46

Figure 4.11: Test for the validity of the Taylor hypothesis. In the first and second column the RHS and the LHS of the inequality (4.2) are respectively reported for the different datasets, while in the third column the RHS to LHS ratio is reported.

From the values given in the above Table, it is evident that the argument by Matthaeus and Goldstein, 1982 [80], is not sufficient to validate Taylor's hypothesis in our database. However, several dataset from similar magnetosheath regions were previously analysed using Cluster spacecraft. In those cases, the availability of multi-spacecraft diagnostics allowed to validate the Taylor hypothesis, even in the absence of a super-Alfvénic flow [13].

For this reason, we also use an alternative, phenomenological verification of the Taylor hypothesis, presented by Stawartz *et al.*, 2016 [124], that has been utilized in other magnetospheric studies of turbulence (Chaston *et al.*, 2007 [18], 2012 [19]).

In a recent work, Stawartz *et al.*, 2016 [124], give a different argument to validate the Taylor hypothesis, which is based on the assumption that  $k_{\perp}$  is sufficient larger than  $k_{\parallel}$ . Their argument may be expressed as in the following. We can assume that fluctuations are mainly Alfvénic (at least in the large-scale domain), so that their frequency in the plasma frame can be estimated as  $\omega \sim \mathbf{k} \cdot \mathbf{v}_A = kv_A \cos \theta$ , where  $\theta$  is the angle between  $\mathbf{k}$  and  $\mathbf{B}_0$ . Indicating by  $\phi$  the angle between  $\mathbf{k}$  and  $\mathbf{v}_{ms}$ , the advection term is  $\mathbf{k} \cdot \mathbf{v}_{ms} = kv_{ms} \cos \phi$ . Since  $v_{ms} \sim v_A$ , the advection term dominates over the frequency  $\omega$  (as required by the Taylor hypothesis) if  $\cos \theta \ll \cos \phi$ .

It is well know that in MHD turbulence the energy cascade tends to develop in the directions perpendicular to the mean magnetic field  $\mathbf{B}_0$ , so that perpendicular wavevectors  $k_{\perp}$  dominate over parallel wavevectors  $k_{\parallel}$ . Then, we expect that  $\theta$  is close to  $\pi/2$ . Examining our datasets, we verified that the mean magnetic field  $\mathbf{B}_0$  is mainly oriented in the  $z$  direction, therefore  $\mathbf{k}$  is essentially in the  $xy$  plane. Instead, the plasma bulk velocity  $\mathbf{v}_{ms}$  is in the  $x$

direction, i.e., mainly perpendicular to  $\mathbf{B}_0$ .

In the table in Figure 4.12, we report the angle  $\alpha$  between  $\mathbf{B}_0$  and  $\mathbf{v}_{ms}$ , calculated as

$$\alpha = \arccos\left(\frac{\mathbf{B}_0 \cdot \mathbf{v}_{ms}}{|\mathbf{B}_0| |\mathbf{v}_{ms}|}\right). \quad (4.3)$$

We can see that, in most cases,  $\alpha$  is around  $90^\circ$ . This shows that the condition  $\cos\theta \ll \cos\phi$  is reasonably satisfied in our database, implying that the Taylor hypothesis is satisfied, according to the argument given by Stawartz *et al.*, 2016 [124].

	$\cos\alpha$ (rad)	$\arccos\alpha$ (rad)	$\alpha$ (deg)
<b>A</b>	-0.25	1.82	104.34
<b>B</b>	0.16	1.41	80.83
<b>C</b>	-0.46	2.05	117.32
<b>D</b>	0.37	1.19	68.41
<b>E</b>	-0.16	1.73	99.10
<b>E2</b>	0.49	1.06	60.69
<b>Fseta</b>	0.53	1.01	58.02
<b>Fsetb</b>	0.24	1.33	76.15
<b>H</b>	0.42	1.14	65.20
<b>L</b>	0.3	1.27	72.58
<b>M</b>	-0.05	1.62	92.84
<b>N</b>	0.08	1.49	85.41
<b>O</b>	0.31	1.26	71.98
<b>P</b>	0.43	1.13	64.57
<b>Q</b>	-0.01	1.58	90.80
<b>R</b>	-0.35	1.93	110.54
<b>S</b>	-0.17	1.74	99.84
<b>T</b>	0.56	0.98	55.97

Figure 4.12: Values obtained by calculating the scalar product between magnetic field  $\mathbf{B}_0$  and the plasma velocity  $\mathbf{v}_{ms}$ . In the first column the value of cosine is shown; in the second and third column the arccosine and the angle between the fields are reported.

The above considerations encourage us to re-interpret the frequency dependence measured by the spacecraft as an information on the spatial dependence in the plasma reference frame.

In order to characterize the properties of the fluctuations, any event was analyzed against the same standard diagnostics for intermittent turbulence, used to test our synthetic model described in previous chapter. In the following, we describe all the observed features.

## 4.1 Autocorrelation function

Figure 4.13 shows examples of the autocorrelation function versus time scale, for two different samples of the whole collection, one chosen among the mixed status (E2) and the other one among the weakly-mixed status (O). The behaviour of the autocorrelation functions is standard, and is similar to the one observed for the synthetic model (cf. Figure (3.5)). The values of the correlation scales  $\tau_{corr}$ , obtained for all samples as described in previous chapter, vary between 13 and 147 sec, in agreement with typical values in this region, and are recorded in Appendix A.

## 4.2 Spectrum of magnetic energy

The magnetic energy power spectra provide quick information about the scaling properties of the field fluctuations. Two examples are given in Figure (4.14). Since the Taylor hypothesis could not be rigorously validated in our database, we present the spectral results in terms of frequency rather than wave vectors, as the transformation between the two relying on the bulk speed inverse proportionality may not be valid.

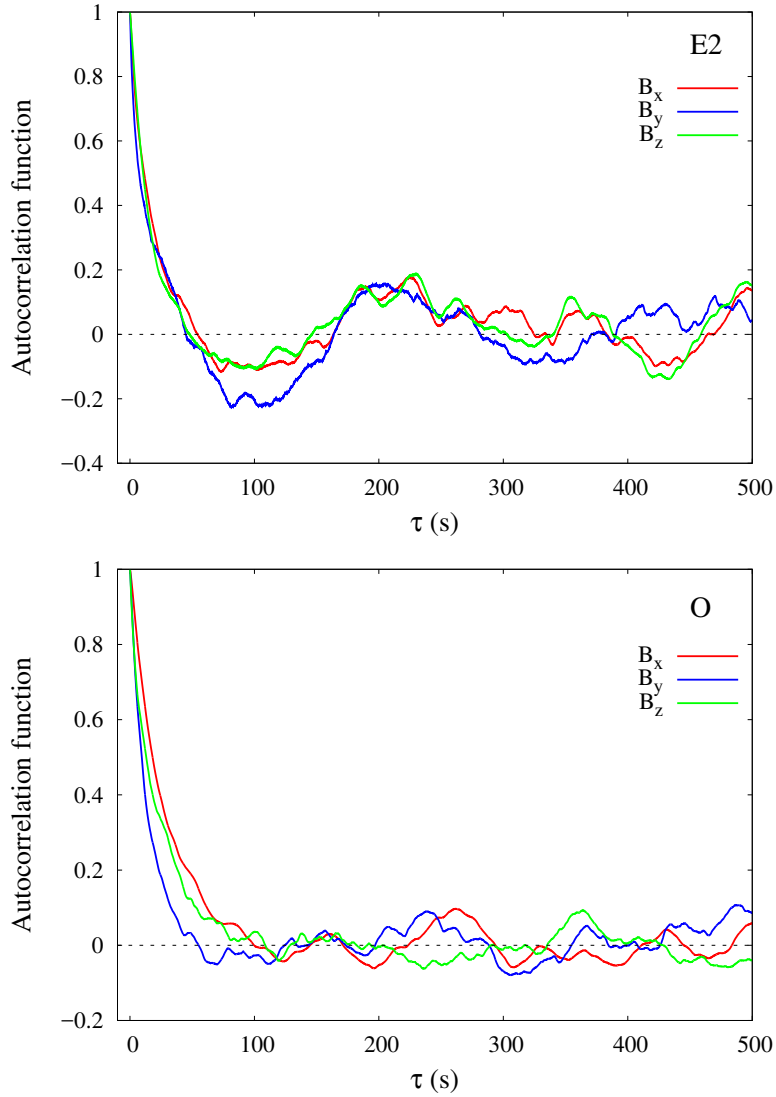


Figure 4.13: The autocorrelation function for three component of magnetic field related to the event E2 in the top panel and the event O at the bottom.

In the Figure (4.14), we show two characteristic frequencies: the frequency related to the correlation time  $f_{corr}$  and the frequency  $f_{d_i}$ , related to the ion inertial length of a thermal ion  $d_i = c/\omega_{pi}$ , i.e. the ratio between light velocity and ion plasma frequency. The latter has been estimated assuming

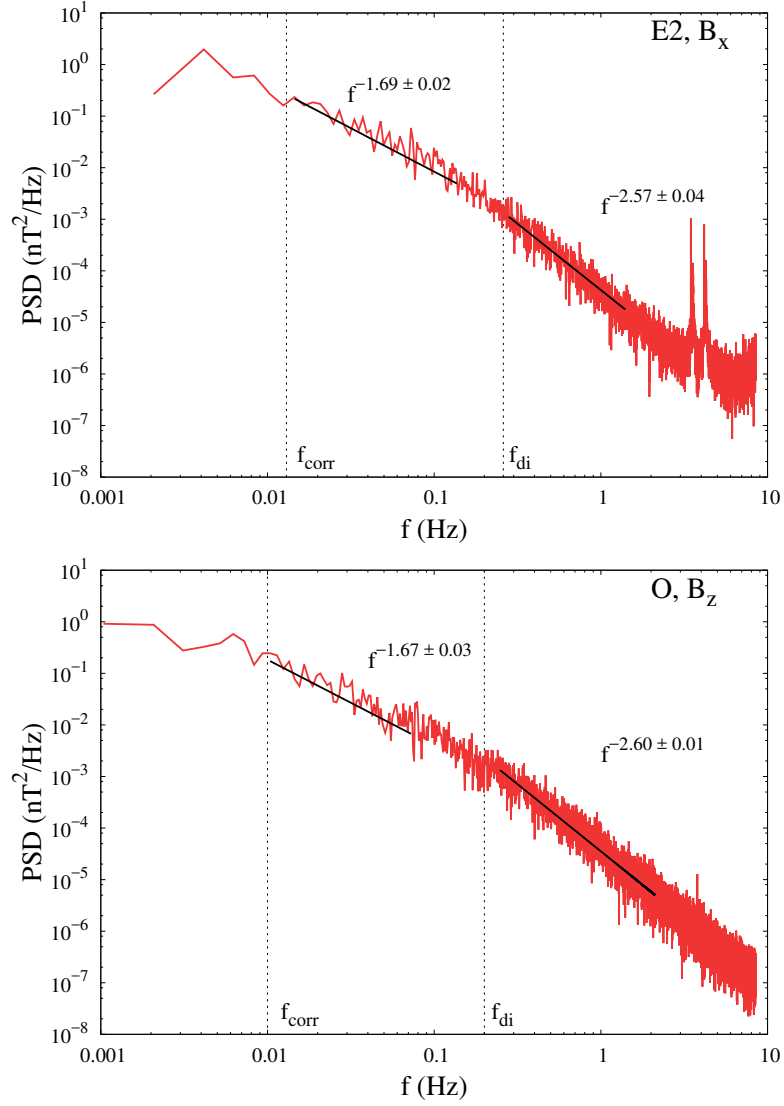


Figure 4.14: The one-dimensional power spectral density (PSD) of the magnetic field  $B_x$  for the dataset E2 (top panel) and  $B_z$  for the dataset O (bottom panel). A Kolmogorov-like spectrum is observed at MHD scale, while a steeper power law is suggested below ion scales. The vertical black dashed lines indicate the frequency  $f_{di}$  related to the ion inertial length  $d_i$ , and the frequency related to the correlation time  $f_{corr}$ .

the validity of the Taylor hypothesis in a broad sense, as in Stawartz *et al.*, 2016 [124].

Specifically, using the Taylor approximation of relation  $\omega_{sc} \simeq \mathbf{k} \cdot \mathbf{v}_{ms}$  and replacing the angular frequency  $\omega$  with the spatial frequency  $f \rightarrow \omega = 2\pi f$  we obtain:

$$2\pi f \simeq kv_{ms}$$

and being the wave vector  $\kappa = 1/\ell$  the inverse of a typical length, in this case  $\ell \sim d_i$ , we have:

$$2\pi f \simeq \frac{v_{ms}}{d_i} \rightarrow f \simeq \frac{v_{ms}}{2\pi d_i} .$$

At large scales, the correlation frequency very well represents the large-scale boundary of the spectral inertial range. Similarly, the inertial range clearly breaks around the frequency associated with the ion inertial scale  $f_{d_i}$ , where kinetic plasma effects start being non-negligible, and in agreement with the usual observations of solar-wind and magnetosheath turbulence (Leamon *et al.*, 1998 [71]). These observations seem to suggest that, although the conditions for the Taylor hypothesis are only phenomenologically met, the transformation from frequency to wave-vector can be safely performed.

In MHD range of scales, i.e. above the ion inertial length, the spectrum is well represented by a power law with exponent  $\sim -1.69$  not far from the Kolmogorov value  $-5/3$ . Below the typical proton scales, the spectrum is compatible with a steeper power law with exponent which we find in the range between  $-1.89$  and  $-2.76$ , with a mean value  $\alpha_{ion} \sim -2.44$ . Similar results were found for the other components of the PSD, collected in Appendix A. The observed spectra seem to indicate that the typical behaviour of space

plasma is retrieved in these samples, and that turbulence might be developing as a consequence of, or superimposed to, the Kelvin-Helmoltz instability. Figure (4.15) shows how the spectral exponent  $\alpha_{kol}$  and the exponent  $\alpha_{ion}$  are distributed around the typical expected values.

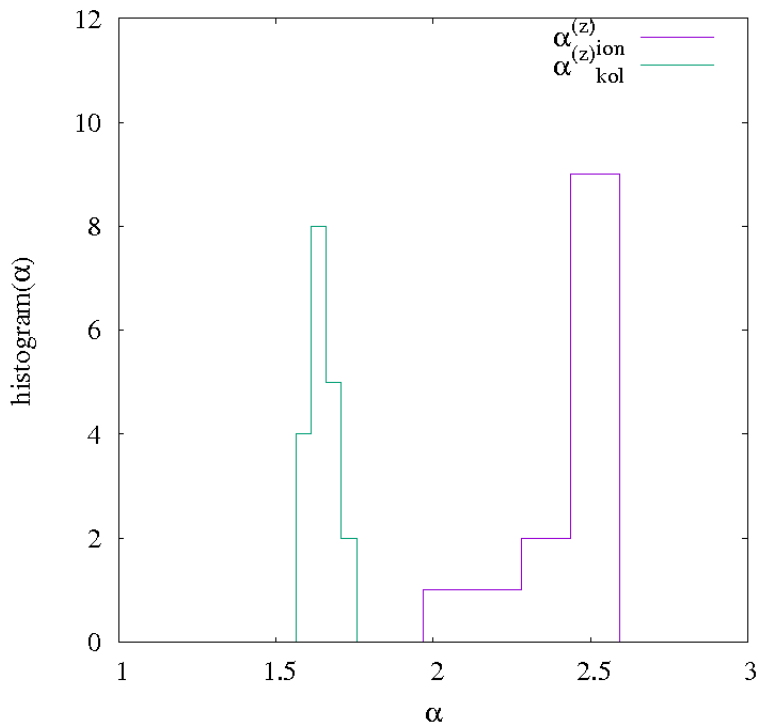


Figure 4.15: Histograms of the total number of events with the spectral exponent  $\alpha_{kol}$ , distributed around the Kolmogorov value  $5/3$  and the exponent  $\alpha_{ion}$ , distributed around the value  $2.44$ .

The histograms show clearly that the inertial range exponent distribution is sharply peaked around the expected Kolmogorov value  $\alpha_{kol} \sim -5/3$ . On the contrary, and in agreement with solar wind observations (Sahraoui *et al.*, 2006 [107]), the small-scale exponents are more broadly distributed around their mean  $\alpha_{ion} \sim /2.44$ .

### 4.3 Probability Distribution Function

As already specified in this thesis, the statistical properties of turbulent fields cannot be fully described by spectra, and the intermittency in particular needs the whole statistics of the fluctuations. For this reason, two examples of the increment PDFs of the  $B_x$  at different scales, are collected in Figure (4.16). For each scale, the magnetic field increments were standardized by normalizing to their standard deviation. The black dashed line represents a reference Gaussian distribution. Similar results were found for the other components. It is worth noting that the probability distribution functions are characterized by high tails and the deviation from Gaussian increases towards smaller scales (Frisch, 1995 [48], Sorriso-Valvo *et al.*, 1999 [120], Bruno and Carbone, 2005 [14]). The fat tails are due to particularly intense magnetic field fluctuations, usually related to the presence of structures.

### 4.4 Kurtosis

A way to quantify the deviation from a Gaussian distribution is the kurtosis, which in our samples has the Gaussian value  $K = 3$  at large scales, roughly down to the correlation scale, and then typically increases toward small scales as a power law  $K(l) \sim l^\kappa$ . For all cases, the power-law fitting range is generally consistent with the spectral inertial range, sometimes with a small shift towards small scales, bounded by the correlation time at large time scales, and by the time associated with the ion-inertial range (via the Taylor hypothesis) at small time scales. The scaling exponent  $\kappa$  gives a quantitative estimate of the intermittency, i.e., of the anomalous scaling of the magnetic fluctuations (Sreenivasan and Annu, 1997 [122]).

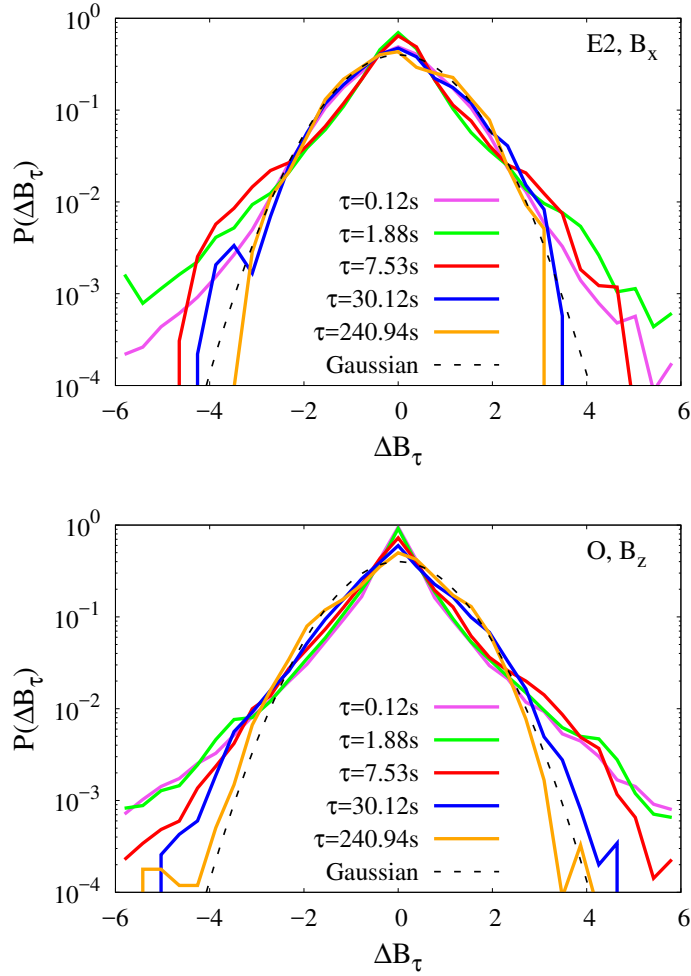


Figure 4.16: Probability distribution functions of the normalized increments  $\Delta B_\tau^{(x)}$  are shown in the top panel for sample E2 and in the bottom panel for sample O. The black dotted line is a Gaussian distribution used as reference.

In Navier-Stokes turbulence, it is often observed that  $\kappa \simeq 0.1$  (Anselmet *et al.*, 1984 [4]). In Figure (4.17), the scaling exponent of kurtosis is larger, consistent with a more efficient intermittency, for both datasets E2 and O. As before, exponents for all samples are collected in the Appendix A.

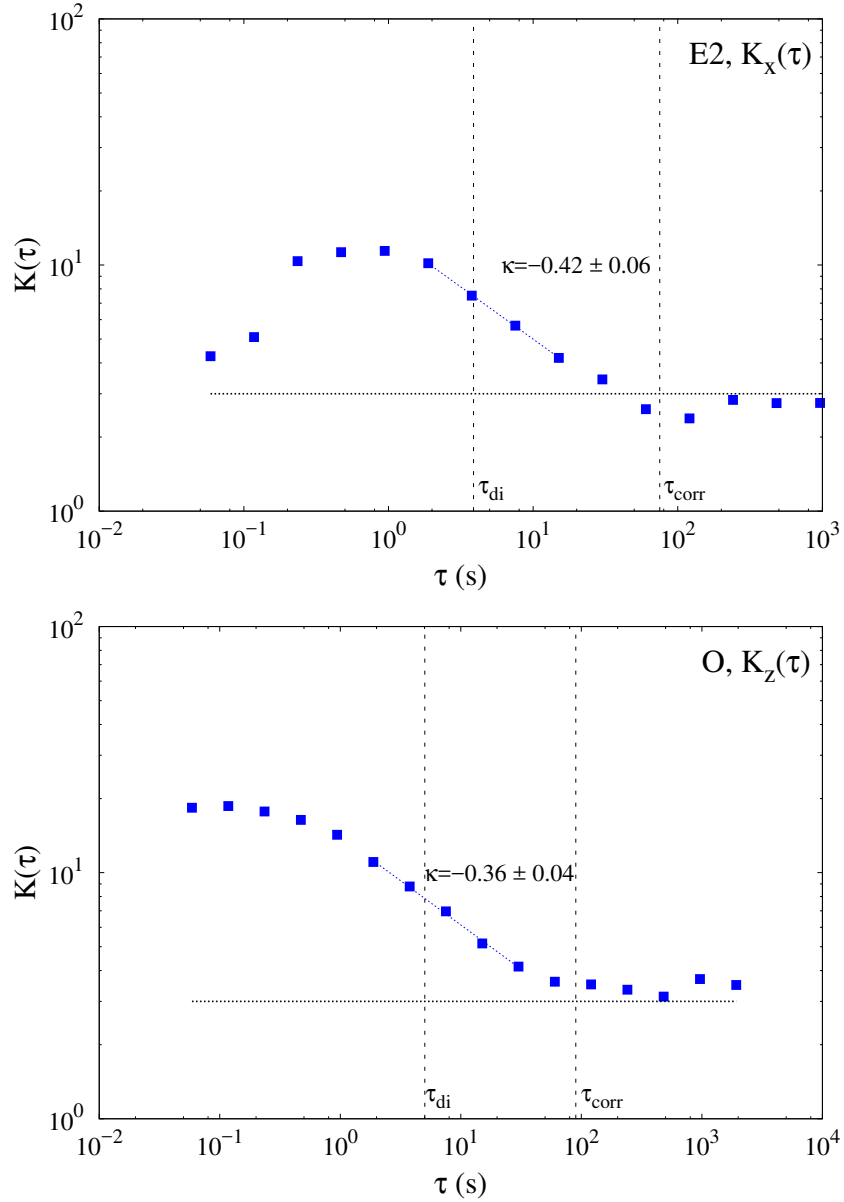


Figure 4.17: The scaling dependence of the kurtosis  $K$  for two sample, E2 at the top and O at the bottom. The Gaussian value  $K = 3$  is indicated, as well as power-law fit in the inertial range for the two cases. The vertical black dashed lines indicate the inertial period  $\tau_{di}$  related to the frequency  $f_{di}$ , and the correlation time  $\tau_{corr}$ .

## 5 Transition to turbulence in the magnetosheath Kelvin-Helmholtz instability

After the analysis of the properties of turbulence in each individual event, we now want to focus on the possibility to highlight the evolution of turbulence along the KH instability by comparing the different samples. In particular, we are interested in understanding if the statistical properties of the field fluctuations depend on the state of the KH vortex roll-up. In order to do so, we will describe the variation of the turbulence and intermittency parameters as the spacecraft explore different locations in the magnetosheath, drifting away from the Sun along the tail-flank magnetopause, where the events are located. In Figure 4.18, the fitted power-law index  $\alpha_{kol}^{(z)}$  of the  $z$  magnetic field component, related to the Kolmogorov range spectrum, is plotted as a function of the  $-X$  coordinate.

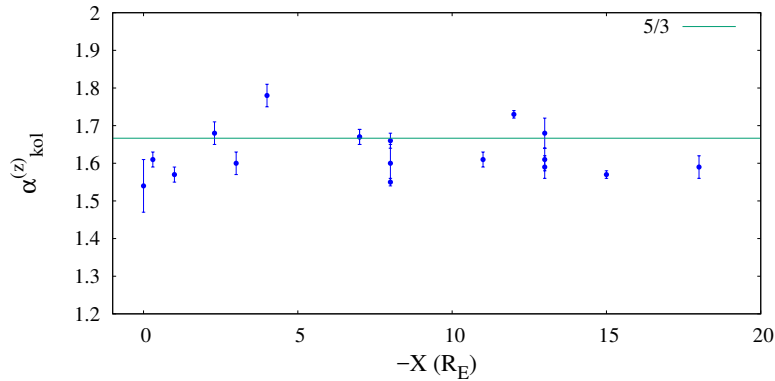


Figure 4.18: The fitted power-law index (component  $z$  of magnetic field), at MHD scales, as a function of  $-X$  coordinate. The value expected for a Kolmogorov-like spectrum is  $-5/3$ , that corresponds to the horizontal green line. A “wavy trend” is observed, during the departure along  $-X$  coordinate, consistently because the error that affect measures are significantly smaller than the  $\alpha$ -index values.

From the figure, it appears that a fluctuating behaviour during the progressive departure along the X coordinate may exist, and is visible as a quasi-periodic modulation of the exponent. The periodicity associated with such oscillation can be estimated by eye to be approximately  $\sim 6 - 7R_E$ . Furthermore, the amplitude of such modulation seems to decrease as the measurements are taken further away from the dusk-dawn line, and a possible saturation may be reached after  $X \sim -15R_E$ . According to the observed period of each set and to the tailward flow speed, the wavelength is estimated to be on average  $\sim 6.4R_E$ , consistent with that reported in literature (Hasegawa *et al.*, 2004 [56], 2006 [55], 2009 [57], Fairfield *et al.*, 2000 [39], Kivelson and Chen, 1995 [64]).

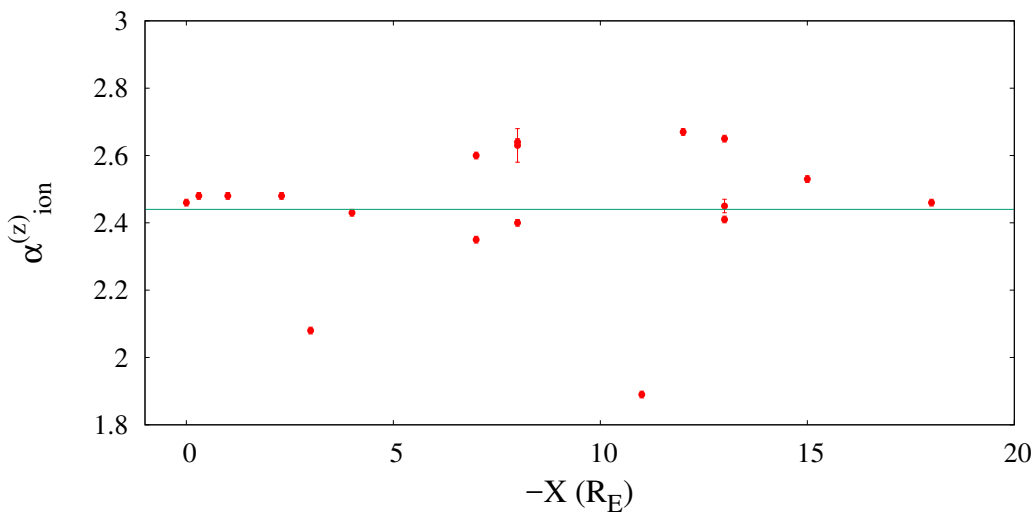


Figure 4.19: The fitted power-law index below ion scale of energy spectra, as a function of  $-X$  coordinate. The reference value is  $-2.44$  (Zimbardo *et al.*, 2010 [140], Sahraoui *et al.*, 2006 [107], Alexandrova *et al.*, 2013 [2])

In the table in Figure 4.20, the values of the fluctuation period, the flow speed  $v_{ms}$  and the wavelength  $\lambda$  for each set, are shown. Our results seem to suggest that, when KHI is observed, the signature of its periodicity is a robust feature of the magnetosheath, and modulates the associated turbulence at all times. Although it is difficult to claim the robustness of this observation with the limited dataset at hand, it is still interesting that the observed modulation seems persistent for most of the parameter obtained in this analysis.

	$v_{ms}$ (km/s)	Fluctuation Period (min)	$\lambda$ ( $R_E$ )
<b>A</b>	332	2-3	7.8
<b>B</b>	183	2-3	4.3
<b>C</b>	257	3	7.3
<b>D</b>	247	3-4	8.1
<b>E</b>	298	2-3	7.0
<b>E2</b>	299	2-3	7.0
<b>FsetA</b>	299	2-3	7.0
<b>FsetB</b>	347	2-3	8.2
<b>H</b>	182	5	8.6
<b>L</b>	92	3	2.6
<b>M</b>	230	2-3	5.4
<b>N</b>	279	2	5.3
<b>O</b>	169	2-3	4.0
<b>P</b>	219	3	6.2
<b>Q</b>	281	2	5.3
<b>R</b>	419	2	7.9
<b>S</b>	227	2-3	5.3
<b>T</b>	312	2-3	7.3
<b>TH1</b>	288	not specified	
<b>TH2</b>	348	not specified	

Figure 4.20: Values of the fluctuation period, the flow speed  $v_{ms}$  and the wavelength  $\lambda$ .

For example, a less evident but similar fluctuation may also be observed for the fitted power-law index in the sub-ion range of scales,  $\alpha_{ion}^{(z)}$ , as also visible in Figure 4.19. The scaling exponent of kurtosis  $\kappa^{(z)}$ , showed in Figure 4.21, also present the same “wavy trend”, just as the figure above described, and in particular with a similar periodicity. This suggest that a kind of signature related to the development of the KH instability waves could be present in the statistical properties of the magnetic turbulence. Note that the power-law index fluctuations are typically larger than the estimate fitting error (as clearly visible from the figures).

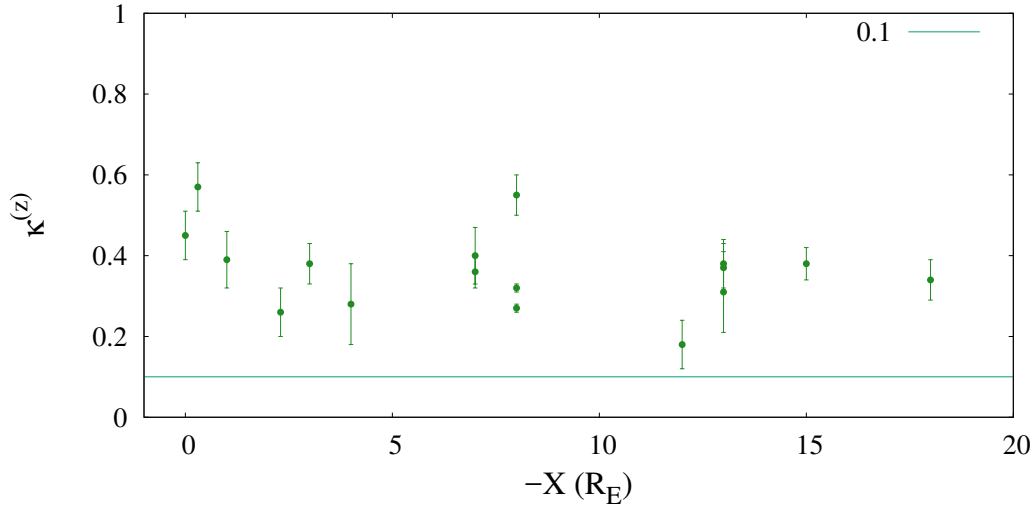


Figure 4.21: The fitted power-law index of the kurtosis, as a function of  $-X$  coordinate. The reference value is  $\kappa = 0.101$ , which is typical value observed in Navier-Stokes turbulence [4].

Finally, the figure of the correlation time  $\tau_{corr}$  as a function of the  $X$  coordinate is given in Figure 4.22. This parameter does not seem to present the same fluctuating behaviour as the other parameters.

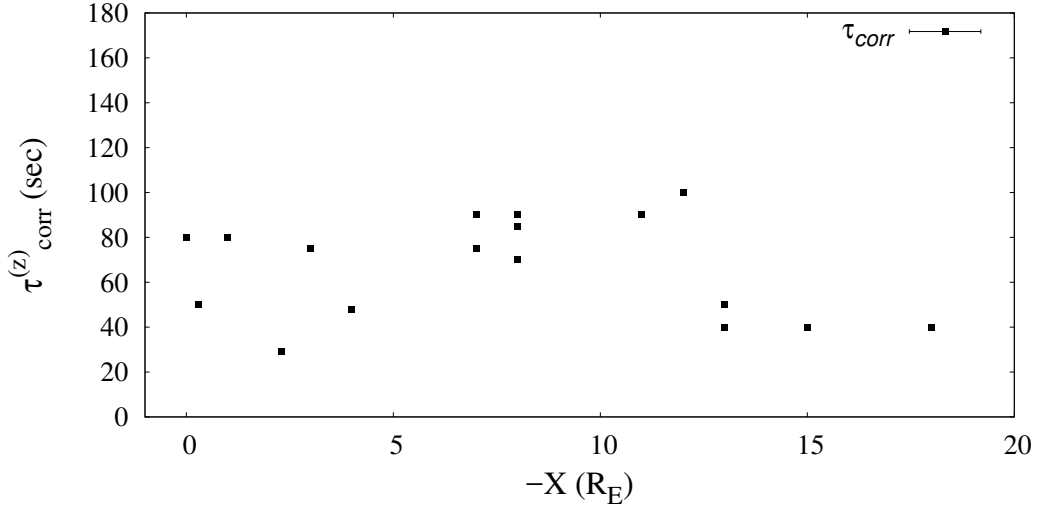


Figure 4.22: The correlation time, relating to  $z$  coordinate of magnetic field, as a function of  $-X$  coordinate.

For a more comprehensive overview of our observation, the fitted power-law indexes  $\alpha_{kol}$ ,  $\alpha_{ion}$  and  $\kappa$  are plotted together as a function of the  $X$  coordinate (Figure 4.23), in order to better visualize the overall behavior which characterizes the KH vortices, as we are describing. In order to have a more global, three-dimensional view, the scaling exponent are also shown together as a function of the  $Y$  coordinate, i.e. the perpendicular coordinate to the Earth's magnetic dipole (Figure 4.24) and of the  $Z$  coordinate, chosen to be in the same sense as the northern magnetic pole (Figure 4.25). The correlation time (bottom panel) for three component of the field, as a function of the coordinate GSM, is also indicated. The spectral index  $\alpha_{kol}$  at MHD scales is indicated by different shades of blue dots for his three components of field; similarly,  $\alpha_{ion}$  is described by red dots for the three component of field and the index  $\kappa$  of the kurtosis is indicated by green dots. We have also

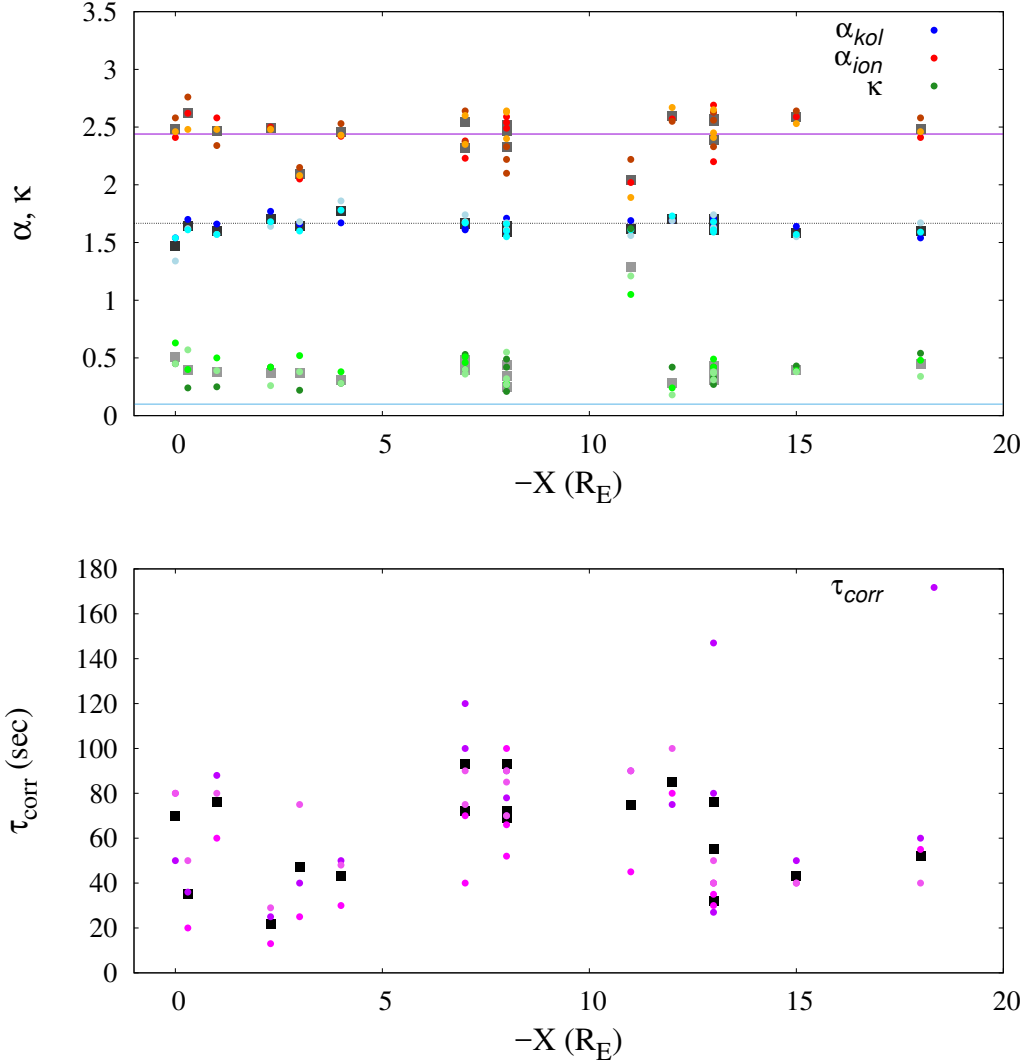


Figure 4.23: Top panel: All fitted power-law index, i.e.  $\alpha_{kolm}$  at MHD scales (blue dots),  $\alpha_{ion}$  at ion scales (red dots) and  $\kappa$  scaling exponent of the kurtosis (green dots), as a function of  $-X$  coordinate. The mean value of each sample is reported as grey square inside the corresponding value of three components of field, of which this value is estimated. The fluctuating behaviour called “wavy trend” is seen for all three indexes. Bottom panel: The autocorrelation time (pink dots) for three component of the field, as a function of  $-X$  coordinate.

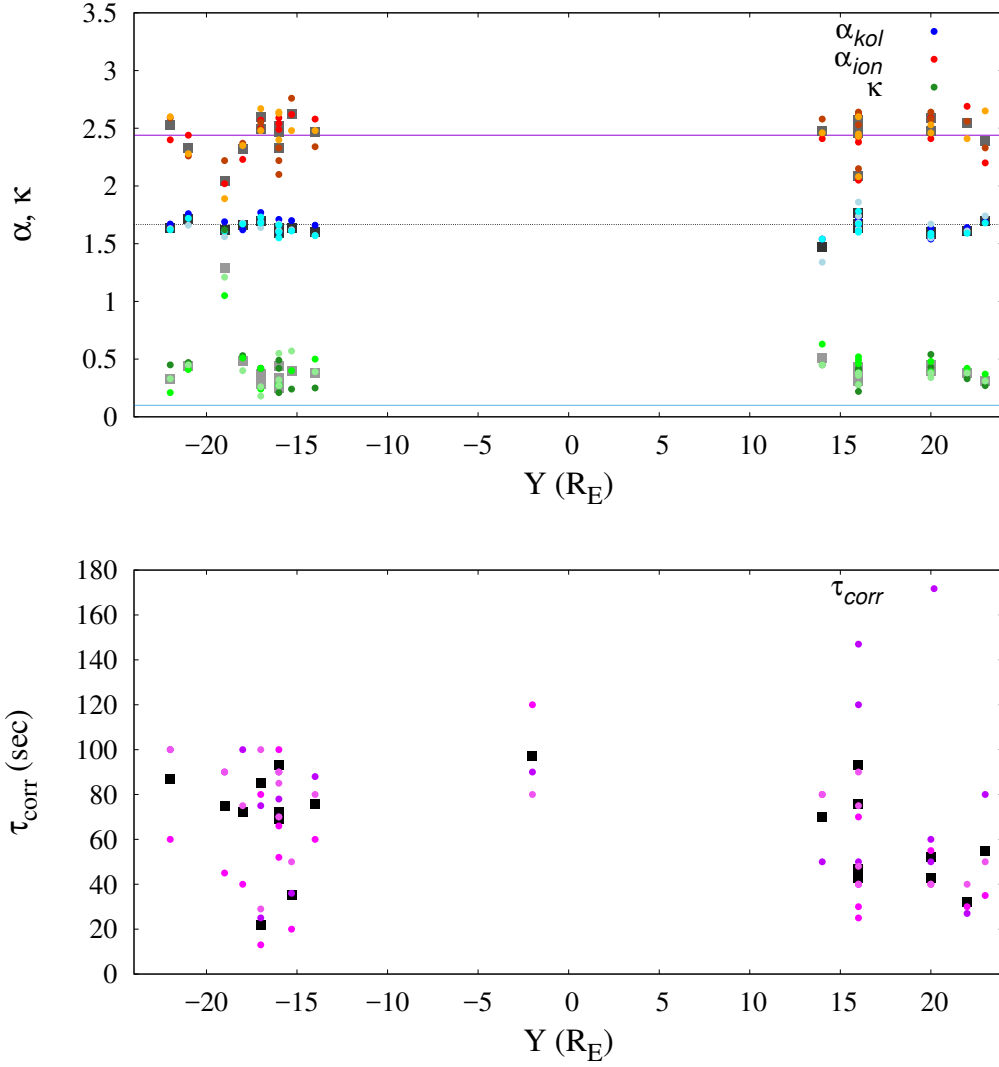


Figure 4.24: All fitted power-law index, i.e.  $\alpha_{kol}$  at MHD scales (blue dots),  $\alpha_{ion}$  at ion scales (red dots) and  $\kappa$  scaling exponent of the kurtosis (green dots), as a function of Y coordinate. The mean value of each sample is reported as grey square inside the corresponding value of three components of field, of which this value is estimated.

Bottom panel: The autocorrelation time (pink dots) for three component of the field, as a function of Y coordinate.

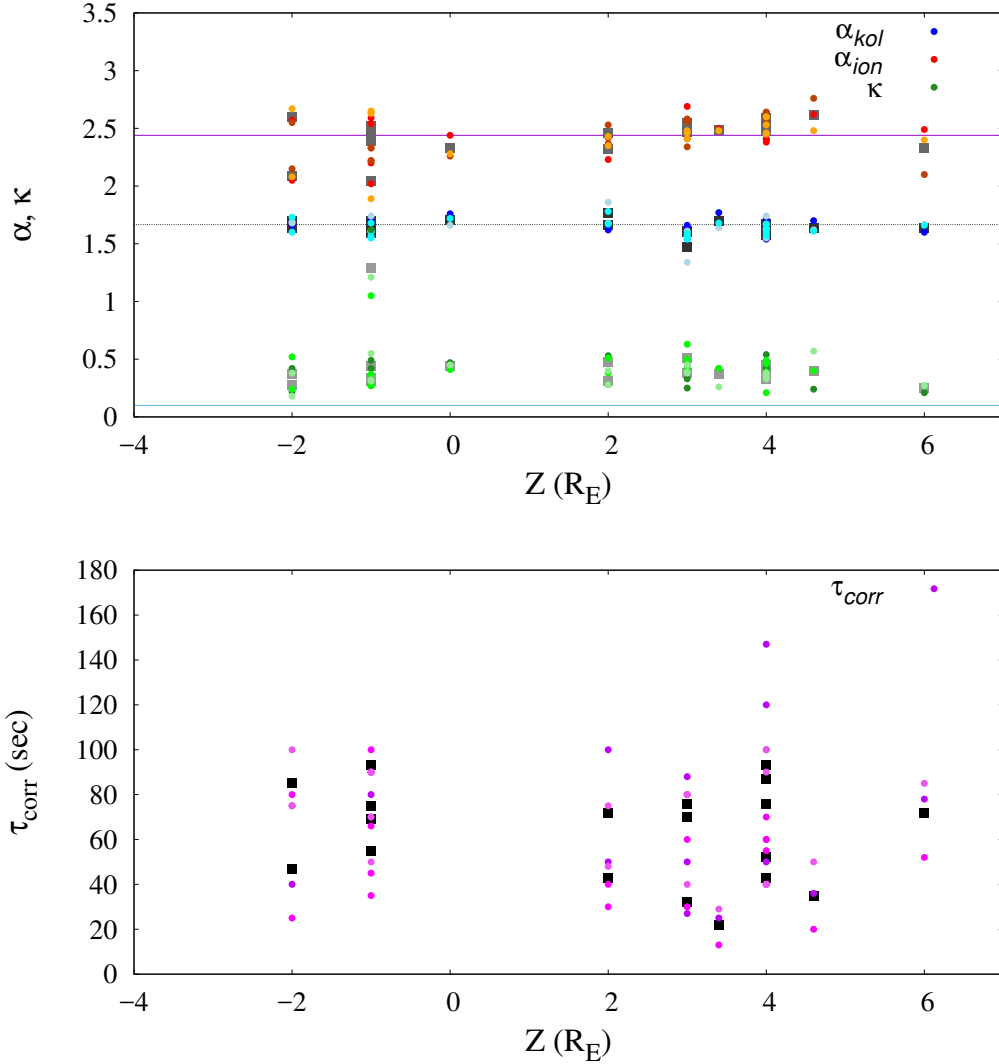


Figure 4.25: All fitted power-law index, i.e.  $\alpha_{kol}$  at MHD scales (blue dots),  $\alpha_{ion}$  at ion scales (red dots) and  $\kappa$  scaling exponent of the kurtosis (green dots), as a function of Z coordinate. The mean value of each sample is reported as grey square inside the corresponding value of three components of field, of which this value is estimated. Bottom panel: The autocorrelation time (pink dots) for three component of the field, as a function of Y coordinate.

reported the mean value of three component of each sample as grey squares. Moreover, reference lines at  $5/3$ ,  $-2.44$  and  $0.101$  are plotted for each exponent, respectively. The fluctuating behaviour we refer to as “wavy trend” is seen for all three indexes, confirming the possible signature of rolled-up vortice that evolves along the coordinates. Noteworthy is the emergence of a clear anti-correlation between the  $\kappa$  and the two spectral indexes, although it is more evident between  $\kappa$  and  $\alpha_{kol}$ .

A more compact view of the dependence of the Y and Z coordinates can be obtained by superposition of the events on the opposite side. This is possible by taking all the events on the same side without any distinctions between dusk and dawnside as in the Figure 4.26. This allows a more evident visualization of the quasi-periodic modulation. In the bottom panel of the same figure, the autocorrelation time is plotted, as a function of Y, although the fluctuating profile does not appear to be completely evident in it. The same presentation was made for the Z coordinate, displayed in Figure 4.27, where the points appear aligned.

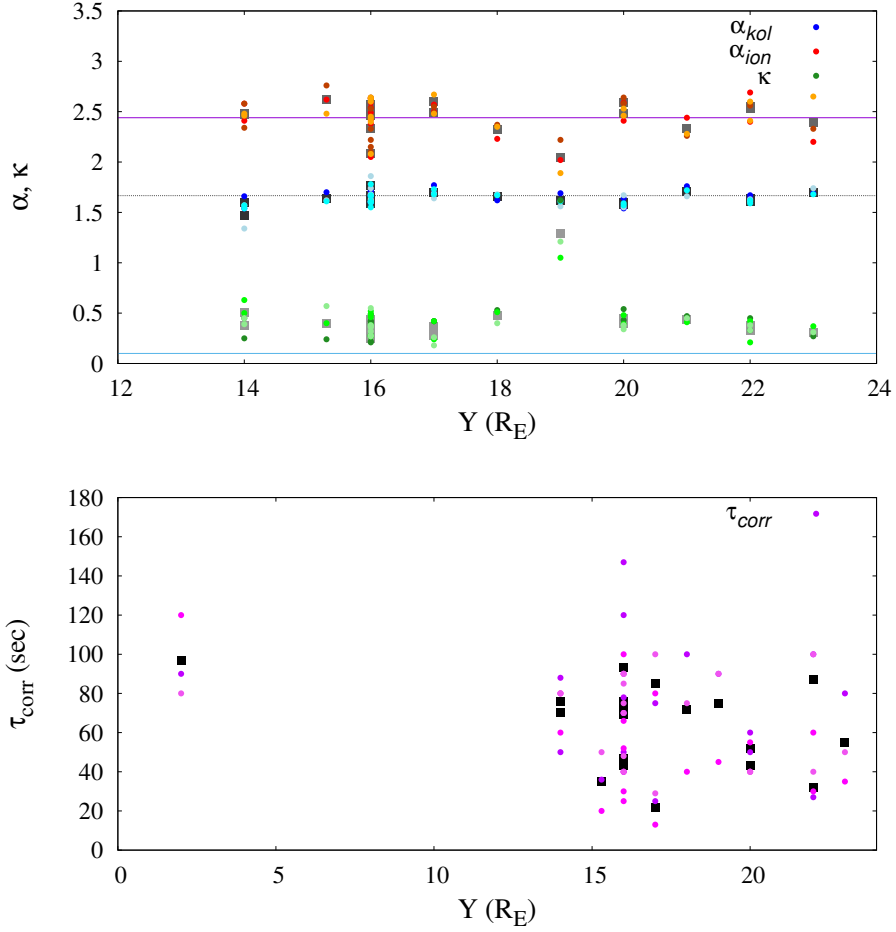


Figure 4.26: All fitted power-law index, i.e.  $\alpha_{kol}$  at MHD scales (blue dots),  $\alpha_{ion}$  at ion scales (red dots) and  $\kappa$  scaling exponent of the kurtosis (green dots), as a function of Y coordinate in absolute value. The mean value of each sample is reported as grey square inside the corresponding value of three components of field, of which this value is estimated. Bottom panel: The autocorrelation time (pink dots) for three component of the field, as a function of Y coordinate in absolute value.

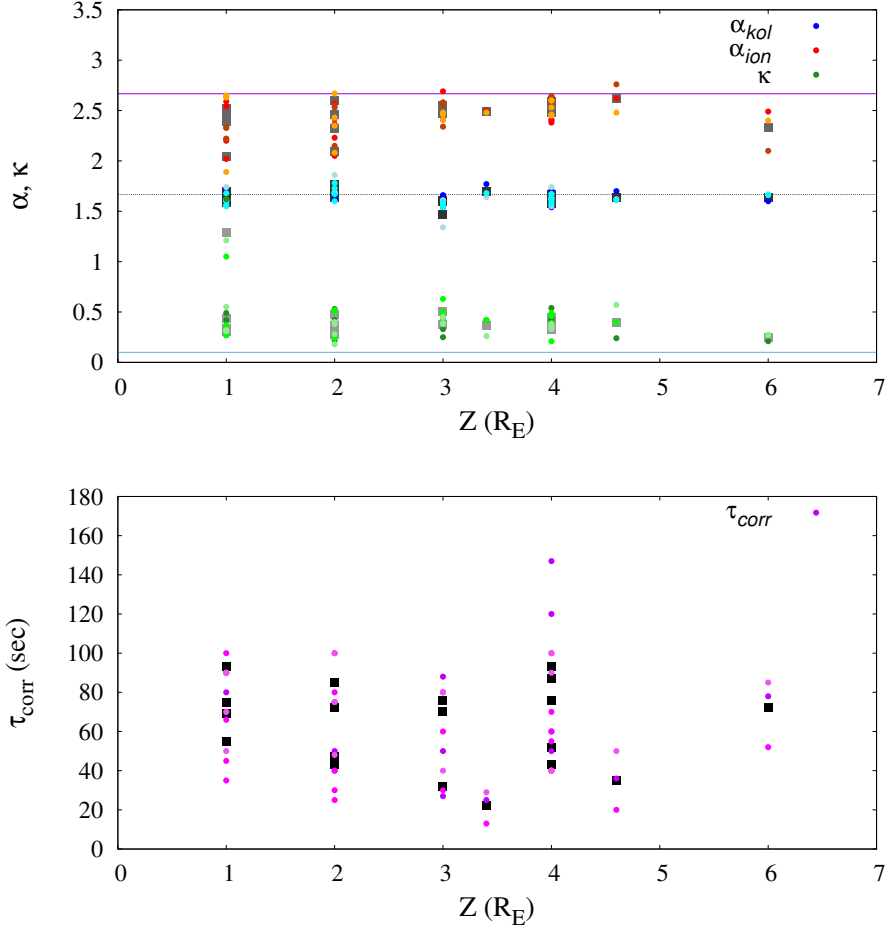


Figure 4.27: All fitted power-law index, i.e.  $\alpha_{kol}$  at MHD scales (blue dots),  $\alpha_{ion}$  at ion scales (red dots) and  $\kappa$  scaling exponent of the kurtosis (green dots), as a function of  $Z$  coordinate in absolute value. The mean value of each sample is reported as grey square inside the corresponding value of three components of field, of which this value is estimated. Bottom panel: The autocorrelation time (pink dots) for three component of the field, as a function of  $Z$  coordinate, in absolute value.

In order to look for correlations between the variations in the turbulence parameters, we directly compare the fluctuations around their means of the two spectral exponents, shown in Figure 4.28 as a function of  $X$  for the  $z$ -component of the field. There is a hint of some correlation in the trend of the two indexes, which is however not very clear.

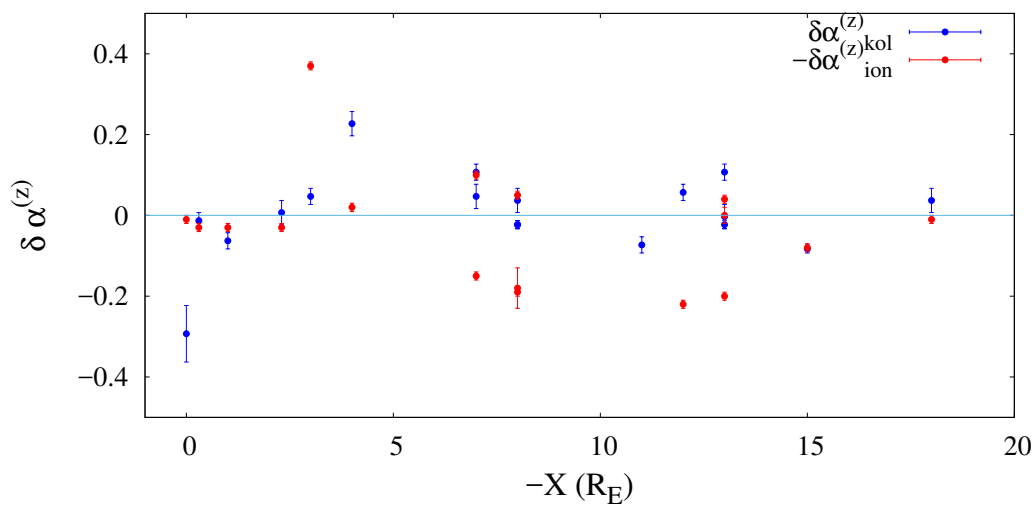


Figure 4.28: Two fitted power-law index for component  $z$  of energy spectra, i.e.  $\alpha_{kol}$  at MHD scales (blue dots) and  $\alpha_{ion}$  at ion scales (red dots) as a function of  $-X$  coordinate.

A similar description was made to highlight possible correlations between the fluctuation of the fitted power-law index for component  $z$  of energy spectra at MHD scales, i.e.  $\alpha_{kol}$  (blue dots) and the fluctuation of the fitted power-law index for component  $z$  of the scaling exponent  $\kappa$  of the Kurtosis (green dots) as a function of  $X$  coordinate, is shown in Figure 4.29. These parameters are reasonably correlated, which is expected, as the intermittency corrections should affect both indexes. The fluctuations of  $\alpha_{ion}$  (blue dots) show some

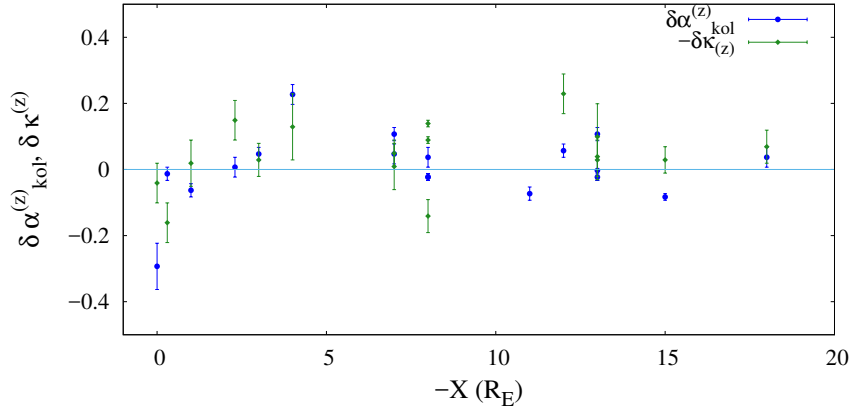


Figure 4.29: The fluctuation of the fitted power-law index for component  $z$  of energy spectra at MHD scales, i.e.  $\alpha_{kolm}$  (blue dots) and the fluctuation of the power-law index for component  $z$  of the scaling exponent  $\kappa$  of the Kurtosis (green dots) as a function of  $-X$  coordinate.

sign of anti-correlation with the scaling exponent  $\kappa$  of the Kurtosis (green dots), again plotted in Figure 4.30, as a function of  $-X$ .

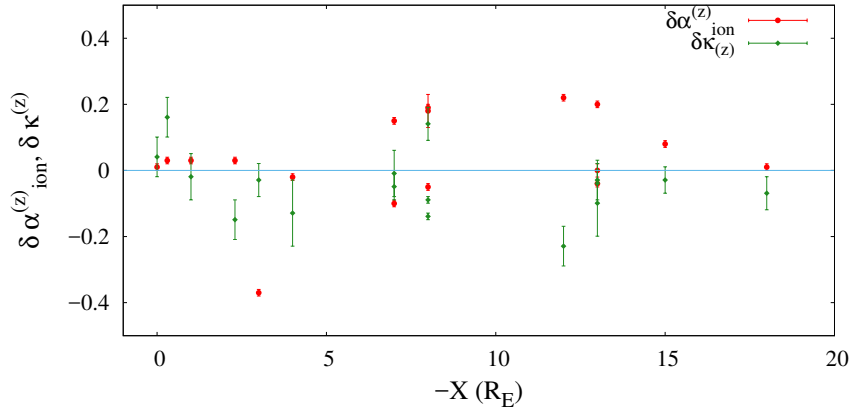


Figure 4.30: The fluctuation of the fitted power-law index for component  $z$  of energy spectra at ion scales, i.e.  $\alpha_{ion}$  (red dots) and the component  $z$  of the fluctuation of the scaling exponent  $\kappa$  of the Kurtosis (green dots) as a function of  $-X$  coordinate.

In order to quantitatively measure the amount of such correlations, we compute the (linear) Pearson and (rank) Spearman correlation coefficients for all pairs of turbulent indexes, listed in table reported in Figure (4.34). Darker green entries indicate moderate correlation, while lighter green shades highlight the pairs with weaker correlations. The black entries show very limited, negligible correlations. For a more visual representation, we show scatter plots for some of the pairs with the highest correlations, i.e.:  $\alpha_{kol}^{(z)}$  vs  $\kappa^{(z)}$  (Figure 4.31),  $\alpha_{ion}^{(z)}$  vs  $\kappa^{(z)}$  (Figure 4.32), and the mean wind speed  $V$  vs  $\kappa$  (Figure 4.33). The presence of correlations, although moderate, could strengthen the observation of the spatial structure along the KH, already visualized above.

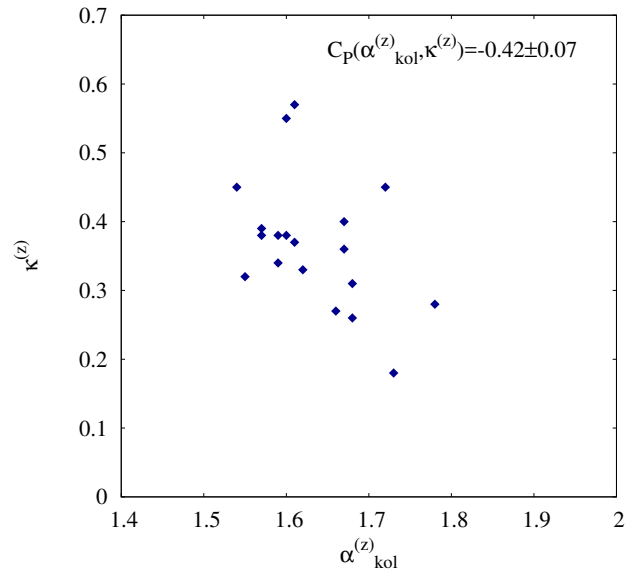


Figure 4.31: The  $z$  component of the scaling exponent  $\alpha_{kol}$  is plotted as a function of the same component of the scaling exponent  $\kappa$ .

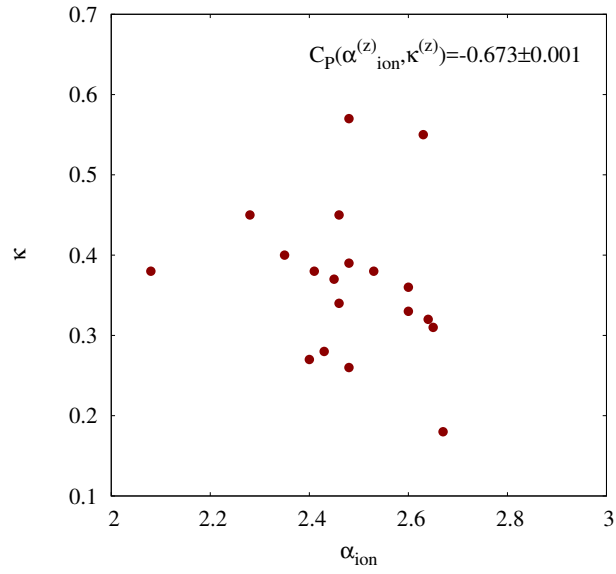


Figure 4.32: The z component of the scaling exponent  $\alpha_{ion}$  is plotted as a function of the same component of the scaling exponent  $\kappa$ .

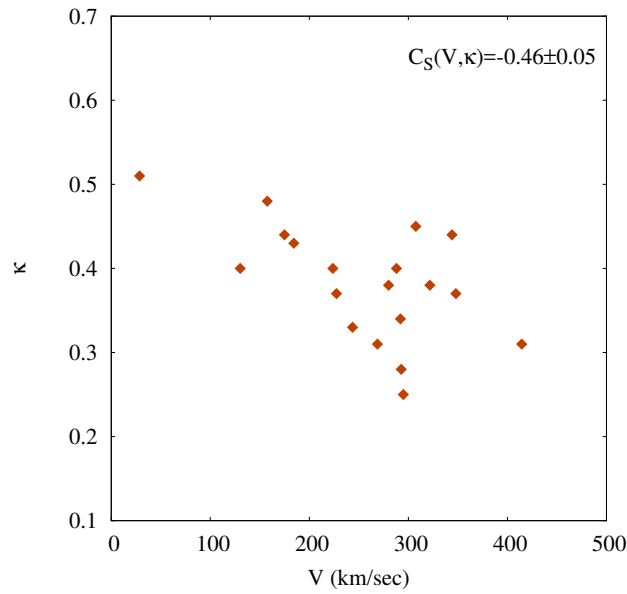


Figure 4.33: The x component of the velocity field is plotted as a function of the same component of the scaling exponent  $\kappa$ .

Correlation	C_Pearson	Prob_Pearson	C_Spearman	Prob_Spearman
ai_k	-0.57	0.01	0.1	0.7
ai_t	-0.1	0.67	-0.15	0.5
aix_kx	-0.47	0.04	-0.2	0.4
aix_tx	-0.09	0.7	-0.28	0.24
aiy_ky	-0.13	0.6	0.003	0.99
aiy_ty	-0.23	0.33	-0.12	0.62
aiz_kz	-0.673	0.001	-0.39	0.09
aiz_tz	-0.06	0.8	0.15	0.5
ak_ai	-0.05	0.8	-0.1	0.7
ak_k	-0.22	0.3	-0.33	0.15
ak_t	-0.06	0.8	0.09	0.7
akx_aix	0.07	0.8	0.23	0.3
akx_kx	0.07	0.8	0.03	0.9
akx_tx	0.007	0.98	-0.03	0.9
aky_aiy	-0.08	0.7	-0.1	0.7
aky_ky	-0.35	0.13	-0.23	0.3
aky_ty	-0.22	0.4	-0.17	0.5
akz_aiz	0.04	0.9	-0.02	0.94
akz_kz	-0.27	0.25	-0.42	0.07
akz_tz	0.01	0.96	0.09	0.7
k_t	0.11	0.6	0.04	0.9
kx_tx	0.21	0.4	0.3	0.2
ky_ty	-0.16	0.5	-0.19	0.4
kz_tz	0.16	0.5	0.001	0.99
v_k	-0.19	0.4	-0.46	0.05
v_kx	-0.13	0.6	-0.25	0.3
v_ky	-0.34	0.15	-0.4	0.06
v_kz	-0.1	0.6	-0.38	0.1
v_t	-0.35	0.1	-0.32	0.2
v_tx	-0.26	0.26	-0.33	0.15
v_ty	-0.32	0.17	-0.21	0.38
v_tz	-0.23	0.2	-0.21	0.38

Figure 4.34: The Pearson and Spearman correlation coefficients for all pairs of turbulent indexes. Darker green entries indicate moderate correlation, while lighter green shades highlight the pairs with weaker correlations. The black entries show very limited, negligible correlations.

## 6 Summary

In this chapter we have studied and characterized the properties of plasma turbulence and intermittency, along the tail-flank magnetopause and its boundary layer, when Kelvin-Helmoltz instability was reported. We have surveyed the Geotail and THEMIS data, recognized as rolled-up vortices by Hasegawa *et al.*, 2006 [55], Fujimoto *et al.*, 1998 [49], Fairfield *et al.*, 2000 [39], 2003 [38], Stenuit *et al.*, 2002 [123] and Lin *et al.*, 2014 [73], taken during satellite magnetopause crossings.

Firstly we have applied time-series analysis techniques to the collection of 20 samples, in order to obtain the autocorrelation function, the power spectrum, the probability distribution functions of the field increments and the kurtosis.

The behaviour of the autocorrelation functions is standard, with values of the correlation scales  $\tau_{corr}$  that vary between 13 and 147 sec, in agreement with typical values in this region.

Since the Taylor hypothesis was validated only phenomenologically in our database, we present the spectral results in terms of frequency rather than wave vectors. In MHD range of scales, the spectrum is well represented by a power law with exponent  $\sim -1.69$  not far from the Kolmogorov value  $-5/3$ . Below the typical proton scales, the spectrum is instead compatible with a steeper power law with exponent which we find in the range between  $-1.89$  and  $-2.76$ , with a mean value  $\alpha_{ion} = -2.44$ . The inertial range clearly breaks around the frequency associated with the ion inertial scale  $f_{di}$ , where kinetic plasma effects start being non-negligible, and in agreement with the

usual observation of solar-wind and magnetosheath turbulence (Leamon *et al.*, 1998 [71]). These observations seem to suggest that the transformation from frequency to wave-vector based on the Taylor hypothesis can be safely performed.

Probability distribution functions are characterized by high tails and the deviation from Gaussian increases towards smaller scales (Frisch, 1995 [48], Sorriso-Valvo *et al.*, 1999 [120], Bruno and Carbone, 2005 [14]). The fat tails are due to particularly intense magnetic field fluctuations, usually related to the presence of structures.

Finally, we have analysed the behaviour of the kurtosis. Its power-law fitting range is generally consistent with the spectral inertial range and the scaling exponent  $\kappa$  gives a quantitative estimate of the intermittency, (Sreenivasan and Annu, 1997 [122]).

In light of the results obtained, then we have investigated the behaviour of several parameters as a function of the progressive departure along the Geocentric Solar Magnetosphere coordinates. It appears that a fluctuating behaviour may exist, and it is visible as a quasi-periodic modulation with an associated periodicity, estimated to be approximately  $6.4 R_E$ . Although the limited dataset at hand makes difficult to claim the robustness of this observation, it is still interesting that the observed modulation seems to persist for most of the parameters considered in this analysis.

In addition, the estimated wavelength is consistent with that reported in literature (Hasegawa *et al.*, 2004 [56], 2006 [55], 2009 [57], Fairfield *et al.*, 2000 [39], Kivelson and Chen, 1995 [64]).

This suggest that a kind of signature, related to the development of the KH instability waves, could be present in the statistical properties of the magnetic turbulence. This may be indicating that, whenever the condition for the onset of the KHI are met in the magnetosheath, the general spatial distribution of the properties of the turbulence generated in the wake of the KH vortices are stable in time.

# Chapter 5

## Conclusions and Perspectives

Turbulence represents an universal phenomenon characterizing the dynamics of different kinds of fluids, both in nature and in laboratory devices. The efficient transfer of energy across scales for which the turbulence is responsible, achieves the connection between the macroscopic flow and the microscopic dissipation of this energy. For this reason, it plays a key role in determining various phenomena so, it is important to provide a representation of turbulence as realistic as possible, including features as intermittency. A natural way to obtain this, is by direct simulations, in which a numerical solution of fluid equations, within a given spatial domain, is calculated starting from suitable initial conditions. In particular, direct simulations of both fluid and MHD equations, are able to reproduce intermittency self-consistently, but with a strong limitation. In fact, they provide a finite space resolution, which determines the extension of the range of spatial scales. This disadvantage can become very severe in 3D configurations, where realistic simulations would require huge computational efforts, as typically happens in astrophysical contexts, where high-Reynolds number fluids are typically involved. A way to address this problem is represented by “synthetic turbulence”, able to

reproduce the main properties of a turbulence field starting from simplified models that mimic the processes taking place in real turbulence. The main advantage of this approach is its reduced computational requirement with respect to direct simulations. This allows to represent, for instance, spatial scale ranges that are larger than in direct simulation, but employing smaller computing resources. This may be useful in astrophysical contexts, like in the solar wind, where in-situ measurements have shown the presence of a turbulence with a spectrum extending over several decades of spatial scales. Models built up over time have been aimed at describing processes that involve very different spatial scales (e.g., particle transport or acceleration, diffusion, and drop formation) (Sardina *et al.*, 2015 [108]); understanding fundamental scaling properties of turbulence (Juneja *et al.*, 1994 [61], Arneodo *et al.*, 1998 [5]); evaluating subgrid stresses (Scotti and Meneveau, 1999 [110], Kerstein *et al.*, 2001 [63], McDermott *et al.*, 2005 [86]) and generating initial conditions for numerical simulations (Rosales and Meneveau, 2006[103]).

We built up a new synthetic turbulence model, presented in a recent paper (Malara *et al.*, 2016 [75]), belonging to the class of “wavelet-based” models, in which the synthetic field is obtained by a superposition of base functions at different spatial scales, whose amplitude is determined so as to reproduce a given spectral law for the turbulent field. Moreover, the model reproduces intermittency in the turbulent field by means of a p-model technique (Meneveau and Sreenivasan, 1987 [87]), in which the spectral energy flux from a given spatial scale to the smaller one is unevenly distributed in space. Our synthetic turbulence model generates a three-component solenoidal time-

independent turbulent field, so it can be used to describe either an incompressible flow or a turbulent magnetic field. Our model shares many aspects with models by Juneja *et al.*, 1994 [61] and by Cametti *et al.*, 1998 [16], but with relevant differences in the algorithm. In fact, one important limitation in the 3D model by Cametti *et al.* [16] is in the memory requirement, which rapidly increases when considering increasing spectral width. The algorithm employed by our model has been designed so as to avoid both large memory employments and long computational times in the evaluation of the turbulent field at a given spatial position. This is the most important feature of the model, because it allows to describe a turbulence with a very extended spectral range using a modest computational effort. The model contains parameters that can be tuned in order to reproduce different physical situations. We also explored the possibility to include an anisotropic spectrum, trying to reproduce the situation described by the so-called “critical balance” principle, postulated by Goldreich & Sridhar, 1995 [51], in the case of a MHD turbulence, often advocated for the description of solar wind turbulence. In order to assess the validity of the model and its reliability in reproducing realistic flows, we have run the standard diagnostics for intermittent turbulence and verified that the synthetic field indeed possesses the characteristics that were chosen as input. To this aim, we have obtained a series of isotropic runs by fixing the scaling exponent  $h$ , which contributes to determine the index of the power-law spectrum, and varying the intermittency parameter  $p$ , which sets the “level” of intermittency. We have worked with three values:  $p = 0.5$  (no intermittency),  $p = 0.7$  (standard Navier-Stokes intermittency),  $p = 0.9$  (strong intermittency). We have then extracted synthetic

one-dimensional cuts within the model domain, and have applied time-series analysis techniques: autocorrelation function, power spectrum, probability distribution functions of the field increments, their structure functions, the kurtosis, and a standard multifractal analysis. All the tests gave satisfactory results, showing that the synthetic data reproduce well the required conditions of spectral scaling and intermittency. A small anisotropy originated by the particular shape of the eddy functions is present along the three axes of the system. This was easily mediated by choosing trajectories with an angle with the three axes. We have also explored the geometry of the system by using two anisotropic runs, with  $p = 0.5$  and  $p = 0.7$ , and by imposing the critical balance conditions. Even in the anisotropic case, the output satisfactorily reproduces the expected values of spectral slope and intermittency for all the observables. We can conclude that the model provides a good representation of intermittent turbulence, and is sensitive to the choice of the input parameters, which allows to fine tune the type of turbulence as desired. We wish to note that a preliminary version of the present model has been recently employed to study the problem of energetic particle diffusion in a magnetic turbulence (Pucci *et al.*, 2016 [99]). The highly suprathermal speed of the energetic test particles, as observed, for example, in the solar wind, allowed for the use of the static turbulent field generated by our model. That investigation has singled out relevant effects on the particle transport related to both large spectral extensions and to intermittency. Thus, a representation of a 3D turbulence with a wide spectrum, as well as a tunable level of intermittency, have been crucial aspects of employing the present synthetic turbulence model in this study. Furthermore, when using our model to run

test-particle simulations the integration of particle trajectories is considerably simplified by the possibility to calculate the turbulent field directly at any spatial position, thus avoiding interpolations on a spatial grid (Benzi *et al.*, 1984 [10], Meneveau and Sreenivasan, 1987 [87]). Another possible application of our model is related to the problem of cosmic ray diffusion in the Galaxy, where a magnetic turbulence with a very wide spectrum is postulated. Another problem which we are planning to work on is the so-called “diffusive shock acceleration”, in which particle acceleration by means of shocks propagating in a turbulent medium is considered. Of course, our synthetic turbulence model has several limitations which are worth discussing. First, it is important to acknowledge that the present version of our model is not able to reproduce the skewness of the field increments PDFs which is universally observed in fully developed turbulence. Indeed, due to the symmetry of the adopted base functions, all third-order moments are essentially vanishing. An improved version of the model that accounts for the appropriate description of the skewness is currently in progress. Another limitation of the model is represented by the lack of time dependence. For instance, this aspect could be important in the case that the model is employed to study transport in turbulent magnetic fields of particles whose typical velocity is of the order of the fluctuation propagation speed (e.g., the Alfvén speed). In particular, this happens for thermal particles in situations when the value of the plasma  $\beta$  is of the order of unity. For this reason, it would be desirable to include a form of time dependence in our model, similar, for instance, as in the model by Lepreti *et al.*, 2006 [72]. We are also working on this subject. Finally, we mention the fact that in real fluids, structures at small

scales often display a certain degree of spatial organization; we are referring to vorticity filaments observed in ordinary fluids, or to quasi-two dimensional current sheets in magnetofluids. Such structures would require a high degree of spatial coherence in order to be reproduced by our model, which is lacking at present.

The second part of this thesis has focused on one key issue: the turbulence at the interface between the solar wind and the Earth's magnetosphere, mediated by the magnetopause. Connections between Sun and Earth have been investigated all along in space plasma physics, with the aim of understanding how solar wind interacts with the Earth's magnetosphere.

We have described this region, which is characterized by strong gradients of density and magnetic field, where the Kelvin-Helmholtz instability (KH) can drive waves at the magnetopause. These waves can grow to form rolled-up vortices and facilitate transfer of plasma into the magnetosphere. This mechanism is considered one of the most important responsible for populating the low latitude boundary layer (LLBL) during periods of northward interplanetary magnetic field. It is very important to be able to determine the properties of plasma turbulence and intermittency inside magnetosheath, given the great interest in the mechanisms associated with the KH instability and the terrestrial magnetosphere. Properties of turbulence can help to understand how the particle transport from the solar wind to the magnetosphere works, and more generally, what are the mechanisms of interaction between these two regions of the near-Earth space. Moreover, it is interesting to study the evolution of turbulence, as a result of the development of KH

instability as it moves away from the Sun along the tail-flank magnetopause. By using data taken during satellites magnetopause crossings, from Themis and Geotail missions, we have collected a big enough dataset classified as KH events by Hasegawa *et al.*, 2006 [55], Fujimoto *et al.*, 1998 [49], Fairfield *et al.*, 2000 [39], 2003 [38], Stenuit *et al.*, 2002 [123] and Lin *et al.*, 2014 [73]. Events are encountered along the flank magnetopause, most of which are behind the dawn-dusk terminator, showing quasi-periodic plasma and field fluctuations associated with KH waves. Our goal has been characterizing the intermittent turbulence that takes place inside such waves. To do this, we have employed the analysis tools already used to assess the validity of the synthetic turbulence model and its reliability in reproducing realistic flows (i.e. the spectral analysis and the scale-dependent statistics of the field increments), also for the analysis of space plasma data. For each dataset, we have obtained: the autocorrelation function associated to the correlation scale of the field; the associated energy power spectrum, whose power-law scaling exponent has to be compared with Kolmogorov-like spectrum observed at MHD scales, while a steeper power law is suggested below proton scales; the Probability Distribution Functions (PDFs) of the scale-dependent increments, whose deviation from a Gaussian qualitatively illustrates the presence of intermittency; finally the kurtosis with its scaling exponent, a quantitative measure of intermittency.

From our results, it appears that a fluctuating behaviour during the progressive departure along the Geocentric Solar Magnetosphere coordinate system may exist, and it is visible as a quasi-periodic modulation of the various exponents. The periodicity associated with such oscillation was estimated

to be approximately  $6.4 R_E$ . Furthermore, the amplitude of such modulation seems to decrease as the measurements are taken further away from the Earth, and a possible saturation may be reached after  $\sim 15R_E$ . Although the limited dataset at hand makes difficult to claim the robustness of this observation, it is still interesting that the observed modulation seems to persist for most of the parameters considered in this analysis. This suggest that a kind of signature related to the development of the KH instability waves could be present in the statistical properties of the magnetic turbulence, even though the different samples used for this study were taken at largely different times. This may be indicating that, whenever the condition for the onset of the KHI are met in the magnetosheath, the general spatial distribution of the properties of the turbulence generated in the wake of the KH vortices are stable in time.

A future development is certainly the possibility to enrich the collection of events combining multispacecraft measurements of MMS mission, in particular considering the much better resolution of particle measurements onboard MMS compared to Geotail. In fact, over three months in 2017, the MMS spacecraft will pass from the dayside magnetopause, to a new, larger orbit on the nightside. Such measurements are crucial to obtain accurate profiles of field across the magnetopause and datasets much larger than the ones used in the present analysis. The perspective is to have a complete and quantitative characterization of turbulence and associated intermittence in this region, which is still poorly studied.

# Appendix A - Data Analysis Collection

All parameters calculated from the data analysis, are collected below. Each set of data was summed up in four tables. The first table shows the informations (taken by Hasegawa *et al.*, 2006 [55]), about the date, the time interval, the GSM position measured in  $R_E$ , the IMF condition, where the symbol NBZ means northward IMF, the ion mixing status and the fluctuation period, related to the rolled-up vortices events, already described in chapter 4, section 4, and here again reported for completeness. The ion mixing status consists of two definitions: the “mixed” status means that a significant amount of cool magnetosheath-like ions, was present on the magnetospheric side of the magnetopause, where density  $n > 1/cm^3$ , while “weakly-mixed” means that magnetosheath-like ions were found on magnetospheric side, but their density was lower than  $n < 1/cm^3$ . The fluctuation period instead, corresponds to the perturbations in the flow that are interpreted by Hasegawa *et al.*, 2006 [55] as being due to vortical motions of plasma (e.g., Fujimoto *et al.*, 2003 [50]), whereas those in the field are due to deformation of the field lines when those near the magnetopause are brought into rolled-up vortices (Hasegawa *et al.*, 2004 [58]; Takagi *et al.*, 2006 [127]).

In the second table we have collected in order: the correlation time  $\tau_{corr}^{(i)}$ ; the mean value of the correlation time  $\langle \tau_{corr}^{(i)} \rangle$  with the associated rms value; the frequency  $f_{corr}^{(i)}$  related to the correlation time, where  $f_{corr}^{(i)} = 1/\tau_{corr}^{(i)}$  and the index  $i = x, y, z$  represents the corresponding component; the ion inertial length  $d_i = c/\omega_{pi}$ , i.e. the ratio between light velocity and ion plasma frequency; the frequency  $f_{d_i}^{(i)}$  (see section 4.2, chapter 4) and its corresponding time  $\tau_{d_i}$ .

In the third table there are the scaling exponents of the power spectral density of magnetic field at MHD scales  $\alpha_{kol}^{(i)}$ , the mean value  $\langle \alpha_{kol}^{(i)} \rangle$  with the associated rms value, the spectral index at the ion scales  $\alpha_{ion}^{(i)}$  and the mean value  $\langle \alpha_{ion}^{(i)} \rangle$  with the rms value.

The fourth table present the scaling exponent  $\kappa^{(i)}$  of the kurtosis, the mean value  $\langle \kappa^{(i)} \rangle$  and the rms value. In addition, below each index, a description of the kurtosis behavior at the ion scale is given.

### Geotail - dataset A

Date	Time Interval	GSM Position (RE)	IMF Condition	Ion Mixing Status	Fluctuation Period
2002-10-15	2100-2300 UT	(-1,-14, 3)	Extended NBZ	Mixed	2-3 min

$\tau_{\text{corr}}^{(i)} \text{ (s)}$			$\langle \tau_{\text{corr}}^{(i)} \rangle_i \pm \tau_{\text{rms}}^{(i)} \text{ (s)}$	$f_{\text{corr}}^{(i)} \text{ (Hz)}$			$d_i \text{ (Km)}$	$f_{di} \text{ (Hz)}$	$\tau_{di} \text{ (s)}$
88.0 ± 0.2	60 ± 0.2	80 ± 0.2	76 ± 12	0.01	0.02	0.01	137.03	0.39	2.59

$\alpha_{\text{kol}}^{(i)}$			$\langle \alpha_{\text{kol}}^{(i)} \rangle_i \pm \alpha_{\text{rms}}^{(i)}$	$\alpha_{\text{ion}}^{(i)}$			$\langle \alpha_{\text{ion}}^{(i)} \rangle_i \pm \alpha_{\text{rms}}^{(i)}$
-1.66 ± 0.03	-1.57 ± 0.02	-1.57 ± 0.02	1.60 ± 0.04	-2.58 ± 0.01	-2.34 ± 0.01	-2.48 ± 0.01	2.47 ± 0.10

$\kappa^{(i)}$			$\langle \kappa^{(i)} \rangle_i \pm \kappa_{\text{rms}}^{(i)}$
-0.25 ± 0.06	-0.50 ± 0.06	-0.39 ± 0.07	0.38 ± 0.10
saturation	saturation	saturation	

### Geotail – dataset B

Date	Time Interval	GSM Position (RE)	IMF Condition	Ion Mixing Status	Fluctuation Period
2001-11-16	1900-2000 UT	(-7,-18, 2)	Extended NBZ (often not dominant)	Weakly Mixed	2-3 min

$\tau_{\text{corr}}^{(i)} \text{ (s)}$			$\langle \tau_{\text{corr}}^{(i)} \rangle_i \pm \tau_{\text{rms}}^{(i)} \text{ (s)}$	$f_{\text{corr}}^{(i)} \text{ (Hz)}$			$d_i \text{ (Km)}$	$f_{di} \text{ (Hz)}$	$\tau_{di} \text{ (s)}$
100.0 ± 0.2	40 ± 0.2	75 ± 0.2	72 ± 25	0.01	0.02	0.01	163.11	0.18	5.59

$\alpha_{\text{kol}}^{(i)}$			$\langle \alpha_{\text{kol}}^{(i)} \rangle_i \pm \alpha_{\text{rms}}^{(i)}$	$\alpha_{\text{ion}}^{(i)}$			$\langle \alpha_{\text{ion}}^{(i)} \rangle_i \pm \alpha_{\text{rms}}^{(i)}$
-1.62 ± 0.03	-1.68 ± 0.03	-1.67 ± 0.02	1.66 ± 0.03	-2.23 ± 0.01	-2.37 ± 0.01	-2.35 ± 0.01	2.32 ± 0.06

$\kappa^{(i)}$			$\langle \kappa^{(i)} \rangle_i \pm \kappa_{\text{rms}}^{(i)}$
-0.53 ± 0.10	0.52 ± 0.10	-0.40 ± 0.07	0.48 ± 0.06
saturation and decrease	saturation and decrease	saturation and decrease	

### Geotail – dataset C

Date	Time Interval	GSM Position (RE)	IMF Condition	Ion Mixing Status	Fluctuation Period
2001-12-07	2000-2130 UT	(-11,-19,-1)	Strong NBZ after N-turning	Weakly Mixed	~3 min

$\tau^{(i)}_{\text{corr}} \text{ (s)}$			$\langle \tau^{(i)}_{\text{corr}} \rangle_i \pm \tau^{(i)}_{\text{rms}} \text{ (s)}$	$f^{(i)}_{\text{corr}} \text{ (Hz)}$			$d_i \text{ (Km)}$	$f_{di} \text{ (Hz)}$	$\tau_{di} \text{ (s)}$
90.0 ± 0.2	45 ± 0.2	90 ± 0.2	75 ± 21	0.01	0.02	0.01	183.94	0.22	4.49

$\alpha^{(i)}_{\text{kol}}$			$\langle \alpha^{(i)}_{\text{kol}} \rangle_i \pm \alpha^{(i)}_{\text{rms}}$	$\alpha^{(i)}_{\text{ion}}$			$\langle \alpha^{(i)}_{\text{ion}} \rangle_i \pm \alpha^{(i)}_{\text{rms}}$
-1.69 ± 0.02	-1.56 ± 0.02	-1.61 ± 0.02	1.62 ± 0.05	-2.02 ± 0.02	-2.22 ± 0.01	-1.89 ± 0.01	2.04 ± 0.13

$\kappa^{(i)}$			$\langle \kappa^{(i)} \rangle_i \pm \kappa^{(i)}_{\text{rms}}$
-1.62 ± 0.07	1.05 ± 0.07	-1.21 ± 0.07	1.29 ± 0.24
increase and saturation	increase and saturation	increase and saturation	

### Geotail – dataset D

Date	Time Interval	GSM Position (RE)	IMF Condition	Ion Mixing Status	Fluctuation Period
1998-12-27	1800-2100 UT	(-21,-22,-4)	Extended strong NBZ	Mixed	3-4 min

$\tau^{(i)}_{\text{corr}} \text{ (s)}$			$\langle \tau^{(i)}_{\text{corr}} \rangle_i \pm \tau^{(i)}_{\text{rms}} \text{ (s)}$	$f^{(i)}_{\text{corr}} \text{ (Hz)}$			$d_i \text{ (Km)}$	$f_{di} \text{ (Hz)}$	$\tau_{di} \text{ (s)}$
100 ± 0.2	60 ± 0.2	100 ± 0.2	87 ± 19	0.01	0.02	0.01	170.44	0.23	4.34

$\alpha^{(i)}_{\text{kol}}$			$\langle \alpha^{(i)}_{\text{kol}} \rangle_i \pm \alpha^{(i)}_{\text{rms}}$	$\alpha^{(i)}_{\text{ion}}$			$\langle \alpha^{(i)}_{\text{ion}} \rangle_i \pm \alpha^{(i)}_{\text{rms}}$
-1.67 ± 0.02	-1.63 ± 0.02	-1.62 ± 0.02	1.64 ± 0.02	-2.40 ± 0.01	-2.59 ± 0.01	-2.60 ± 0.01	2.53 ± 0.09

$\kappa^{(i)}$			$\langle \kappa^{(i)} \rangle_i \pm \kappa^{(i)}_{\text{rms}}$
-0.45 ± 0.06	-0.21 ± 0.04	-0.33 ± 0.04	0.33 ± 0.10
saturation and increase	saturation	saturation	

## Geotail – dataset E

Date	Time Interval	GSM Position (RE)	IMF Condition	Ion Mixing Status	Fluctuation Period
2000-11-01	1030-1200 UT	(-8,-16,6)	Extended strong NBZ	Mixed	2-3 min

$\tau_{\text{corr}}^{(i)}$ (s)			$\langle \tau_{\text{corr}}^{(i)} \rangle_i \pm \tau_{\text{rms}}^{(i)}$ (s)	$f_{\text{corr}}^{(i)}$ (Hz)			$d_i$ (Km)	$f_{di}$ (Hz)	$\tau_{di}$ (s)
78 ± 0.2	52 ± 0.2	85 ± 0.2	72 ± 14	0.01	0.02	0.01	115.17	0.41	2.43

$\alpha_{\text{kol}}^{(i)}$			$\langle \alpha_{\text{kol}}^{(i)} \rangle_i \pm \alpha_{\text{rms}}^{(i)}$	$\alpha_{\text{ion}}^{(i)}$			$\langle \alpha_{\text{ion}}^{(i)} \rangle_i \pm \alpha_{\text{rms}}^{(i)}$
-1.60 ± 0.02	-1.67 ± 0.03	-1.66 ± 0.02	1.64 ± 0.03	-2.49 ± 0.01	-2.10 ± 0.01	-2.40 ± 0.01	2.33 ± 0.17

$\kappa^{(i)}$			$\langle \kappa^{(i)} \rangle_i \pm \kappa_{\text{rms}}^{(i)}$
-0.21 ± 0.01	-0.27 ± 0.01	-0.27 ± 0.01	0.25 ± 0.03
saturation and decrease	saturation and decrease	saturation and decrease	

## E2

Date	Time Interval	GSM Position (RE)	IMF Condition	Ion Mixing Status	Fluctuation Period
2002-03-25	0530-0900 UT	(-12,-17,-2)	Extended strong NBZ	Mixed	2-3 min

$\tau_{\text{corr}}^{(i)}$ (s)			$\langle \tau_{\text{corr}}^{(i)} \rangle_i \pm \tau_{\text{rms}}^{(i)}$ (s)	$f_{\text{corr}}^{(i)}$ (Hz)			$d_i$ (Km)	$f_{di}$ (Hz)	$\tau_{di}$ (s)
75 ± 0.2	80 ± 0.2	100 ± 0.2	85 ± 11	0.01	0.01	0.01	184.50	0.26	3.87

$\alpha_{\text{kol}}^{(i)}$			$\langle \alpha_{\text{kol}}^{(i)} \rangle_i \pm \alpha_{\text{rms}}^{(i)}$	$\alpha_{\text{ion}}^{(i)}$			$\langle \alpha_{\text{ion}}^{(i)} \rangle_i \pm \alpha_{\text{rms}}^{(i)}$
-1.69 ± 0.02	-1.69 ± 0.02	-1.73 ± 0.01	1.70 ± 0.02	-2.57 ± 0.04	-2.55 ± 0.01	-2.67 ± 0.01	2.60 ± 0.05

$\kappa^{(i)}$			$\langle \kappa^{(i)} \rangle_i \pm \kappa_{\text{rms}}^{(i)}$
-0.42 ± 0.06	-0.24 ± 0.07	-0.18 ± 0.06	0.28 ± 0.10
saturation and decrease	saturation and decrease	saturation and decrease	

### Geotail – dataset F<sub>a</sub>

Date	Time Interval	GSM Position (RE)	IMF Condition	Ion Mixing Status	Fluctuation Period
2002-03-25	1000-1300 UT	(-8,-16,-1)	Extended strong NBZ	Mixed	2-3 min

$\tau_{\text{corr}}^{(i)}$ (s)			$\langle \tau_{\text{corr}}^{(i)} \rangle_i \pm \tau_{\text{rms}}^{(i)}$ (s)	$f_{\text{corr}}^{(i)}$ (Hz)			$d_i$ (Km)	$f_{\text{di}}$ (Hz)	$\tau_{\text{di}}$ (s)
90 ± 0.2	100 ± 0.2	90 ± 0.2	93 ± 5	0.01	0.01	0.01	184.51	0.26	3.88

$\alpha_{\text{kol}}^{(i)}$			$\langle \alpha_{\text{kol}}^{(i)} \rangle_i \pm \alpha_{\text{rms}}^{(i)}$	$\alpha_{\text{ion}}^{(i)}$			$\langle \alpha_{\text{ion}}^{(i)} \rangle_i \pm \alpha_{\text{rms}}^{(i)}$
-1.60 ± 0.04	-1.61 ± 0.01	-1.55 ± 0.01	1.59 ± 0.03	-2.54 ± 0.01	-2.22 ± 0.01	-2.64 ± 0.01	2.47 ± 0.18

$\kappa^{(i)}$			$\langle \kappa^{(i)} \rangle_i \pm \kappa_{\text{rms}}^{(i)}$	
-0.42 ± 0.01	-0.28 ± 0.01	-0.32 ± 0.01	0.34 ± 0.06	
saturation and decrease	saturation and decrease	saturation and decrease		

### Geotail – dataset F<sub>b</sub>

Date	Time Interval	GSM Position (RE)	IMF Condition	Ion Mixing Status	Fluctuation Period
2002-03-25	1000-1300 UT	(-8,-16,-1)	Extended strong NBZ	Mixed	2-3 min

$\tau_{\text{corr}}^{(i)}$ (s)			$\langle \tau_{\text{corr}}^{(i)} \rangle_i \pm \tau_{\text{rms}}^{(i)}$ (s)	$f_{\text{corr}}^{(i)}$ (Hz)			$d_i$ (Km)	$f_{\text{di}}$ (Hz)	$\tau_{\text{di}}$ (s)
70 ± 0.2	66 ± 0.2	70 ± 0.2	69 ± 19	0.01	0.02	0.01	133.66	0.41	2.42

$\alpha_{\text{kol}}^{(i)}$			$\langle \alpha_{\text{kol}}^{(i)} \rangle_i \pm \alpha_{\text{rms}}^{(i)}$	$\alpha_{\text{ion}}^{(i)}$			$\langle \alpha_{\text{ion}}^{(i)} \rangle_i \pm \alpha_{\text{rms}}^{(i)}$
-1.71 ± 0.02	-1.61 ± 0.01	-1.60 ± 0.05	1.64 ± 0.05	-2.59 ± 0.05	-2.33 ± 0.05	-2.63 ± 0.05	2.52 ± 0.13

$\kappa^{(i)}$			$\langle \kappa^{(i)} \rangle_i \pm \kappa_{\text{rms}}^{(i)}$	
-0.49 ± 0.05	-0.27 ± 0.03	-0.55 ± 0.05	0.44 ± 0.12	
saturation and decrease	saturation	saturation and decrease		

### Geotail – dataset H

Date	Time Interval	GSM Position (RE)	IMF Condition	Ion Mixing Status	Fluctuation Period
2001-01-25	1330-1630 UT	(-22,-21, 0)	Extended strong NBZ	Mixed	~5 min

$\tau_{\text{corr}}^{(i)} \text{ (s)}$			$\langle \tau_{\text{corr}}^{(i)} \rangle_i \pm \tau_{\text{rms}}^{(i)} \text{ (s)}$	$f_{\text{corr}}^{(i)} \text{ (Hz)}$			$d_i \text{ (Km)}$	$f_{di} \text{ (Hz)}$	$\tau_{di} \text{ (s)}$
$90 \pm 0.2$	$120 \pm 0.2$	$80 \pm 0.2$	$97 \pm 17$	0.01	0.01	0.01	167.04	0.17	5.76

$\alpha_{\text{kol}}^{(i)}$			$\langle \alpha_{\text{kol}}^{(i)} \rangle_i \pm \alpha_{\text{rms}}^{(i)}$	$\alpha_{\text{ion}}^{(i)}$			$\langle \alpha_{\text{ion}}^{(i)} \rangle_i \pm \alpha_{\text{rms}}^{(i)}$
$-1.76 \pm 0.03$	$-1.66 \pm 0.02$	$-1.72 \pm 0.02$	$1.71 \pm 0.04$	$-2.44 \pm 0.01$	$-2.26 \pm 0.01$	$-2.28 \pm 0.01$	$2.33 \pm 0.08$

$\kappa^{(i)}$			$\langle \kappa^{(i)} \rangle_i \pm \kappa_{\text{rms}}^{(i)}$
$-0.47 \pm 0.06$	$-0.41 \pm 0.04$	$-0.45 \pm 0.06$	$0.44 \pm 0.02$
saturation and decrease	saturation and decrease	saturation and decrease	

### Geotail – dataset L

Date	Time Interval	GSM Position (RE)	IMF Condition	Ion Mixing Status	Fluctuation Period
1998-08-01	0530-0730 UT	(0, 14, -3)	Extended strong NBZ	Mixed	~3 min

$\tau_{\text{corr}}^{(i)} \text{ (s)}$			$\langle \tau_{\text{corr}}^{(i)} \rangle_i \pm \tau_{\text{rms}}^{(i)} \text{ (s)}$	$f_{\text{corr}}^{(i)} \text{ (Hz)}$			$d_i \text{ (Km)}$	$f_{di} \text{ (Hz)}$	$\tau_{di} \text{ (s)}$
$50 \pm 0.2$	$80 \pm 0.2$	$80 \pm 0.2$	$70 \pm 14$	0.02	0.01	0.01	100.67	0.14	6.87

$\alpha_{\text{kol}}^{(i)}$			$\langle \alpha_{\text{kol}}^{(i)} \rangle_i \pm \alpha_{\text{rms}}^{(i)}$	$\alpha_{\text{ion}}^{(i)}$			$\langle \alpha_{\text{ion}}^{(i)} \rangle_i \pm \alpha_{\text{rms}}^{(i)}$
$-1.54 \pm 0.08$	$-1.34 \pm 0.07$	$-1.54 \pm 0.07$	$1.47 \pm 0.09$	$-2.41 \pm 0.01$	$-2.58 \pm 0.01$	$-2.46 \pm 0.01$	$2.48 \pm 0.07$

$\kappa^{(i)}$			$\langle \kappa^{(i)} \rangle_i \pm \kappa_{\text{rms}}^{(i)}$
$-0.45 \pm 0.11$	$-0.63 \pm 0.07$	$-0.45 \pm 0.06$	$0.51 \pm 0.08$
saturation and increase	increase and saturation	increase and saturation	

### Geotail – dataset M

Date	Time Interval	GSM Position (RE)	IMF Condition	Ion Mixing Status	Fluctuation Period
1999-07-20	0630-0730 UT	(-3, 16,-2)	Extended strong NBZ	Mixed	2-3 min

$\tau_{\text{corr}}^{(i)} \text{ (s)}$			$\langle \tau_{\text{corr}}^{(i)} \rangle_i \pm \tau_{\text{rms}}^{(i)} \text{ (s)}$	$f_{\text{corr}}^{(i)} \text{ (Hz)}$			$d_i \text{ (Km)}$	$f_{di} \text{ (Hz)}$	$\tau_{di} \text{ (s)}$
40 ± 0.2	25 ± 0.2	75 ± 0.2	47 ± 21	0.02	0.04	0.01	77.34	0.47	2.11

$\alpha_{\text{kol}}^{(i)}$			$\langle \alpha_{\text{kol}}^{(i)} \rangle_i \pm \alpha_{\text{rms}}^{(i)}$	$\alpha_{\text{ion}}^{(i)}$			$\langle \alpha_{\text{ion}}^{(i)} \rangle_i \pm \alpha_{\text{rms}}^{(i)}$
-1.66 ± 0.02	-1.68 ± 0.02	-1.60 ± 0.03	1.64 ± 0.03	-2.05 ± 0.01	-2.15 ± 0.01	-2.08 ± 0.01	2.09 ± 0.04

$\kappa^{(i)}$			$\langle \kappa^{(i)} \rangle_i \pm \kappa_{\text{rms}}^{(i)}$
-0.22 ± 0.3	-0.52 ± 0.06	-0.38 ± 0.05	0.37 ± 0.12
saturation and decrease	saturation and decrease	saturation and decrease	

### Geotail – dataset N

Date	Time Interval	GSM Position (RE)	IMF Condition	Ion Mixing Status	Fluctuation Period
1999-02-15	1445-1515 UT	(-4, 16, 2)	NBZ after N-turning	Mixed	~2 min

$\tau_{\text{corr}}^{(i)} \text{ (s)}$			$\langle \tau_{\text{corr}}^{(i)} \rangle_i \pm \tau_{\text{rms}}^{(i)} \text{ (s)}$	$f_{\text{corr}}^{(i)} \text{ (Hz)}$			$d_i \text{ (Km)}$	$f_{di} \text{ (Hz)}$	$\tau_{di} \text{ (s)}$
50 ± 0.2	30 ± 0.2	48 ± 0.2	43 ± 9	0.02	0.03	0.02	137	0.32	3.09

$\alpha_{\text{kol}}^{(i)}$			$\langle \alpha_{\text{kol}}^{(i)} \rangle_i \pm \alpha_{\text{rms}}^{(i)}$	$\alpha_{\text{ion}}^{(i)}$			$\langle \alpha_{\text{ion}}^{(i)} \rangle_i \pm \alpha_{\text{rms}}^{(i)}$
-1.67 ± 0.07	-1.86 ± 0.03	-1.78 ± 0.03	1.77 ± 0.08	-2.42 ± 0.03	-2.53 ± 0.01	-2.43 ± 0.01	2.46 ± 0.05

$\kappa^{(i)}$			$\langle \kappa^{(i)} \rangle_i \pm \kappa_{\text{rms}}^{(i)}$
-0.28 ± 0.10	-0.38 ± 0.06	-0.28 ± 0.10	0.31 ± 0.05
saturation	increase and saturation	saturation	

### Event O

Date	Time Interval	GSM Position (RE)	IMF Condition	Ion Mixing Status	Fluctuation Period
1997-01-10	2050-2400 UT	(-7, 16, 4)	Nondominant NBZ after N-turning	Weakly Mixed	2- 3 min

$\tau^{(i)}_{\text{corr}} \text{ (s)}$			$\langle \tau^{(i)}_{\text{corr}} \rangle_i \pm \tau^{(i)}_{\text{rms}} \text{ (s)}$	$f^{(i)}_{\text{corr}} \text{ (Hz)}$			$d_i \text{ (Km)}$	$f_{di} \text{ (Hz)}$	$\tau_{di} \text{ (s)}$
120 ± 0.2	70 ± 0.2	90 ± 0.2	93 ± 20	0.01	0.01	0.01	135.60	0.20	5.03

$\alpha^{(i)}_{\text{kol}}$			$\langle \alpha^{(i)}_{\text{kol}} \rangle_i \pm \alpha^{(i)}_{\text{rms}}$	$\alpha^{(i)}_{\text{ion}}$			$\langle \alpha^{(i)}_{\text{ion}} \rangle_i \pm \alpha^{(i)}_{\text{rms}}$
-1.61 ± 0.02	-1.74 ± 0.02	-1.67 ± 0.02	1.67 ± 0.05	-2.38 ± 0.01	-2.64 ± 0.01	-2.60 ± 0.01	2.54 ± 0.11

$\kappa^{(i)}$			$\langle \kappa^{(i)} \rangle_i \pm \kappa^{(i)}_{\text{rms}}$
-0.40 ± 0.04	-0.46 ± 0.04	-0.36 ± 0.04	0.40 ± 0.04
saturation	saturation	saturation	

### Geotail – dataset P

Date	Time Interval	GSM Position (RE)	IMF Condition	Ion Mixing Status	Fluctuation Period
1997-01-11	0400-0500 UT	(-13, 16, 4)	Extended Strong NBZ	Mixed	~3 min

$\tau^{(i)}_{\text{corr}} \text{ (s)}$			$\langle \tau^{(i)}_{\text{corr}} \rangle_i \pm \tau^{(i)}_{\text{rms}} \text{ (s)}$	$f^{(i)}_{\text{corr}} \text{ (Hz)}$			$d_i \text{ (Km)}$	$f_{di} \text{ (Hz)}$	$\tau_{di} \text{ (s)}$
147 ± 0.2	40 ± 0.2	40 ± 0.2	76 ± 50	0.01	0.02	0.02	107.14	0.32	3.07

$\alpha^{(i)}_{\text{kol}}$			$\langle \alpha^{(i)}_{\text{kol}} \rangle_i \pm \alpha^{(i)}_{\text{rms}}$	$\alpha^{(i)}_{\text{ion}}$			$\langle \alpha^{(i)}_{\text{ion}} \rangle_i \pm \alpha^{(i)}_{\text{rms}}$
-1.71 ± 0.03	-1.63 ± 0.03	-1.61 ± 0.03	1.65 ± 0.04	-2.63 ± 0.01	-2.63 ± 0.01	-2.45 ± 0.02	2.57 ± 0.08

$\kappa^{(i)}$			$\langle \kappa^{(i)} \rangle_i \pm \kappa^{(i)}_{\text{rms}}$
-0.42 ± 0.06	-0.49 ± 0.06	-0.37 ± 0.06	0.43 ± 0.05
saturation	saturation	saturation	

### Geotail – dataset Q

Date		Time Interval	GSM Position (RE)	IMF Condition	Ion Mixing Status	Fluctuation Period
1997-02-12		1430-1600 UT	(-13, 22, 3)	Extended Strong NBZ	Mixed	~2 min

$\tau_{\text{corr}}^{(i)} \text{ (s)}$			$\langle \tau_{\text{corr}}^{(i)} \rangle_i \pm \tau_{\text{rms}}^{(i)} \text{ (s)}$	$f_{\text{corr}}^{(i)} \text{ (Hz)}$			$d_i \text{ (Km)}$	$f_{\text{di}} \text{ (Hz)}$	$\tau_{\text{di}} \text{ (s)}$
27 ± 0.2	30 ± 0.2	40 ± 0.2	32 ± 5	0.04	0.03	0.02	142.53	0.31	3.18

$\alpha_{\text{kol}}^{(i)}$			$\langle \alpha_{\text{kol}}^{(i)} \rangle_i \pm \alpha_{\text{rms}}^{(i)}$	$\alpha_{\text{ion}}^{(i)}$			$\langle \alpha_{\text{ion}}^{(i)} \rangle_i \pm \alpha_{\text{rms}}^{(i)}$
-1.64 ± 0.03	-1.61 ± 0.03	-1.59 ± 0.03	1.61 ± 0.02	-2.69 ± 0.01	-2.56 ± 0.01	-2.41 ± 0.01	2.55 ± 0.11

$\kappa^{(i)}$			$\langle \kappa^{(i)} \rangle_i \pm \kappa_{\text{rms}}^{(i)}$
-0.33 ± 0.10	-0.42 ± 0.06	-0.38 ± 0.06	0.38 ± 0.04
saturation	saturation	saturation and increase	

### Geotail – dataset R

Date		Time Interval	GSM Position (RE)	IMF Condition	Ion Mixing Status	Fluctuation Period
2003-07-17		0330-0500 UT	(-13, 23,-1)	Nondominant NBZ after N-turning	Weakly Mixed	~2 min

$\tau_{\text{corr}}^{(i)} \text{ (s)}$			$\langle \tau_{\text{corr}}^{(i)} \rangle_i \pm \tau_{\text{rms}}^{(i)} \text{ (s)}$	$f_{\text{corr}}^{(i)} \text{ (Hz)}$			$d_i \text{ (Km)}$	$f_{\text{di}} \text{ (Hz)}$	$\tau_{\text{di}} \text{ (s)}$
80 ± 0.2	35 ± 0.2	50 ± 0.2	55 ± 19	0.01	0.03	0.02	223.71	0.3	3.35

$\alpha_{\text{kol}}^{(i)}$			$\langle \alpha_{\text{kol}}^{(i)} \rangle_i \pm \alpha_{\text{rms}}^{(i)}$	$\alpha_{\text{ion}}^{(i)}$			$\langle \alpha_{\text{ion}}^{(i)} \rangle_i \pm \alpha_{\text{rms}}^{(i)}$
-1.69 ± 0.03	-1.74 ± 0.02	-1.68 ± 0.04	1.70 ± 0.03	-2.20 ± 0.01	-2.33 ± 0.01	-2.65 ± 0.01	2.39 ± 0.19

$\kappa^{(i)}$			$\langle \kappa^{(i)} \rangle_i \pm \kappa_{\text{rms}}^{(i)}$
-0.27 ± 0.06	-0.37 ± 0.06	-0.31 ± 0.10	0.31 ± 0.04
decrease	decrease	decrease	

## Geotail – dataset S

Date	Time Interval	GSM Position (RE)	IMF Condition	Ion Mixing Status	Fluctuation Period
1995-03-24	0600-0800 UT	(-15, 20, 4)	Extended Strong NBZ	Mixed	2-3 min

$\tau^{(i)}_{\text{corr}} \text{ (s)}$			$\langle \tau^{(i)}_{\text{corr}} \rangle_i \pm \tau^{(i)}_{\text{rms}} \text{ (s)}$	$f^{(i)}_{\text{corr}} \text{ (Hz)}$			$d_i \text{ (Km)}$	$f_{di} \text{ (Hz)}$	$\tau_{di} \text{ (s)}$
$50 \pm 0.2$	$40 \pm 0.2$	$40 \pm 0.2$	$43 \pm 5$	0.02	0.02	0.02	88.59	0.41	2.45

$\alpha^{(i)}_{\text{kol}}$			$\langle \alpha^{(i)}_{\text{kol}} \rangle_i \pm \alpha^{(i)}_{\text{rms}}$	$\alpha^{(i)}_{\text{ion}}$			$\langle \alpha^{(i)}_{\text{ion}} \rangle_i \pm \alpha^{(i)}_{\text{rms}}$
$-1.64 \pm 0.02$	$-1.55 \pm 0.01$	$-1.57 \pm 0.01$	$1.58 \pm 0.04$	$-2.59 \pm 0.01$	$-2.64 \pm 0.01$	$-2.53 \pm 0.01$	$2.59 \pm 0.04$

$\kappa^{(i)}$			$\langle \kappa^{(i)} \rangle_i \pm \kappa^{(i)}_{\text{rms}}$
$-0.43 \pm 0.03$	$-0.39 \pm 0.03$	$-0.38 \pm 0.04$	$0.40 \pm 0.02$
increase	increase	saturation	

## Geotail – dataset T

Date	Time Interval	GSM Position (RE)	IMF Condition	Ion Mixing Status	Fluctuation Period
1998-04-13	0315-0430 UT	(-18, 20, 4)	Extended Strong NBZ	Mixed	2-3 min

$\tau^{(i)}_{\text{corr}} \text{ (s)}$			$\langle \tau^{(i)}_{\text{corr}} \rangle_i \pm \tau^{(i)}_{\text{rms}} \text{ (s)}$	$f^{(i)}_{\text{corr}} \text{ (Hz)}$			$d_i \text{ (Km)}$	$f_{di} \text{ (Hz)}$	$\tau_{di} \text{ (s)}$
$60 \pm 0.2$	$55 \pm 0.2$	$40 \pm 0.2$	$52 \pm 8$	0.02	0.02	0.02	190.83	0.27	3.84

$\alpha^{(i)}_{\text{kol}}$			$\langle \alpha^{(i)}_{\text{kol}} \rangle_i \pm \alpha^{(i)}_{\text{rms}}$	$\alpha^{(i)}_{\text{ion}}$			$\langle \alpha^{(i)}_{\text{ion}} \rangle_i \pm \alpha^{(i)}_{\text{rms}}$
$-1.54 \pm 0.08$	$-1.67 \pm 0.03$	$-1.59 \pm 0.03$	$1.60 \pm 0.05$	$-2.41 \pm 0.01$	$-2.58 \pm 0.01$	$-2.46 \pm 0.01$	$2.48 \pm 0.07$

$\kappa^{(i)}$			$\langle \kappa^{(i)} \rangle_i \pm \kappa^{(i)}_{\text{rms}}$
$-0.54 \pm 0.04$	$-0.48 \pm 0.04$	$-0.34 \pm 0.05$	$0.45 \pm 0.08$
saturation	saturation	saturation	

### THEMIS – dataset TH1

Date	Time Interval	GSM Position (RE)	IMF Condition	Ion Mixing Status	Fluctuation Period
2008-11-06	0850-0920 UT	(-0.3, -15.3, 4.6)	Not specified	Not specified	Not specified

$\tau^{(i)}_{\text{corr}} \text{ (s)}$			$\langle \tau^{(i)}_{\text{corr}} \rangle_i \pm \tau^{(i)}_{\text{rms}} \text{ (s)}$	$f^{(i)}_{\text{corr}} \text{ (Hz)}$			$d_i \text{ (Km)}$	$f_{di} \text{ (Hz)}$	$\tau_{di} \text{ (s)}$
36 ± 0.2	20 ± 0.2	50 ± 0.2	35 ± 12	0.03	0.05	0.02	122.78	0.37	2.68

$\alpha^{(i)}_{\text{kol}}$			$\langle \alpha^{(i)}_{\text{kol}} \rangle_i \pm \alpha^{(i)}_{\text{rms}}$	$\alpha^{(i)}_{\text{ion}}$			$\langle \alpha^{(i)}_{\text{ion}} \rangle_i \pm \alpha^{(i)}_{\text{rms}}$
-1.70 ± 0.01	-1.62 ± 0.02	-1.61 ± 0.02	-1.64 ± 0.04	-2.62 ± 0.01	-2.76 ± 0.01	-2.48 ± 0.01	-2.62 ± 0.11

$\kappa^{(i)}$			$\langle \kappa^{(i)} \rangle_i \pm \kappa^{(i)}_{\text{rms}}$
-0.24 ± 0.03	-0.40 ± 0.04	-0.57 ± 0.06	0.40 ± 0.13
saturation and decrease	decrease	decrease	

### THEMIS – dataset TH2

Date	Time Interval	GSM Position (RE)	IMF Condition	Ion Mixing Status	Fluctuation Period
2008-11-18	0720-0730 UT	(-2.3, -17, 3.4)	Not specified	Not specified	Not specified

$\tau^{(i)}_{\text{corr}} \text{ (s)}$			$\langle \tau^{(i)}_{\text{corr}} \rangle_i \pm \tau^{(i)}_{\text{rms}} \text{ (s)}$	$f^{(i)}_{\text{corr}} \text{ (Hz)}$			$d_i \text{ (Km)}$	$f_{di} \text{ (Hz)}$	$\tau_{di} \text{ (s)}$
25 ± 0.2	13 ± 0.2	29 ± 0.2	22 ± 7	0.04	0.08	0.03	162.33	0.34	2.93

$\alpha^{(i)}_{\text{kol}}$			$\langle \alpha^{(i)}_{\text{kol}} \rangle_i \pm \alpha^{(i)}_{\text{rms}}$	$\alpha^{(i)}_{\text{ion}}$			$\langle \alpha^{(i)}_{\text{ion}} \rangle_i \pm \alpha^{(i)}_{\text{rms}}$
-1.77 ± 0.10	-1.64 ± 0.34	-1.68 ± 0.03	-1.70 ± 0.05	-2.50 ± 0.01	-2.49 ± 0.01	-2.48 ± 0.01	-2.49 ± 0.01

$\kappa^{(i)}$			$\langle \kappa^{(i)} \rangle_i \pm \kappa^{(i)}_{\text{rms}}$
-0.42 ± 0.06	-0.42 ± 0.10	-0.26 ± 0.06	0.37 ± 0.07
decrease	decrease	decrease	

# Appendix B - Geocentric systems

Coordinate systems used in the study of Earth-Sun relations are different, depending on the physical processes to be describe. For a comprehensive description of the transformation between the major coordinate systems in use see Russel, 1971 [54] and Hapgood, 1992 [106].

We focus our attention on geocentric systems, i.e. the cartesian coordinate systems originated in the center of the Earth. Typically they can be divided into three categories:

- Systems based on the rotational axis of the Earth: the Geographic Coordinate System (GEO), is defined so that its X-axis is in the Earth's equatorial plane but is fixed with the rotation of the Earth so that it passes through the Greenwich meridian. Its Z-axis is parallel to the rotation axis of the Earth, and its Y-axis completes a right-handed orthogonal set  $Y = Z \times X$ ; the Geocentric Equatorial Inertial System (GEI), has its X-axis pointing from the Earth towards the first point of Aries (the position of the Sun at the vernal equinox). This direction is the intersection of the Earth's equatorial plane and the ecliptic plane and thus the X-axis lies in both planes. The Z-axis is parallel to the

rotation axis of the Earth and Y completes the right-handed orthogonal set  $Y = Z \times X$ ;

- Systems based on the Earth-Sun line: the Geocentric Solar Ecliptic (GSE) has its X axis towards the Sun and its Z axis perpendicular to the plane of the Earth's orbit around the Sun (positive North). This system is fixed with respect to the Earth-Sun line. The Geocentric Solar Magnetospheric (GSM), has its X axis towards the Sun and its Z axis is the projection of the Earth's magnetic dipole axis (positive North) on to the plane perpendicular to the X axis. The direction of the geomagnetic field near the nose of the magnetosphere is well-ordered by this system. Thus it is considered the best system to use when studying the effects of interplanetary magnetic field components (e.g.  $B_z$ ) on magnetospheric and ionospheric phenomena.
- Systems based on the magnetic axis of the Earth's magnetic dipole; in the Solar Magnetic (SM), the Z-axis is chosen parallel to the north magnetic pole and its Y axis is perpendicular to the plane containing the dipole axis and the Earth-Sun line (positive in direction opposite to the Earth's orbital motion). The direction of the geomagnetic field in the outer magnetosphere is well-ordered by this system. GeoMagnetic (MAG), instead, has the Z-axis of the dipole meridian system (DM) chosen along the north magnetic dipole axis. However, the Y-axis is chosen to be perpendicular to a radius vector to the point of observation rather than the Sun. The positive Y direction is chosen to be eastwards, so that the X-axis is directed outwards from the dipole.

# Bibliography

- [1] AKHIEZER, A. I., AKHIEZER, A., POLOVIN, R. V., SITENKO, A. G., AND STEPANOV, K. N., *Plasma electrodynamics, Vol. 2 Linear Theory*, Pergamon, New York, 1975.
- [2] ALEXANDROVA, O., CHEN, C. H. K., SORRISO-VALVO, L. ET AL., *Solar Wind Turbulence and the Role of Ion Instabilities*, *Space Sci. Rev.*, **178**, 101-139, 2013.
- [3] ALFVEN, H., *A theory of the magnetic storms and the aurorae II and III*, *Kgl. Sv. Vet. ak. Handl. Tredje Ser.*, **18**, 9, 1940.
- [4] ANSELMET, F, GAGNE., Y, HOPFINGER, E. J AND ANTONIA, R. A., *High-order velocity structure functions in turbulent shear flows*, *J. Fluid Mech.*, **140**, 25, 63-89, 1984.
- [5] ARNEODO, A., BACRY, E. AND MUZY, J. F., *Random cascades on wavelet dyadic trees* , *J. Math. Phys.*, **39**, 4142, 1998.
- [6] BAUMJOHANN, R. A. AND TREUMANN, W., *Basic space plasma physics*, Imperial College Press, London, 1999.
- [7] BAVASSANO CATTANEO, M. B., MARCUCCI, M. F., BOGDANOVA, Y. V., REME, H., DANDOURAS, I., KISTLER, L. M. AND LUCEK, E., *Global reconnection topology as inferred from plasma observations inside Kelvin-Helmholtz vortices*, *Ann. Geophys.*, **28**, 893-906, 2010.
- [8] BELMONT, G., GRAPPIN, R., MOTTEZ, F., PANTELLINI, F. AND PELLETIER, G., *Collisionless plasmas in astrophysics*, John Wiley Sons, Chichester, 2013.

- [9] BENZI, R., BIFERALE, L., CRISANTI, A., PALADIN, G., VERGASOLA, M. AND VULPIANI, A., *A random process for the construction of multiaffine fields*, Physica D: Nonlinear Phenomena, **65**, 352-358, 1993.
- [10] BENZI, R., PALADIN, L., PARISI, G. AND VULPIANI, A., *On the multifractal nature of fully developed turbulence and chaotic systems*, J. Phys., **A17**, 3521-3531, 1984.
- [11] BIFERALE, L., BOFFETTA, G., CELANI, A., CRISANTI, A. AND VULPIANI, A., *Mimicking a turbulent signal: Sequential multiaffine processes*, Phys. Rev., **E 57**, R6261(R), 1998.
- [12] BOROVSKY, J E., THOMSEN, M. F. AND ELPIC, R. C., *The driving of the plasma sheet by the solar wind*, J. of Geophys. Res.: Space Physics 1978-2012, **103**, A8, 617-639, 1998.
- [13] BREUILLARD, H., YORDANOVA, E., VAIVADS, A., ALEXANDROVA, O., *The effects of kinetic instabilities on small-scale turbulence in Earth's magnetosheath*, Astrophys. J., **829**, 54-60, 2016.
- [14] BRUNO, R. AND CARBONE, V., *The solar wind as a turbulence laboratory*, Living Rev. Sol. Phys., **2**, 4, 2005.
- [15] BURLAGA, L. F., *Interplanetary magnetohydrodynamics*, International Series in Astronomy and Astrophysics, **3** Oxford University Press, Oxford, 272, 1995.
- [16] CAMETTI, F., CARBONE, V. AND VELTRI, P., *Synthetic 3-D turbulence*, J. Phys., **IV**, 08, 197, 1998.
- [17] CARBONE, V. AND VELTRI, P., *A Shell Model for Anisotropic Magnetohydrodynamic Turbulence*, Geophys. and Astrophys. Fluid Dynamics, **5**, 153-181, 1990.
- [18] CHASTON, C. C., WILBER, M., MOZER, F. S., FUJIMOTO, M., GOLDSTEIN, M. L., ACUNA, M., REME, H. AND FAZAKERLEY, A., *Mode conversion and anomalous transport in Kelvin-Helmholtz vortices and kinetic Alfvén waves at the Earth's magnetopause*, Phys. Rev. Lett., **99(17)**, 175004, 2007.

- [19] CHASTON, C. C., BONNELL, J. W., CLAUSEN, L. AND ANGELOPOULOS V., *Energy transport by kinetic-scale electromagnetic waves in fast plasma sheet flows*, J. Geophys. Res., **117**, A09202, 2012.
- [20] CHEN, C. H. K., MALLET, A., YOUSEF, T. A., SCHEKOCHIHIN, A. A. AND HORBURY, T. S., *Anisotropy of Alfvénic turbulence in the solar wind and numerical simulations*, Mon. Not. R. Astron. Soc., **415**, 4, 3219-3226, 2011.
- [21] CHEN, S. H. AND KIVELSON, M. G., *Nonsinusoidal waves at the magnetopause*, Geophys. Res. Lett., **20**, 2699-2702, 1993.
- [22] CHEN, S. H., KIVELSON, M. G., GOSLING, J. T., WALKER, R. J. AND LAZARUS, A. J., *Anomalous aspects of magnetosheath flow and of the shape and oscillations of the magnetopause during an interval of strongly northward interplanetary magnetic field*, J. of Geophys. Res., **98**, 5727-5742, 1993.
- [23] CHHABRA, A. B., MENEVEAU, C., JENSEN, M. H. AND SREENIVASAN, K. R., *Direct determination of the  $f(\alpha)$  singularity spectrum and its application to fully developed turbulence*, Phys. Rev., **A 40**, 5284, 1989.
- [24] COWLEY, S., W., H., *Evidence for the occurrence and importance of reconnection between the earth's magnetic field and the interplanetary magnetic field*, Magnetic Reconnection in Space and Laboratory Plasmas, 375-378, 1984.
- [25] CRAVENS, T. E., *Physics of Solar System Plasmas*, Cambridge University Press, Cambridge, 1997.
- [26] DOBROWOLNY, M., MANGENEY, A., AND VELTRI, P., *Fully developed anisotropic hydromagnetic turbulence in the interplanetary space*, Phys. Rev. Lett., **45**, 144, 1980.
- [27] DOKE, T., FUJII, M., FUJIMOTO, M., FUJIKI, K., FUKUI, T., GLIEM, F., GUTTLER, W., HASEBE, N., HAYASHI, W., ITO, T., ITSUMI, K. ET AL., *The Energetic Particle Spectrometer HEP onboard the Geotail spacecraft*, J. of Geomagnetism and Geoelectricity, **46**, 1, 713-733, 1994.

- [28] DOKE, T., HASEBE, N., HAYASHI, T., ITSUMI, K., KIKUCHI, J., KOBAYASHI, M. N., KONDOH, K., SHIRAI, H., TAKASHIMA, T., TAKEHANA, T., YAMADA, Y., YANAGIMACHI, T. AND YASHIRO, J., *Observation of galactic cosmic ray particles by the HEP-HI telescope on the GEOTAIL satellite*, Advances in Space Research, **23**, 3, 487-490, 1999.
- [29] DOUADY, S., COUDER, Y. AND BRACHET, M. E., *Direct observation of the intermittency of intense vorticity filaments in turbulence*, Phys. Rev. Lett., **67**, 983, 1991.
- [30] DUBRULLE, B., *Intermittency in fully developed turbulence: Log-Poisson statistics and generalized scale covariance*, Phys. Rev. Lett., **73**, 959, 1994.
- [31] DUDOK DE WIT, T., ALEXANDROVA, O., FURNO, I., SORRISO-VALVO, L. AND ZIMBARDO, G., *Methods for characterising microphysical processes in plasmas*, Space Sci. Rev., **178**, 665, 2013.
- [32] DUDOK DE WIT, T., *Can high-order moments be meaningfully estimated from experimental turbulence measurements?*, Phys. Rev., **E 70**, 055302 (R), 2004.
- [33] DUNGEY, J. W., *The interplanetary magnetic field and the auroral zones*, Phys. Rev. Lett., **6**, 1961.
- [34] DUNGEY, W. J., *The structure of the exosphere or adventures in velocity space*, Geophysics, The Earth's Environment, **503**, 1963.
- [35] DUNGEY, W. J., *Electrodynamics of the outer atmosphere*, Physics of the Ionosphere, **1**, 229, 1955.
- [36] EASTMAN, T. E., BOARDSEN, S. A., CHEN, S. H., FUNG, S. F. AND KESSEL, R. L., *Configuration of high-latitude and high-altitude boundary layers*, J. of Geophys. Res., **105**, 23221-23238, 2000.
- [37] ELSÄSSER, W. M., *The hydromagnetic equations*, Phys. Rev., **79**, 183, 1950.
- [38] FAIRFIELD, D. H., FARRUGIA, C. J., MUKAI, T., NAGAI, T. AND FEDEROV, A., *Motion of the dusk flank boundary layer caused by solar wind pressure changes and the Kelvin-Helmholtz instability: 10-11 January 1997*, J. Geophys. Res., **108**, A12, 2003.

- [39] FAIRFIELD, D. H., OTTO, A., MUKAI, T., KOKUBUN, S., LEPING, R. P., STEINBERG, J. T., LAZARUS, A. J. AND YAMAMOTO, T., *Geotail observations of the Kelvin-Helmholtz instability at the equatorial magnetotail boundary for parallel northward fields*, J. Geophys. Res., **105**, 21, 2000.
- [40] FAIRFIELD, B., MAMMARELLA, N. AND DI DOMENICO, A., *Centenarian's "Holy" Memory: is being positive enough?*, J. Gen. Psychol., **174**, 2013.
- [41] FAIRFIELD, D. H., KUZNETSOVA, M M, MUKAI, T., NAGAI, T., GOMBOSI, T. I. AND RIDLEY, A. J., *Waves on the dusk flank boundary layer during very northward interplanetary magnetic field conditions: Observations and simulation*, J. of Geophys. Res., Space Physics 1978-2012, **112**, A8, 2007.
- [42] FALCONER, K., *Fractal Geometry: Mathematical Foundations and Applications*, John Wiley Sons, Chichester, 1990.
- [43] FARRUGIA, C. J., GRATTON, F. T. AND TORBERT, R. B., *Viscous-type processes in the solar wind-magnetosphere interaction*, Space Science Reviews, **95**,1-2, 2001.
- [44] FOULLON, C., FARRUGIA, C. J., FAZAKERLEY, A. N., OWEN, C. J., GRATTON, F. T. AND TORBERT, R. B., *Evolution of Kelvin-Helmholtz activity on the dusk flank magnetopause*, J. Geophys. Res., **113**, A11203, 2008.
- [45] FRANK, L.A., ACKERSON, K. L., PATERSON, W. R., LEE, J. A., ENGLISH, M. AND PICKETT, G. L., *The Comprehensive Plasma Instrumentation (CPI) for the GEOTAIL Spacecraft*, J. of Geomagnetism and Geoelectricity, **46**, 1, 1994.
- [46] FREDRICKS, R. W., CORONITI, F. V., *Ambiguities in the deduction of rest frame fluctuation spectrums from spectrums computed in moving frames*, J. Geophys. Res. 81, 5591, 1976.
- [47] FRISCH, U. AND PARISI, G., *Turbulence and Predictability in Geophysical Fluid Dynamics and Climatology, Proceedings of the International School of Physics "Enrico Fermi", Varenna, 1983*, edited by M. Ghil, R. Benzi G. Parisi, North Holland, Amsterdam, 84, 1985.

- [48] FRISCH, U., *Turbulence. The legacy of A. N. Kolmogorov*, Cambridge University Press, Cambridge, UK, 1995.
- [49] FUJIMOTO, M., TERASAWA, T., MUKAI, T., SAITO, Y., YAMAMOTO, T. AND KOKUBUN, S., *Plasma entry from the flanks of the near-Earth magnetotail: GEOTAIL observations*, J. Geophys. Res. Space Physics 1978-2012 , **103**, A3, 4391-4408, 1998.
- [50] FUJIMOTO, M., TONOOKA, T AND MUKAI, T., *Vortex-like fluctuations in the magnetotail flanks and their possible roles in plasma transport in Earth's Low-Latitude Boundary Layer*, Geophys. Monogr. Ser., **133**, edited by Newell, P. T. and Onsager, T., 241-251, AGU, Washington D. C., 2003.
- [51] GOLDREICH, P. AND SRIDHAR, S., *Toward a theory of interstellar turbulence. II. Strong Alfvénic turbulence*, Astrophys. J., **438**, 763-775, 1995.
- [52] HAERENDEL, G., PASCHMANN, G., SCKOPKE, N., ROSENBAUER, H. AND HEDGECOCK, P. C., *The frontside boundary layer of the magnetosphere and the problem of reconnection*, J. of Geophys. Res., **83**, 3195-3216, 1978.
- [53] HALSEY, T. C., JENSEN, M. H., KADANOFF, L. P., PROCACCIA, I. I. AND SHRAIMAN, B. I., *Fractal measures and their singularities: The characterization of strange sets* , Phys. Rev., **A 33**, 1141-1151, 1986.
- [54] HAPGOOD, M. A. , *Space Physics Coordinate Transformations: A users guide*, Planet Space Sci., **40**, 711-717, 1992.
- [55] HASEGAWA, H, FUJIMOTO, M., TAKAGI, K., SAITO, Y., MUKAI, T. AND RÉME, H., *Single-spacecraft detection of rolled-up Kelvin-Helmholtz vortices at the flank magnetopause*, J. of Geophys. Res., **111**, 2006.
- [56] HASEGAWA, H., FUJIMOTO, M., PHAN, T D., REME, H., BALOGH, A., DUNLOP, M., W., HASHIMOTO, C. AND TANDOKORO, R., *Transport of solar wind into Earth's magnetosphere through rolled-up Kelvin-Helmholtz vortices*, Nature, **430**, 755-758, 2004a.
- [57] HASEGAWA, H., RETINÒ, A., VAIVADS, A., KHOTYAINTEV, Y., ANDRE, M., NAKAMURA, T. H. M., TEH, W. L., SONNERUP, B. U. O.,

- SCHWARTZ, S., J., SEKI, Y., FUJIMOTO, M., SAITO, M., REME, H. AND CANU, P., *Kelvin-Helmholtz waves at the Earth's magnetopause: Multiscale development and associated reconnection*, J. of Geophys. Res., **114**, A12207, 2009.
- [58] HASEGAWA, H.,FUJIMOTO, M., SAITO, Y. AND MUKAI, T., *Dense and stagnant ions in the low-latitude boundary region under northward interplanetary magnetic field*, Geophys Res. Lett., **31**, 6, 2004.
- [59] HONES, E. W., ASBRIDGE, J. R., BAME, S. J., MONTGOMERY, M. D., SINGER, S. AND AKASOFU, S. I., *Measurements of magnetotail plasma flow made with Vela 4B*, J. of Geophys. Res., **77**, 1972.
- [60] HORBURY, T. S., FORMAN, M AND OUGHTON, S., *Anisotropic Scaling of Magnetohydrodynamic Turbulence*, Phys. Rev. Lett., **101**, 17, 175005, 2008.
- [61] JUNEJA, A., LATHROP, D. P., SREENIVASAN, K. R. AND STOLOVITZKY, G., *Synthetic turbulence*, Phys. Rev., **E 49**, 5179-5194, 1994.
- [62] KASABA, Y., HAYAKAWA, H., ISHISAKA, K., OKADA, T., MATSUOKA, A., MUKAI, T. AND TAKEI, T., *Evaluation of DC electric field measurement by the double probe system aboard the Geotail spacecraft*, Advances in Space Research, **37**, 3, 604-609, 2006.
- [63] KERSTEIN, A. R., ASHURST, W. T., WUNSCH, S. AND NILSEN, V., *One-dimensional turbulence: Vector formulation and application to free shear flows* , J. Fluid Mech, **447**, 85, 2001.
- [64] KIVELSON, M. G. AND CHEN, S. H., *The magnetopause: Surface waves and instabilities and their possible dynamic consequences*, in *Physics of the Magnetopause*, Geophys. Monogr. Ser., **90**, edited by Song, P., Sonnerup, B. U. Ö. and Thomsen, M. F., 257-268, AGU,Washington, D. C., 1995.
- [65] KLEIN, K. G., HOWES, G. G., TENBARGE, J. M., *The violation of the Taylor hypothesis in measurements of solar wind turbulence*, Astrophys. J. Lett., **790** L20, 2014.

- [66] KOKUBUN, S., YAMAMOTO, T., ACUNA, M. H., HAYASHI, K., SHIOKAWA, K. AND KAWANO, H., *The Geotail Magnetic Field Experiment*, J. Geomag. Geo-electr., **46**, 1994.
- [67] KOLMOGOROV, A. N., *A refinement of previous hypotheses concerning the local structure of turbulence in a viscous incompressible fluid at high Reynolds number*, J. Fluid Mechanics, **13**, 1, 82, 1962.
- [68] KOLMOGOROV, A. N., *Local structure of turbulence in incompressible fluid*, Dokl. Akad. Nauk SSSR, **30**, 9-13, 1941, (in russian), translated in "Kolmogorov ideas 50 years on", Proc. R. Soc. Lond. A, **434**, 9-13, Eds. J.C.R. Hunt and O. M. Phillips, 1995.
- [69] KRAICHNAN, R. H., *Inertial-range spectrum of hydromagnetic turbulence*, Phys. Fluids, **8**, 1385, 1965.
- [70] LANDAU, L. D. & LIFSHITZ, E. M., *Fluids Mechanics*, 2nd edition, Pergamon, Oxford, 1987.
- [71] LEAMON, R. J., SMITH, C. W., NESS, N. F., MATTHAEUS, W. H., OBSERVATIONAL CONSTRAINTS ON THE DYNAMICS OF THE INTERPLANETARY MAGNETIC FIELD DISSIPATION RANGE, J. of Geophys. Res., **103**, A3, 4775-4787, 1998.
- [72] LEPRETI, F., CARBONE, V. AND VELTRI, P., *Model for intermittency of energy dissipation in turbulent flows*, Phys. Rev., **E 74**, 026306, 2006.
- [73] LIN, D., WANG, C., LI, W., TANG, B., GUO, X. AND PENG, Z., *Properties of Kelvin-Helmholtz waves at the magnetopause under northward interplanetary magnetic field: Statistical study*, J. Geophys. Res. Space Physics, **119**, 7485-7494, 2014.
- [74] LUI, A. T. Y., VENKATESAN, D. AND MURPHREE, J. S., *Auroral bright spots on the dayside oval*, J. of Geophys. Res., **94**, 5515-5522, 1989.
- [75] MALARA, F., DI MARE, F., NIGRO, G. AND SORRISO-VALVO, L., *Fast algorithm for a three-dimensional model of intermittent turbulence*, Phys. Rev., **E 94**, 053109, 2016.
- [76] MANDELBROT, B. B., *Fractals: Form, Chance and Dimension*, Freeman Co., San Francisco, 1977.

- [77] MANDELBROT, B. B., *The fractal geometry of nature*, Freeman, San Francisco, 1982.
- [78] MATSUMOTO, H., NAGANO, I., ANDERSON, R. R., KOJIMA, H., HASHIMOTO, K., TSUTSUI, M., OKADA, K., KIMURA, H., OMURA, Y. AND OKADA, M., *Plasma Wave Observations with GEOTAIL Spacecraft*, J. of Geomagnetism and Geoelectricity, **46**, 1, 1994.
- [79] MATSUMOTO, Y. AND SEKI, K., *Formation of a broad plasma turbulent layer by forward and inverse energy cascades of the kelvin-helmholtz instability*, J. of Geophys. Res.: Space Physics 1978-2012, **115**, A10, 2010.
- [80] MATTHAEUS, W. H., GOLDSTEIN, M. L., 1982a, *Measurement of the rugged invariants of magnetohydrodynamic turbulence*, J. Geophys. Res., **87**, 6011, 1982.
- [81] MATTHAEUS, W. H., GOLDSTEIN, M. L. 1982b, *Stationarity of magnetohydrodynamic fluctuations in the solar wind* J. Geophys. Res., **87**, 10347, Neugebauer, M., Science, 252, 404, 1991.
- [82] MATTHAEUS, W. H., GOLDSTEIN, M. L. AND J. KING, J., *An interplanetary magnetic field ensemble at 1 AU*, J. Geophys. Res., **91**, 59, 1986.
- [83] MATTHAEUS, W. H., GOLDSTEIN, M. L. AND ROBERTS, D. A., *Evidence for the presence of quasi-two-dimensional fluctuations in the solar wind*, J. Geophys. Res., **95**, 20, 673-695, 1990.
- [84] MCCOMAS, D. J., BARRACLOUGH, B. L., FUNSTEN, H. O., GOSLING, J. T., SANTIAGO-MUNOZ, W., R. M. SKOUG, R. M., GOLDSTEIN, B. E., NEUGEBAUER, M., RILEY, P. AND BALOGH, A., *Solar wind observations over Ulysses: first full polar orbit*, J. Geophys. Res., **105**, A5, 2000.
- [85] MCCOMAS, D. J., EBERT, R. W., ELLIOTT, H. A., SCHWADRON, N. A., GOLDSTEIN, B. E. AND GOSLING, J. T., *Weaker solar wind from the polar coronal holes and the whole Sun*, Geophys. Res. Lett., **35**, 18103, 2008.
- [86] MCDERMOTT, R. J., KERSTEIN, A. R., SCHMIDT, R. C. AND SMITH, P. J., *The ensemble mean limit of the one-dimensional turbulence*

- model and application to finite-volume large-eddy simulation*, J. Turb., **6**, 1-33, 2005.
- [87] MENEVEAU, C. AND SREENIVASAN, K., *Simple multifractal cascade model for fully developed turbulence*, Phys. Rev. Lett., **59**, 1424, 1987.
- [88] MITCHELL, D. G., KUTCHKO, F., WILLIAMS, D. J., EASTMAN, T. E., FRANK, L. A. AND RUSSELL, C. T., *An extended study of the low-latitude boundary layer on the dawn and dusk flanks of the magnetosphere*, J. of Geophys. Res., **92**, 7394-7404, 1987.
- [89] MUKAI, T., MACHIDA, S., SAITO, Y., HIRAHARA, M., TERASAWA, T., KAYA, N., OBARA, T., EJIRI, M. AND NISHIDA, M., *The low energy particle (LEP) experiment onboard the Geotail satellite*, J. of Geomagnetism and Geoelectricity, **46**, 1, 669-692, 1994.
- [90] NAGANO, I., YAGITANI, S., KOJIMA, H., KAKEHI, Y., SHIOZAKI, T., MATSUMOTO, H., HASHIMOTO, K., OKADA, T., KOKUBUN, S. AND YAMAMOTO, T., *Wave form analysis of the continuum radiation observed by GEOTAIL*, Geophysic. Research Lett., **21**, 25, 2911-2914, 1994.
- [91] NISHIDA, A., UESUGI, K., NAKATANI, I., MUKAI, T., FAIRFIELD, D. H. AND ACUNA, M. H., *Geotail mission to explore earth's magnetotail*, EOS- AGU, **73**, 40, 425-429, 1992.
- [92] OTTO, A. AND FAIRFIELD, D. H., *Kelvin-Helmholtz instability at the magnetotail boundary: MHD simulation and comparison with Geotail observations*, J. of Geophys. Res., **105**, 21,17521, 2000.
- [93] OUGHTON, S., PRIEST, E. R. AND W. H. MATTHAEUS, W. H., *The influence of a mean magnetic field on three- dimensional magnetohydrodynamic turbulence* , J. of Fluid Mechanics, **280**, 95-117, 1994.
- [94] PALADIN, G. AND VULPIANI, A., *Anomalous Scaling Laws in Multifractal Objects*, Phys. Rep., **156**, 4, 147-225, 1987.
- [95] PARKER, E. N., *Dynamics of the interplanetary gas and magnetic field*, Astrophys. J., **128**, 664-676, 1958.
- [96] PASCHMANN, G., HAERENDEL, G., SCKOPKE, N., ROSENBAUER, H. AND HEDGECOCK, P. C., *Plasma and magnetic field characteristics of*

- the distant polar cusp near local noon: the entry layer*, J. Geophys. Res., **81**, 2883-2899, 1976.
- [97] PEI, Z., HE, J., XIN, W., TU, C., MARSCH, E., LINGHUA, W. AND LIMEI, J., *Influence of intermittency on the anisotropy of magnetic structure functions of solar wind turbulence*, J. Geophys. Res., **121**, 2, 911-924, 2016.
- [98] PERRI, S., BALOGH, A., *Stationarity in solar wind flow*, Astrophys. J., **714**, 937-943, 2010.
- [99] PUCCI, F., MALARA, F., PERRI, S., ZIMBARDO, G., SORRISO-VALVO, L. AND VALENTINI, F., *Energetic particle transport in the presence of magnetic turbulence: influence of spectral extension and intermittency*, Mon. Not. R. Astron. Soc., **459**, 3, 3395-3406, 2016.
- [100] RICHARDSON, L. F., *Weather Prediction by Numerical Process*, Cambridge University Press, Cambridge, UK, 1922.
- [101] ROBERTS, D. A., *Construction of Solar-Wind-Like Magnetic Fields*, Phys. Rev. Lett., **109**, 31102, 2012.
- [102] ROSALES, C. AND MENEVEAU, C., *Anomalous scaling and intermittency in three-dimensional synthetic turbulence*, Phys. Rev., **E 78**, 016313, 2008.
- [103] ROSALES, C. AND MENEVEAU, C., *A minimal multiscale Lagrangian map approach to synthesize non-Gaussian turbulent vector fields*, Phys. Fluids, **18**, 075104, 2006.
- [104] ROSENBAUER, H., GRNWALDT, H., MONTGOMERY, M. D., PASCHMANN, G. AND SCKOPKE, N., *Heos 2 plasma observations in the distant polar magnetosphere: the plasma mantle*, J. of Geophys. Res., **80**, 2723-2737, 1975.
- [105] RUFFOLO, D., CHUYCHAI, P. AND MATTHAEUS, W., H., *Random Walk of Magnetic Field Lines in Nonaxisymmetric Turbulence*, Astrophys. J., **644**, 971, 2006.
- [106] RUSSELL, C. T., *Geophysical Coordinate Transformations*, Cosmic Electrodynamics, **2**, 184-196, 1971.

- [107] SAHRAOUI, F., BELMONT, G., REZEAU, L., CORNILLEAU-WEHRLIN, N., PINÇON, J. L., BALOGH, A., *Anisotropic Turbulent Spectra in the Terrestrial Magnetosheath as Seen by the Cluster Spacecraft*, Phys. Rev. Lett. **96**, 075002, 2006.
- [108] SARDINA, G., PICANO, F., BRANDT, L. AND CABALLERO, R., *Continuous Growth of Droplet Size Variance due to Condensation in Turbulent Clouds*, Phys. Rev. Lett., **115**, 184501, 2015.
- [109] SCKOPKE, N., PASCHMANN, G., HAERENDEL, G., SONNERUP, B. U., BAME, S. J., FORBES, T. G., HONES, E., W. AND RUSSELL, C. T., *Structure of the low-latitude boundary layer* J. of Geophys. Res.: Space Physics 1978-2012, **86**, A4, 2099-2110, 1981.
- [110] SCOTTI, A. AND MENEVEAU, C., *A fractal model for large eddy simulation of turbulent flow*, Physica D: Nonlinear Phenomena, **127**, 198-232, 1999.
- [111] SHE, Z., S. AND LÉVÊQUE, E., *Universal scaling laws in fully developed turbulence*, Phys. Rev. Lett., **72**, 336, 1994.
- [112] SHE, Z. S., *Intermittency and non-Gaussian statistics in turbulence*, Fluid Dyn. Res., **8**, 143-158, 1991.
- [113] SHE, Z. S., JACKSON, E. AND ORSZAG, S. A., *Intermittent vortex structures in homogeneous isotropic turbulence*, Nature, **344**, 226-228, 1990.
- [114] SHE, Z. S., JACKSON, E. AND ORSZAG, S. A., *Structure and dynamics of homogeneous turbulence: models and simulations* Proc. R. Soc. London, **A 434**, 101, 1991.
- [115] SHEBALIN, J. V., MATTHAEUS, W. H. AND MONTGOMERY, D., *Anisotropy in MHD turbulence due to a mean magnetic field*, J. Plasma Phys., **29**, 525, 1983.
- [116] SIGGIA, E. D., *Numerical study of small-scale intermittency in three-dimensional turbulence*, J. Fluid Mech., **107**, 375-406, 1981.
- [117] SONG, P. AND RUSSELL, C. T., *Model of the formation of the low-latitude boundary layer for strongly northward interplanetary magnetic*

- field*, J. of Geophys. Res.: Space Physics 1978-2012, **97**, A2, 1411-1420, 1992.
- [118] SONNERUP, B. U. Ö., *Theory of the low-latitude boundary layer*, J. of Geophys. Res., **85**, 2017-2026, 1980.
- [119] SORRISO-VALVO, L., CARBONE, V., BRUNO, R. AND VELTRI, P., *Persistence of small-scale anisotropy of magnetic turbulence as observed in the solar wind*, Europhys. Lett., **75**, 832-838, 2006.
- [120] SORRISO-VALVO, L., CARBONE, V., VELTRI, P., CONSOLINI, G. AND BRUNO, R., *Intermittency in the solar wind turbulence through probability distribution functions of fluctuations*, Geophys. Res. Lett., **26**, 1801-1804, 1999.
- [121] SORRISO-VALVO, L., YORDANOVA, E. AND CARBONE, V., *On the scaling properties of anisotropy of interplanetary magnetic turbulent fluctuations*, Europhys. Lett., **90**, 5, 59001, 2010.
- [122] SREENIVASAN, K. R. AND ANNU, A., *The phenomenology of small-scale turbulence*, Ann. Rev. Fluid Mech., **29**, 435-472, 1997.
- [123] STENUIT, H., ET AL., *Multispacecraft study on the dynamics of the dusk-flank magnetosphere under northward IMF: 10 ? 11 January 1997*, J. Geophys. Res., **107**, A10, 1333, 2002.
- [124] STAWARTZ, J. E., ET AL., *Observations of turbulence in a Kelvin-Helmholtz event on 8 September 2015 by the Magnetospheric Multiscale mission*, J. Geophys. Res. Space Physics, **121**, 11,021-11,034, 2016.
- [125] SUBEDI, P., CHHIBER, R., TESSEIN, J. A., WAN, M. AND MATTHAEUS, W. H., *Generating Synthetic Magnetic field intermittency using minimal multiscale lagrangian mapping approach*, Astrophys. J., **796**, 2, 97, 2014.
- [126] SUNDBERG, T., BOARDSEN, S. A., SLAVIN, J. A., ANDERSON, B. J., KORTH, H., ZURBUCHEN, T. H., RAINES, J. M AND SOLOMON, S. C., *MESSENGER orbital observations of large-amplitude Kelvin-Helmholtz waves at Mercury's magnetopause*, J. of Geophys. Res., **117**, A04216, 2012.

- [127] TAKAGI, K., HASHIMOTO, C., HASEGAWA, H., FUJIMOTO, M. AND TANDOKORO, R., *Kelvin-Helmholtz instability in a magnetotail flank-like geometry: Three-dimensional MHD simulations*, J. Geophys. Res., **111**, A08202, 2006.
- [128] TAYLOR, G. I., *The spectrum of turbulence*, RSPSA, **164**, 476, 1938.
- [129] TERASAWA, T., FUJIMOTO, M., MUKAI, T., SHINOHARA, I., SAITO, Y., YAMAMOTO, T., MACHIDA, S., KOKUBUN, S., LAZARUS, A. J., STEINBERG, J. T. AND LEPPING, R. P., *Solar wind control of density and temperature in the near-earth plasma sheet: Wind/Geotail collaboration*, Geophys. Res. Lett., **24**, 8, 935-938, 1997.
- [130] TSURUDA, T., HAYAKAWA, H., NAKAMURA, M., OKADA, T., MATSUOKA, A., MOZER, F. S. AND SCHMIDT, R., *Electric Field Measurements on the GEOTAIL Satellite*, J. of Geomagnetism and Geoelectricity, **46**, 693-711, 1994.
- [131] VAN ATTA, C. W., & PARK, J., *Statistical self-similarity and inertial subrange turbulence*, Lect. Notes in Phys., **12**, 402-426, 1975.
- [132] VINCENT, A. AND MENEGUZZI, M., *The satial structure and statistical properties of homogeneous turbulence*, J. Fluid Mech., **225**, 1, 1991.
- [133] VIO, R., CRISTIANI, S., LESSI, O. AND PROVENZALE, A., *Time series analysis in astronomy - an application to quasar variability studies*, Astrophys. J., **391**, 2, 518-530, 1992.
- [134] VOLLAND, H., *Handbook of atmospheric electrodynamics*, **2**, CRC Press, Florida, 1995.
- [135] WILLIAMS, D. J., MCENTIRE, R. M., SCHLEMM II, C., LUI, A. T. Y., GLOECKLER, G., CHRISTON, G. AND GLIEM, V., *Plasma Wave Observations with GEOTAIL Spacecraft*, Journal of Geomagnetism and Geoelectricity, **46**, 1, 39-58, 1994.
- [136] WING, S. AND NEWELL, P. T., *2D plasma sheet ion density and temperature profiles for northward and southward IMF*, Geophys. Res. Lett., **29**, 9, 2002.

- [137] YAMAMOTO, T., *A linear analysis of the hybrid Kelvin-Helmholtz/Rayleigh-Taylor instability in an electrostatic magnetosphere-ionosphere coupling system*, J. of Geophys. Res., **113**, 2008.
- [138] YORDANOVA, E., PERRI, S., SORRISO-VALVO, L. AND CARBONE, V., *Multipoint observation of anisotropy and intermittency in solar-wind turbulence*, Europhys. Lett., **110**, 1, 19001, 2015 .
- [139] ZIMBARDO, G., VELTRI, P. AND POMMOIS, P., *Anomalous, quasi-linear, and percolative regimes for magnetic-field-line transport in axially symmetric turbulence*, Phys. Rev., **E 61**, 1940, 2000.
- [140] ZIMBARDO, G., GRECO, A., SORRISO-VALVO, L., PERRI, S., VÖROS, Z., ABURJANIA, G., CHARGAZIA, K., ALEXANDROVA, O., *Magnetic Turbulence in the Geospace Environment*, Space Sci. Rev., **156**, 89-134, 2010.